

Reactivity of Electrogenenerated Free Hydroxyl Radicals and Activation of Dioxygen on Boron-Doped Diamond Electrodes

THÈSE N° 4129 (2008)

PRÉSENTÉE LE 4 JUILLET 2008

À LA FACULTE SCIENCES DE BASE

GROUPE DE GÉNIE ÉLECTROCHIMIQUE

PROGRAMME DOCTORAL EN CHIMIE ET GÉNIE CHIMIQUE

ÉCOLE POLYTECHNIQUE FÉDÉRALE DE LAUSANNE

POUR L'OBTENTION DU GRADE DE DOCTEUR ÈS SCIENCES

PAR

Agnieszka KAPALKA

M.Sc. in materials science, AGH University of science and technology Cracow, Pologne
et de nationalité polonaise

acceptée sur proposition du jury:

Prof. F. M. Wurm, président du jury
Prof. C. Comninellis, directeur de thèse
Prof. A. De Battisti, rapporteur
Prof. A. Savall, rapporteur
Dr R. Thampi, rapporteur



ÉCOLE POLYTECHNIQUE
FÉDÉRALE DE LAUSANNE

Suisse
2008

Acknowledgments

The work presented here results from collaboration and support of many people. First of all, I would like to thank my thesis supervisor Prof. Christos Comninellis for having accepted me as a PhD student in his group, and for introducing me to the fascinating field of electrochemistry. His continuous support, encouragement, and suggestions have helped me a lot in my work. I truly appreciate all the discussions that often opened my eyes and directed my research.

Thanks to all the members of the jury: Prof. Florian Maria Wurm, Prof. André Savall, Prof. Achille De Battisti, and Dr. Ravindranathan Thampi for reading and evaluating my thesis as well as assisting in my exam.

Many thanks to Dr. György Fóti for his help at all time and priceless tips.

Thanks to Prof. Helmut Baltruschat for accepting me for one month in his research group in Bonn, introducing me to DEMS, and for numerous interesting discussions. Barbora Lanova, thank you for your warm welcome, great help in DEMS measurements, and unforgettable “Bonn by night”.

Special thanks to Ingrid Margot and Evelyne Toubes-Scherrer for their help in administration and to Gérard Bovard and André Fattet for their invaluable technical support.

To everyone in the GGEC team: Justyna, Béatrice, Ilaria, Elena, Guillaume, Bahaa, Arnaud, Alain, Erika, Mériadec, Cyril, Pietro, Stéphane, Déborah, Gabriele, and Lassiné for all the good moments we have shared. Many thanks to Bahaa and Béatrice for introducing me to electrochemical measurements, Déborah for assisting me in the lab, and to Cyril for “résumé”.

Special thanks to Blanca, Michal, Erika, Jochen, Lisa, Kim, Marina, Gabriele, Philippe, Kathryn, Yadira, Martin, Pamela, Pietro, Micaela, Kashid, Elina, Natasha, Gwen ... for all fun we have had together and for your friendship.

Special thanks to my family for never ending support. Szczególnie dziękuję moim rodzicom za trzymanie kciuków w najtrudniejszych momentach oraz mojej siostrze za wielogodzinne rozmowy...

Największe jednak podziękowania kieruję do mojego męża Michała. Dziękuję Ci nie tylko za te wspaniałe lata spędzone razem w Lozannie, ale również za Twoją nieustanną pomoc. Dziękuję Ci niezmiernie za online support, intensywny kurs Matlaba i LyX'a oraz za nieocenioną pomoc w rozwiązywaniu równań.

To właśnie Tobie dedykuję niniejszą pracę.

Abstract

Synthetic boron-doped diamond (BDD) thin film is an electrode material with high chemical and dimensional stability, low background current and a very wide potential window of water stability. Upon anodic polarization, BDD generates hydroxyl radicals that mediate the oxidation processes in the vicinity of the electrode surface. These hydroxyl radicals are assumed to be free, i.e., not adsorbed on the electrode surface.

Hydroxyl radicals are formed on BDD during water discharge, which is the rate determining step of oxygen evolution reaction. Oxygen evolution on BDD occurs at a high overpotential (over 1 V) with respect to the thermodynamic potential for O₂ formation ($E_{OER}^{\circ} = 1.23$ V vs. SHE), but very close to the thermodynamic potential of HO• formation ($E_{HO^{\bullet}}^{\circ} = 2.38$ V vs. SHE). In the presence of organics, the onset potential of HO• formation changes, which affects the current-potential curves. As a consequence, oxidation of most of organic compounds on BDD results in a shift of the current-potential curves toward lower potentials. An exception is acetic acid, which adsorbs on the electrode surface causing auto-inhibition of its oxidation (oxidation is shifted toward higher potentials). In general, however, oxidation of organics on BDD is a fast reaction, controlled by the mass transport of organics to the anode surface.

In the presence of an organic compound, hydroxyl radicals initiate chain reactions resulting in involvement (activation) of molecular oxygen dissolved in aerated aqueous solution. Direct evidence for this process was found during oxidation of acetic acid solution saturated with isotopically labelled ¹⁸O₂. As a result, C¹⁸O₂ and C¹⁶O¹⁸O were evolved proving that molecular oxygen participates in the mineralization of acetic acid. This electrochemically induced activation process is probably initiated by organic free radicals (R•) formed during reaction between organic compounds and hydroxyl radicals. Organic free radicals react further with molecular oxygen to form peroxy radical (RO₂•). Organic peroxy radicals are very reactive and can initiate subsequent chain reactions leading, via several possible intermediates, to complete oxidation of organic compound. In fact, similar mechanism has been reported in radiolysis (upon X-ray or γ-ray) of aqueous

solutions of acetic acid. This non-faradaic enhancement of the electrooxidation processes opens the possibilities for designing a less energy consuming degradation of organic pollutants on BDD anodes.

KEYWORDS: boron-doped diamond; hydroxyl radicals; molecular oxygen; oxygen evolution; oxidation of organics

Résumé

La fine couche synthétique de diamant dopé au bore (BDD) est un matériel d'électrode qui possède une stabilité chimique et dimensionnelle élevée, un courant de fond bas et une fenêtre potentielle très large. Sous polarisation anodique, l'électrode BDD produit des radicaux hydroxyle qui participent aux processus d'oxydation à proximité de la surface de l'électrode. On suppose que ces radicaux hydroxyle sont libres, i.e., non adsorbé à la surface de l'électrode.

Les radicaux hydroxyle sont formés sur BDD pendant la décharge de l'eau, qui est l'étape déterminante de la réaction du dégagement d'oxygène. Le dégagement d'oxygène sur BDD a lieu aux grandes surtensions (au dessus de 1 V) conformément au potentiel thermodynamique de la formation de l'oxygène ($E_{OER}^{\circ} = 1.23$ V vs. SHE), mais très près du potentiel thermodynamique de formation de HO^{\bullet} ($E_{HO^{\bullet}}^{\circ} = 2.38$ V vs. SHE). En présence de produits organiques, le potentiel de formation de HO^{\bullet} change, ce qui affecte les courbes de courant-tension. Ainsi, l'oxydation de la plupart des composés organiques sur BDD a pour conséquence un décalage des courbes de courant-tension vers des potentiels inférieurs. Une exception est observée pour l'acide acétique qui s'adsorbe sur la surface de l'électrode et qui cause l'auto-inhibition de son oxydation (l'oxydation est décalée vers des potentiels plus élevés). Cependant, l'oxydation des produits organiques sur BDD est, en général, une réaction rapide, contrôlée par le transport de masse des produits organiques à la surface de l'anode.

En présence d'un composé organique, les radicaux hydroxyle amorcent des réactions en chaîne ayant pour résultat l'accroissement de l'activité de l'oxygène moléculaire dissout dans le soluté aqueux aéré. La preuve directe de ce processus est donnée par l'oxydation d'une solution d'acide acétique saturée en oxygène isotopique $^{18}O_2$; la formation de $C^{18}O_2$ et de $C^{16}O^{18}O$ qui en découle, montre que l'oxygène moléculaire participe à la minéralisation de l'acide acétique. Ce procédé d'activation électrochimique est probablement amorcée par les radicaux organiques libres (R^{\bullet}) formés pendant la réaction entre les composés organiques et les radicaux hydroxyle. Les radicaux organiques libres réagissent ensuite avec l'oxygène moléculaire pour former des radicaux

peroxy de forme RO_2^\bullet . Les radicaux organiques peroxy sont très réactifs et peuvent amorcer de futures réactions en chaîne permettant, par plusieurs intermédiaires possibles, l'oxydation complète du composé organique. En fait, un mécanisme semblable a été observé dans la radiolyse (sous rayon X ou γ) des solutés de l'acide acétique. Cette augmentation non-faradique du processus d'électro-oxidation ouvre de nouvelles possibilités pour la conception de procédés de dégradation des polluants organiques sur des anodes de BDD en consommant moins d'énergie.

MOTS-CLÉS: diamant dopé au bore; radicaux hydroxyle; l'oxygène moléculaire; dégagement d'oxygène; l'oxydation des composés organiques

Contents

Contents	vii
1 Introduction	1
2 Bibliography	5
2.1 Electrochemistry of diamond	6
2.1.1 Synthesis of boron-doped diamond by HF-CVD	6
2.1.2 Properties and applications of BDD electrodes	8
2.1.3 Theoretical model for oxidation of organic compounds on BDD	10
2.1.4 Mechanism for organics oxidation on active and non-active electrodes	14
2.2 Differential electrochemical mass spectrometry	16
2.2.1 DEMS setup	17
2.2.2 DEMS analysis	19
2.3 Activation of molecular oxygen	21
3 Theoretical Part	25
3.1 Electrogenation of hydroxyl radicals on the electrode surface in acid solution	26
3.1.1 Formation of hydroxyl radicals by water discharge	26
3.1.2 Thermodynamic aspect of free HO• formation	26
3.1.3 The influence of the anode material on the potential of HO• formation	27
3.1.4 Electrogenation of HO• on BDD electrode	28
3.2 Concentration profile of hydroxyl radicals on BDD electrodes	29
3.2.1 Concentration profile of HO• during oxygen evolution	29
3.2.2 Concentration profile of HO• during oxidation of organic compounds	32
3.3 Shift of water discharge potential during organics oxidation	35
3.4 Conclusions	37

4	Oxygen Evolution Reaction; A Kinetic Study	39
4.1	Introduction	40
4.2	Experimental details	41
4.3	Results	44
4.3.1	Comparison of the electrochemical response of BDD and BDD MEA . .	44
4.3.1.1	Potential window	44
4.3.1.2	Anodic Tafel plot	45
4.3.2	Surface redox couples	47
4.3.3	Activation enthalpy	49
4.3.4	Reaction order	51
4.4	Discussion	51
4.5	Conclusions	53
5	Electrochemical Oxidation of C₁- Organic Compounds; Voltammetry and DEMS	55
5.1	Introduction	56
5.2	Experimental details	57
5.3	Results	60
5.3.1	Voltammetric study of methanol and formic acid oxidation	60
5.3.2	DEMS study of methanol and formic acid oxidation	62
5.3.2.1	Response of the supporting electrolyte	62
5.3.2.2	Methanol oxidation	62
5.3.2.3	Formic acid oxidation	64
5.4	Discussion	67
5.5	Conclusions	71
6	Electrochemical Oxidation of Formic Acid with 100% current efficiency	73
6.1	Introduction	74
6.2	Optimization of the electrochemical mineralization on BDD anodes	76
6.3	Experimental details	78
6.4	Results and discussion	79
6.4.1	Bulk electrolysis of formic acid under different electrolysis regimes . . .	79
6.4.2	Bulk electrolysis of formic acid under programmed current	80
6.5	Conclusions	82

7	Electrochemical Oxidation of Acetic Acid; Voltammetry and Chronoamperometry	83
7.1	Introduction	84
7.2	Experimental details	84
7.3	Results	85
7.3.1	Anodic polarization curves	85
7.3.2	Anodic Tafel plots	86
7.3.3	Effect of the concentration on acetic acid electrooxidation	87
7.3.4	Effect of the potential on acetic acid electrooxidation	88
7.3.5	Behavior of $\text{Ce}^{3+/4+}$ redox couple in presence of acetic acid	88
7.3.6	Formic acid electrooxidation in presence of acetic acid	92
7.4	Discussion	93
7.5	Conclusions	95
8	Electrochemical Oxidation of Acetic Acid; DEMS	97
8.1	Introduction	98
8.2	Experimental details	99
8.3	Results	102
8.3.1	Electrooxidation of acetic acid	102
8.3.2	Effect of acetic acid concentration	103
8.3.3	Detection of intermediates	104
8.4	Discussion	106
8.5	Conclusions	109
9	Electrochemically Induced Oxidation of Acetic Acid by Molecular Oxygen	111
9.1	Introduction	112
9.2	Experimental details	113
9.3	Results	114
9.3.1	Electrooxidation of air/oxygen-saturated solution of acetic acid	114
9.3.2	Electrooxidation of acetic acid saturated with isotopically labelled $^{18}\text{O}_2$	116
9.4	Discussion	118
9.5	Conclusions	122
10	General Discussion	125

11 Perspectives	131
11.1 Mechanically implanted MI-BDD electrodes	132
11.1.1 Introduction	132
11.1.2 Preparation of the mechanically implanted MI-BDD electrodes	133
11.1.3 Electrochemical characterization of LC-MI-BDD electrode	135
11.1.4 Discussion	137
11.1.5 Conclusions	139
11.2 Electrochemically induced activation of molecular oxygen	140
11.3 Study of adsorption process on BDD surface	140
References	141
List of Symbols	153
Curriculum Vitae	157

Chapter 1

Introduction

Conductive boron-doped diamond (BDD) is an electrode material with outstanding properties, which are remarkably different from those of other traditional carbon electrodes such as glassy carbon or graphite. As reported in [1, 2, 3], diamond electrodes have a wide working potential window, low capacitance, high chemical inertness, and dimensional stability. All these properties have led to application of diamond in electrochemistry, opening a new branch known as electrochemistry of diamond electrodes [1].

The first extensive study of use of diamond electrodes in electrochemistry was done by Pleskov et al. in 1987 [4]. Since then, the synthetic BDD thin films have attracted attention of researchers resulting in a rapid increase in the number of publications (Fig. 1.1) and patents. Until now, the

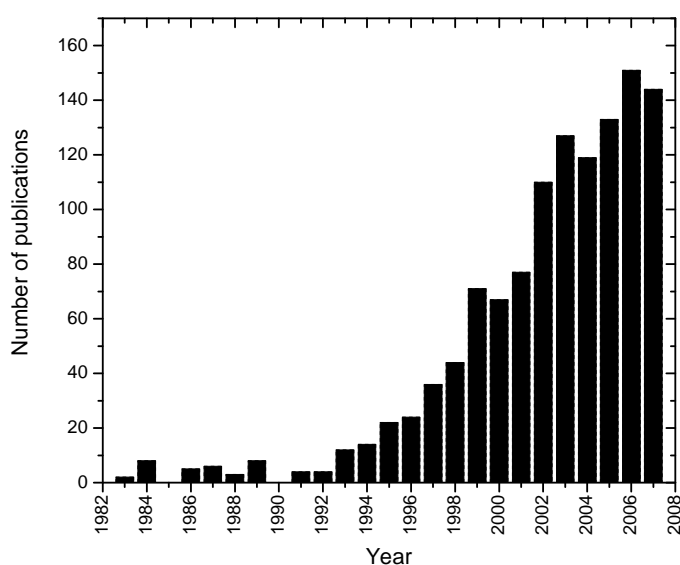


Figure 1.1. Yearly research publications on diamond electrochemistry.

main electrochemical applications of diamond electrodes are in the domains of: electrosynthesis [5, 6], electrochemical treatment of organic pollutants [7, 8, 9, 10], electroanalysis [11, 12, 13], preparation of strong oxidants [14], and recovery of heavy metals [15].

Although, in general, electrochemical reactions can proceed as long as a current is supplied to the electrode, the knowledge of the electrochemical reaction mechanism is still important in order to design less energy consuming processes. Thus, fundamental research is a basis for understanding of the electrochemical reaction mechanism and efficient use of energy.

This work focuses on better understanding of the role of hydroxyl radicals and molecular oxygen in the electrooxidation processes on boron-doped diamond electrodes. Two processes are investigated: (i) oxygen evolution, and (ii) oxidation of organic compounds (methanol, formic acid, and acetic acid) in aqueous solution. In both cases, hydroxyl radicals, formed during water discharge on the diamond surface, are believed to be the main intermediates.

In Chapter 3, the theoretical aspect of electrogeneration of free hydroxyl radicals (HO^\bullet) is discussed and a model describing the HO^\bullet concentration profile at the BDD surface, in the presence and absence of organic compounds, is presented. The determined surface concentration of HO^\bullet has been used to predict the shift of the current-potential curves, toward lower potentials, induced by the reaction of the electrogenerated HO^\bullet with the organic compounds present in the electrolyte.

The kinetics of oxygen evolution reaction (OER) in 1 M HClO_4 is studied in Chapter 4 using both BDD macroelectrode and microelectrodes-array. Two main aspects are considered: (i) the high overpotential for oxygen evolution (over 1 V), and (ii) the high Tafel slope for OER reported on BDD in the literature (between 220 and 415 mV dec^{-1} [16, 17, 18]). On the basis of the obtained results, a simplified mechanism of OER and the involved rate-determining step are proposed.

In Chapter 5, the electrochemical oxidation of C1-organic compounds (methanol and formic acid) is studied using voltammetry and differential electrochemical mass spectrometry (DEMS). An indirect mechanism of electrooxidation, mediated by free hydroxyl radicals, is proposed. Furthermore, experimental verification of the model proposed in Chapter 3 is also provided.

In Chapter 6, the bulk electrolysis of formic acid is presented. It is shown that electrolysis performed under programmed current allows to achieve fast mineralization of formic acid with a current efficiency close to 100% throughout the electrolysis.

In Chapters 7–9, the electrochemical oxidation of acetic acid is studied using voltammetry, chronoamperometry, and DEMS. It is shown that, contrary to most of organic compounds, acetic

acid adsorbs on the BDD surface resulting in auto-inhibition of its oxidation. The proposed mechanism of acetic acid electrooxidation includes mediation of both hydroxyl radicals and molecular oxygen dissolved in aerated aqueous solution.

Finally, Chapters 10 and 11 summarize the main results obtained in this thesis and show directions for the future investigations.

The results presented in this thesis allow for better understanding of the electrochemical oxidation processes on boron-doped diamond electrodes in aqueous solutions, showing promise for a less energy consuming electrochemical treatment of organic wastes.

Chapter 2

Bibliography

In the first part of this chapter a review of the literature in the field of electrochemistry of boron-doped diamond (BDD) is presented. This part focuses mainly on synthesis of diamond thin films, their properties and application in wastewater treatment. In the second part, the principles of the differential electrochemical mass spectrometry (DEMS), which is an on-line method used for detection of electrochemical reaction products, are discussed. Both the experimental and analytical aspects of this method are considered. Finally, the third part of this chapter deals with the activation of molecular oxygen in photochemistry and radiolysis. These topics were selected in order to give the background for the following experimental chapters.

2.1 Electrochemistry of diamond

2.1.1 Synthesis of boron-doped diamond by HF-CVD

Diamond is an allotropic form of carbon whose uniqueness is related to the high atomic density, extreme hardness and mechanical / chemical resistance [19]. Being an insulator, diamond needs to be doped (with boron, fluorine or nitrogen) in order to be useful as an electrode material [20]. Diamond thin films, deposited on an appropriate substrate by chemical vapor deposition (CVD) are the most widely studied and well reported in literature [15, 21]. This technique involves a gas-phase chemical reaction above a solid surface. Depending on the mode of gas activation (typically mixture of CH_4 / H_2 / $\text{B}(\text{CH}_3)_3$), two main techniques have been used for the diamond deposition: the hot-filament and the microwave-assisted plasma-enhanced chemical vapor deposition. Since in this work BDD electrodes were prepared by the Hot Filament Chemical Vapor Deposition (HF-CVD) at the CSEM (Swiss Center for Electronics and Microtechnology), only this method will be described in details.

The HF-CVD reactor consist of a continuously pumped vacuum chamber, as shown in Fig. 2.1 [22]. The reactive gas is a mixture of methane (0.5–2.5%) in hydrogen containing various amount of trimethylboron as a boron source to give different boron to carbon ratios (B/C) in the deposit.

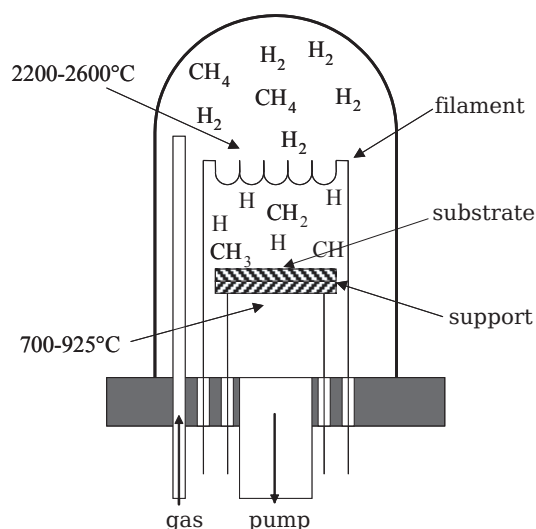


Figure 2.1. Schematic representation of the HF-CVD reactor [22].

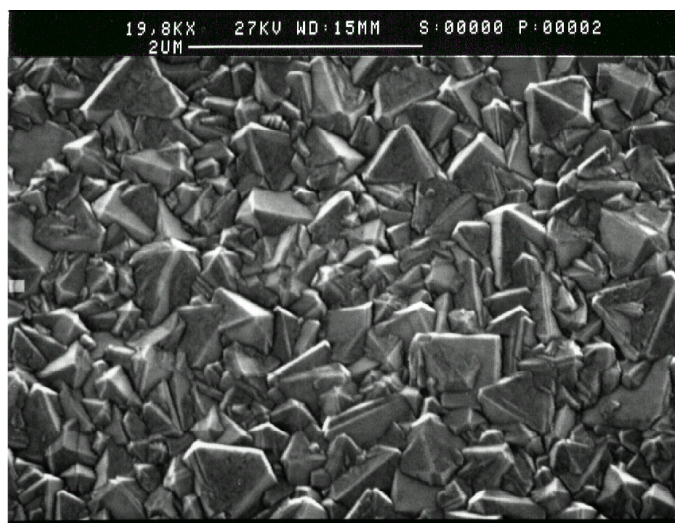


Figure 2.2. SEM micrograph of a polycrystalline boron-doped diamond.

The gaseous mixture is thermally activated (dissociated) by the tungsten or tantalum filament heated at 2200–2600°C. Few millimeters below the filament, the substrate (typically p-Si, Ti, Nb, Ta, Mo, W), on which the deposition of diamond proceeds, is kept at 700–925°C (Fig. 2.1).

The nucleation of diamond on non-diamond substrates is still not well understood. According to a commonly accepted theory [23], activation of CH_4 / H_2 gas results in formation of hydrogen atoms, which abstract hydrogen from methane and form methyl radicals. These methyl radicals are the main species responsible for diamond growth. After being formed, all reactive species diffuse towards the substrate surface, where they adsorb and coalesce. To allow the initiation and the construction of tetrahedrally coordinated sp^3 network, diamond particles must be present on the substrate surface. These particles are introduced during pretreatment of the surface, typically by mechanical polishing with a diamond powder. Thus, atomic hydrogen abstracts a hydrogen atom from the diamond surface, leaving a surface radical which can further react with methyl radical. The coalescence of the latter lead to formation of diamond film.

The synthesis of diamond by HF-CVD results in a randomly textured polycrystalline boron-doped diamond film on a conductive substrate (Fig. 2.2). The typical boron concentration in the deposit is in the range of 200–10000 ppm [19, 24, 25]. At lower boron concentrations (< 200 ppm), the resistivity of the formed thin films is too high for electrochemical applications. On the other hand, higher B/C ratio (> 10000 ppm) leads to the fast degradation of the electrodes, probably due to the formation of high amount of sp^2 species. As the boron content increases, diamond changes its nature from a dielectric, then progressively to a wide-gap semiconductor, degenerate

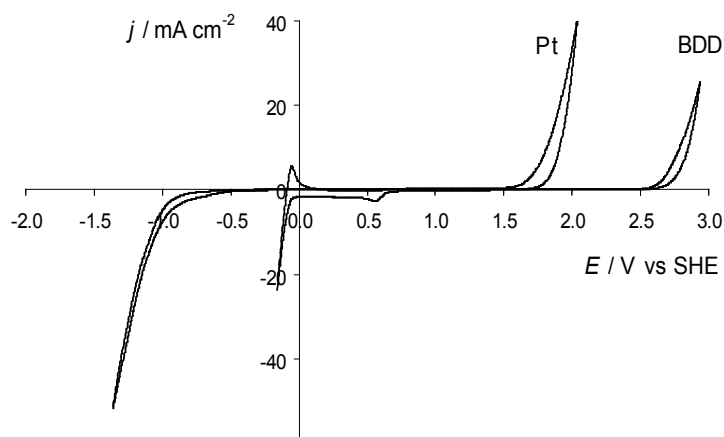


Figure 2.3. Comparison of the cyclic voltammograms recorded on BDD and Pt electrode; electrolyte 1M H₂SO₄; scan rate 50 mV s⁻¹ [22].

semiconductor, and finally a quasi-metal.

As-grown chemical vapor deposited BDD electrodes are terminated with hydrogen. These surfaces are hydrophobic and are not attractive for adsorption. The electrode surface changes from hydrophobic to hydrophilic, and chemically bound oxygen is present on a diamond surface, due to anodic polarization [26, 27, 28]. Oxygen terminated BDD, although still very unreactive compared to other carbon electrodes, is not completely inert and may undergo electrostatic interactions with certain molecules.

2.1.2 Properties and applications of BDD electrodes

The first extensive study of use of diamond electrodes in electrochemistry was performed by Pleskov et al. in 1987 [4]. Since then, synthetic BDD thin films have been applied in a number of applications due to their outstanding properties, which are remarkably different from those of other conventional electrodes, e.g., glassy carbon or platinum [1, 2, 3]. Compared to graphite or glassy carbon electrodes, diamond electrodes have a good resistance toward corrosive conditions and resistance to fouling (deactivation). Furthermore, diamond thin films exhibit a very large potential window with respect to hydrogen / oxygen evolution, extending to almost 4 V, and a low background current. Compared to Pt electrodes, the potential window of BDD is about 2 V larger, as shown in Fig. 2.3. High anodic stability of BDD in acid medium and high oxygen evolution overpotential allow to produce powerful oxidants of high redox potential. Recently, Marselli et al. [29] have confirmed, by means of spin trapping, the formation of hydroxyl radicals on BDD

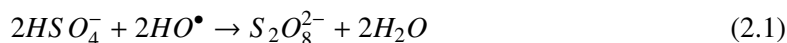
electrode during its anodic polarization in acid aqueous solution.

All these properties have led to application of diamond electrodes in electrosynthesis [5, 6], electro-mineralization of organic pollutants [7, 8, 9, 10], preparation of strong oxidants [14], recovery of heavy metals [15], and electroanalysis [11, 12, 13]. In this section, the application of BDD anodes in preparation of powerful oxidants, electrosynthesis and wastewater treatment will be described in more details [30].

Preparation of powerful oxidants

The production of oxidants with high redox potential can be performed on BDD by either a direct electron transfer or an indirect mechanism mediated by hydroxyl radicals. In the former case, oxidants are produced in a fast electron transfer reaction. A typical example is the couple $\text{Ag}^{2+}/\text{Ag}^+$ ($E^\circ = 1.98 \text{ V vs. SHE}$), which can be used as mediator in the electrochemical oxidation for synthesis and for the treatment of nuclear wastes.

A typical example of the indirect process of oxidants formation on BDD involves the couple $\text{S}_2\text{O}_8^{2-}/\text{SO}_4^{2-}$ ($E^\circ = 2.0 \text{ V vs. SHE}$). It is assumed that hydroxyl radicals are involved in formation of peroxodisulfate in H_2SO_4 , as given by Eq. 2.1.

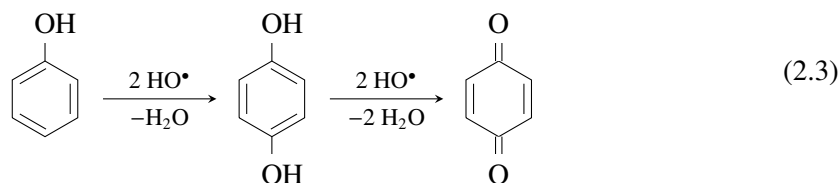


The most important applications of peroxodisulfate are in etching printed circuits, acrylonitrile polymerization, wastewater treatment, dye oxidation, and fiber whitening.

Electrosynthesis

The feasibility of electroorganic synthesis on diamond electrodes was investigated and reported in literature. The oxidation of phenol to benzoquinone is a typical example. Preparative bulk electrolysis of phenol on BDD anodes under galvanostatic conditions revealed that, depending on experimental conditions, it is possible to obtain partial oxidation of phenol to aromatic intermediates (benzoquinone, hydroquinone and catechol) or its complete mineralization to carbon dioxide. The electrochemical oxidation of phenol involves hydroxyl radicals formed during water discharge on BDD anodes (Eq. 2.2), which react with phenol in the vicinity of the electrode surface (Eq. 2.3).





Similar mechanism was proposed for oxidation of 3-methylpyridine to nicotinic acid. In both cases, the oxidation of organics in the potential region of water decomposition does not lead to deactivation of the electrode surface.

Wastewater treatment

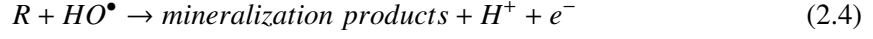
Biological treatment is the most economic process of wastewater depollution and it is used for the elimination of readily biodegradable organic pollutants. This kind of treatment, however, is not applicable to refractory and toxic pollutants for which an electrochemical oxidation becomes a very attractive alternative. The oxidation of various organic compounds has been investigated on BDD anodes (carboxylic acids, alcohols, ketones, phenolic compounds and aromatic acids). It has been shown that destruction of pollutants on diamond electrodes proceeds with a high current efficiency and at appreciable rates. Two mechanisms were distinguished for the electrochemical oxidation of organic compounds on BDD: direct oxidation and indirect oxidation via electrogenerated intermediates formed at high anodic potentials.

The oxidation of carboxylic acid requires high anodic potentials, i.e., it occurs in the region of water discharge ($> 2.3 \text{ V vs. SHE}$). This phenomenon has been explained by the presence and mediation of electrogenerated hydroxyl radicals, confirming the indirect mechanism. Oxidation of phenolic compounds can proceed in the potential region of water stability indicating a direct oxidation mechanism. The latter however results in a deposition of the adhesive polymeric material which can not be removed by washing with organic solvents. To restore the initial activity of electrode, it is necessary to apply high anodic potentials ($E > 2.3 \text{ V vs. SHE}$) at which BDD can form active intermediates, probably hydroxyl radicals, that oxidize the polymeric film present on the electrode surface.

2.1.3 Theoretical model for oxidation of organic compounds on BDD [22, 31]

The model of electrochemical mineralization of organics on BDD anodes has been developed for a batch recirculation reactor system under galvanostatic conditions, based on a simplified mecha-

nism given in Eqs. 2.2, 2.4–2.5.



In this mechanism, electrogenerated hydroxyl radicals are the intermediates for both the main reaction of organics oxidation (Eq. 2.4) and the side reaction of oxygen evolution (Eq. 2.5). For this simplified mechanism reaction scheme a kinetic model was proposed with the following assumptions: (i) adsorption of the organic compounds at the electrode surface is negligible, (ii) all organics have the same diffusion coefficient D ; (iii) the global rate of the electrochemical mineralization of organics is a fast reaction and it is controlled by mass transport of organics to the anode surface. The consequence of this last assumption is that the rate of the mineralization reaction is independent of the chemical nature of the organic compound present in the electrolyte. Under these conditions, the limiting current density for the electrochemical mineralization of an organic compound (or a mixture of organics) under given hydrodynamic conditions can be written as:

$$j_{lim}(t) = 4Fk_mCOD(t) \quad (2.6)$$

where j_{lim} ($A\ m^{-2}$) is the limiting current density, F ($C\ mol^{-1}$) is the Faraday constant, k_m ($m\ s^{-1}$) is the mass transport coefficient, and COD ($mol\ O_2\ m^{-3}$) is the chemical oxygen demand.

At the beginning of electrolysis, at time $t = 0$, the initial limiting current density (j_{lim}^0) is given by:

$$j_{lim}^0 = 4Fk_mCOD^0 \quad (2.7)$$

where COD^0 is the initial chemical oxygen demand.

Under galvanostatic conditions, two different operating regimes are defined: at $j_{apply} < j_{lim}$ the electrolysis is controlled by the charge transfer and at $j_{apply} > j_{lim}$ it is controlled by the mass transfer.

Electrolysis under current limited control ($j_{apply} < j_{lim}$)

In this operating regime, the current efficiency is 100% and the rate of *COD* removal is constant and can be written as:

$$r = \alpha \frac{j_{lim}^0}{4F} \quad (2.8)$$

where α is the dimensionless current density defined as:

$$\alpha = \frac{j_{apply}}{j_{lim}^0} \quad \text{with } 0 < \alpha < 1 \quad (2.9)$$

The evolution of *COD*(*t*) with time, in this operating regime ($j_{apply} < j_{lim}$), is given by:

$$COD(t) = COD^0 \left(1 - \alpha \frac{Ak_m}{V_r} t \right) \quad (2.10)$$

where A (m²) is the anode surface, and V_r (m³) is the volume of reservoir in a batch recirculation reactor system.

This behavior persists until a critical time (t_{cr}), at which the applied current density is equal to the limiting current density, which corresponds to:

$$COD_{cr} = \alpha COD^0 \quad (2.11)$$

Substituting Eq. 2.11 in Eq. 2.10 the critical time is defined as:

$$t_{cr} = \frac{1 - \alpha}{\alpha} \frac{V_r}{Ak_m} \quad (2.12)$$

Electrolysis under mass transport control ($j_{apply} > j_{lim}$)

When the applied current exceeds the limiting current, secondary reactions (such as oxygen evolution) commence resulting in a decrease of the instantaneous current efficiency (*ICE*). In this regime, *COD* decreases exponentially with time (Eq. 2.13).

$$COD(t) = \alpha COD^0 \exp \left(-\frac{Ak_m}{V_r} t + \frac{1 - \alpha}{\alpha} \right) \quad (2.13)$$

The instantaneous current efficiency (*ICE*) can be defined as:

$$ICE = \frac{j_{lim}}{j_{apply}} = \frac{COD(t)}{\alpha COD^0} \quad (2.14)$$

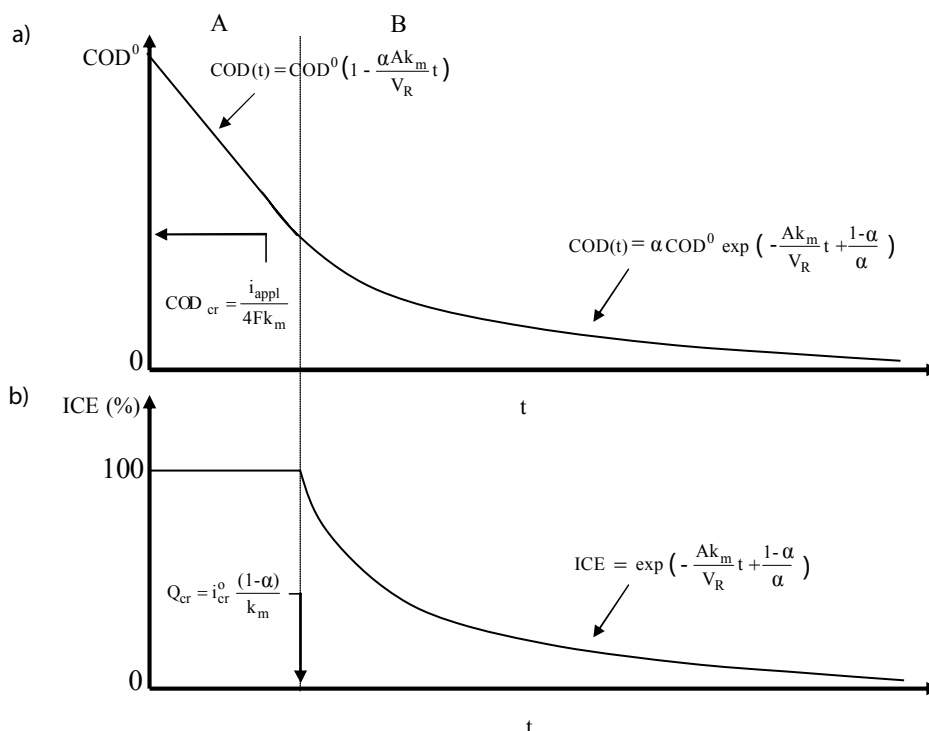


Figure 2.4. Evolution of (a) COD and (b) ICE in function of time; (A) represents the charge transport control; (B) represents the mass transport control.

Thus, from Eqs. 2.13 and 2.14, ICE is now given by:

$$ICE = \exp\left(-\frac{A k_m}{V_r} t + \frac{1-\alpha}{\alpha}\right) \quad (2.15)$$

A graphical representation of the proposed kinetic model is given in Fig. 2.4. In order to verify the validity of this model, anodic oxidation of various aromatic compounds in acidic solution has been performed by varying organics concentration and current density [31].

Formation of intermediates

It has been found, that the amount and nature of intermediates formed during the electrochemical mineralization of organics on BDD anodes depends strongly on the working regime. In fact, electrolysis under conditions of current limited control results usually in the formation of an important number of intermediates in contrast to electrolysis under mass transport regime, where practically no intermediates are formed and CO_2 is the only final product. The complete mineralization under mass transport regime has been explained by a high local concentration of electrogenerated

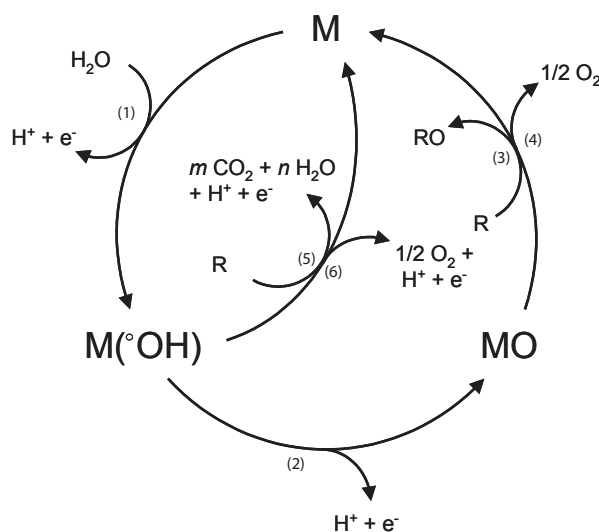


Figure 2.5. Scheme of the electrochemical oxidation of organic compounds on *active* anodes (reactions (1), (2), (3), and (4)), and *non-active* anodes (reactions (1), (5), and (6)); M is an active site at the electrode surface [31].

hydroxyl radicals on the anode surface relative to concentration of organics [32].

2.1.4 General mechanism for the oxidation of organics on active and non-active electrodes [33, 31]

In general, anodic oxidation of organics may proceed either via direct or indirect oxidation process. In direct electrochemical oxidation, electron exchange occurs between the organic species and the electrocatalytic electrode surface. In indirect electrochemical oxidation, the organic compounds exchange electrons with the anode surface through mediation of electroactive species. This intermediation may be homogeneous (using dissolved mediators in the electrolyte, e.g., Ag^{2+}/Ag^+ , Ce^{4+}/Ce^{3+}) or heterogeneous, in which mediators are fixed at the electrode surface. In the latter case, both its reaction with organics and its regeneration take place at the electrode surface.

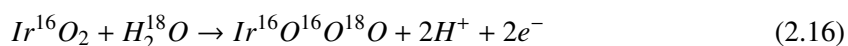
In our laboratory, it has been found that the nature of the electrode material influences strongly both the selectivity and the efficiency of the organics mineralization. Furthermore, it was demonstrated that frequently oxidation of organics occurs, without any loss in electrode activity, only at high potentials, in the domain of O_2 evolution. In order to explain these observations, a general

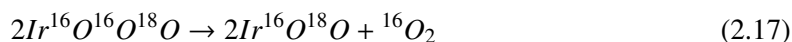
model for anodic oxidation of organics in acid aqueous solutions has been proposed (Fig. 2.5). According to this model, the initial step of oxidation process is the discharge of water molecules to hydroxyl radicals (reaction 1). The electrochemical and chemical reactivity of these hydroxyl radicals depends strongly on the nature of anode material (M). Two extreme cases can be distinguished:

- At *active* (electrocatalytic) electrode, there is a strong interaction between the electrode surface (M) and hydroxyl radicals. In this case, there is possible transition of the oxygen from the hydroxyl radicals to the anode surface resulting in formation of the so-called higher oxide (reaction 2). The surface redox couple MO / M can act as mediator in the oxidation of organics (reaction 3) which may result in the partial (selective) oxidation of organics. This reaction is in competition with the side reaction of O₂ evolution due to the decomposition of the higher oxide (reaction 4).
- At *non-active* (non-electrocatalytic) electrode there is a weak interaction between the electrode surface (M) and hydroxyl radicals. In this case, the oxidation of organics is mediated by hydroxyl radicals, which may result in fully oxidized reaction products such as CO₂ (reaction 5). This reaction is also in a competition with the side reaction of hydroxyl radical discharge to oxygen (reaction 6).

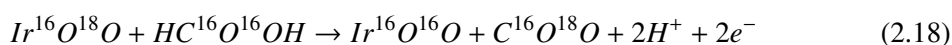
In summary, the electrochemical activity (overpotential for oxygen evolution) and chemical reactivity (rate of organics oxidation) of adsorbed HO• depends on the strength of M-OH interaction. In general, the weaker is this interaction, the lower is the anode reactivity toward oxygen evolution and the higher is the anode reactivity for organics oxidation (fast chemical reaction).

IrO₂ is a typical example of an *active* electrode with a high electrocatalytic activity for O₂ evolution (low overvoltage anode). Recently, Fierro et al. [34] have demonstrated, using differential electrochemical mass spectrometry (DEMS) together with ¹⁸O labelling, that iridium oxide layer indeed participates in both the oxygen evolution reaction and organics oxidation what confirmed the proposed model. The authors have found that oxygen evolution on Ir¹⁶O₂ in H₂¹⁸O containing electrolyte results in formation of Ir¹⁶O¹⁸O according to Eqs.2.16–2.17.





Furthermore, they have observed that ^{18}O -labelled iridium dioxide results in formation of $^{16}O^{18}O$ and $^{18}O_2$ what proves that oxygen evolution reaction proceeds via mediation of IrO_3/ IrO_2 redox couple. In the second part of their experiment [35], oxidation of formic acid was performed on $Ir^{16}O^{18}O$. During the experiment, $C^{16}O^{18}O$ evolution was observed showing that the IrO_2 coating participated in an oxidation process (Eq. 2.18).



Boron-doped diamond anode is a typical example of *non-active electrode* which does not participate in the anodic reaction and does not provide any catalytic active sites for adsorption of reactants on its surface. BDD (high overvoltage anode) can be considered as an inert substrate, which acts as a sink (or supplier) for removal of electrons.

2.2 Differential electrochemical mass spectrometry [36, 37, 38]

Electrochemical mass spectrometry (EMS) is a technique which allows detection of electrochemical reaction products shortly after their formation. This is achieved by interfacing an electrochemical cell to a conventional mass spectrometer (MS) via a porous membrane which transfers all volatile species formed during continuous electrochemical reaction. In an experiment, the ion current corresponding to a given species of interest is measured simultaneously with the faradaic current during a potential sweep (cyclic voltammetry), resulting in the so-called mass spectrometric cyclic voltammogram (MSCV) and a cyclic voltammogram (CV), respectively.

The possibility of measuring electrochemical reaction products by connecting the electrochemical cell to a mass spectrometer was first suggested by Bruckenstein and Gadde in 1971 [39]. The authors connected a working electrode to a porous membrane with non-wetting properties, which was used as the interface between the electrochemical cell and the inlet of MS. In their setup, the delay of response for the volatile products entering the MS was about 20 seconds.

A considerable improvement of the method was achieved by Wolter and Heitbaum in 1984 [40]. The authors used a differential pumping system with turbomolecular pumps which allows a fast transfer of products from the electrochemical cell to the ionization chamber and a fast elimination of collected gases. Due to the improved vacuum system, the response time for an elec-

trochemical experiment was about 0.2 s. In this way, the faradaic current and the ionic current could be correlated without major distortions for scan rates up to 50 mV s^{-1} . In order to distinguish this technique from product sampling, i.e., an integral approach, the authors called their method differential electrochemical mass spectrometry (DEMS). Since then, the electrochemical mass spectrometry has become a powerful tool in electroanalysis and electrochemical kinetics.

2.2.1 DEMS setup

Interface to vacuum

In a typical DEMS experiment it is important to be able to separate the volatile products from the electrolyte. For aqueous and also some organic electrolytes this can be achieved by using a porous Teflon membrane. Due to its hydrophobicity, the liquid does not penetrate through it. On the contrary, dissolved gaseous and other volatile species can readily evaporate in the pores. The critical pore size of the Teflon membrane depends on the surface tension of the liquid. For aqueous electrolytes, the pore size is $< 0.8 \mu\text{m}$. Thus, a typical Teflon membrane is $75 \mu\text{m}$ thick with a porosity of 50%. Since it is very thin, in DEMS setup, the Teflon membrane is supported by a glass or steel frit.

The conventional electrochemical cell

Several electrodes and cell types have been described in the literature. In the classical approach, the electrocatalyst layer, e.g., Pt, is sputtered directly onto the Teflon membrane. In this way, one side of the electrode is in contact with the solution being electrolyzed, whereas the other side is in contact with the mass spectrometer vacuum system. The advantage of this approach is a fast transfer of the species to the vacuum and the large surface area of the electrocatalyst layer. The disadvantage, however, is the low mechanical stability and the higher thickness leading to the depletion of the species within the electrocatalyst layer (diffusion behavior). Thus, porous metal layer electrodes are not suitable for investigation of electrode reactions connected with strong gas evolution, since the strong bubbling causes destruction of the electrode. For this type of electrode, the typical electrochemical cell, made of Teflon or glass, is shown in Fig. 2.6. The volume of this cell is defined by a Teflon spacer (1) placed between the electrode and the electrochemical cell. In this configuration, the response time for an electrochemical experiment is about 0.1 s.

In order to use massive (compact) electrodes for DEMS, other types of electrochemical cells,

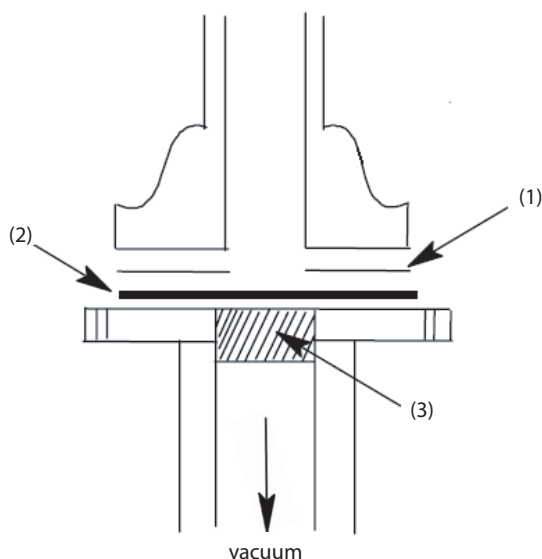


Figure 2.6. Schematic representation of the conventional electrochemical cell used in DEMS; (1) Teflon spacer, (2) working electrode, i.e., electrocatalyst layer sputtered onto porous Teflon membrane, (3) steel frit [36].

such as thin layer cell or the dual thin layer cell, were developed. In these cells, the electrode is separated from the Teflon membrane by a 50 to 100 μm electrolyte layer (defined by a Teflon spacer). In this configuration, volatile species produced at the electrode diffuse to the Teflon membrane (supported by a steel frit) within 2 seconds.

Vacuum system

Figure 2.7 shows a typical experimental DEMS setup used for the combination of cyclic voltammetry and on-line mass spectrometry. It consists of an electrochemical cell (1) attached to the inlet of a mass spectrometer via a valve at position (2), which is evacuated differentially by two turbomolecular pumps: at position (4) with a working pressure of about 10^{-2} bar, and (8), placed after the ionization chamber, with a working pressure of less than 10^{-5} mbar. The electrodes of the electrochemical cell are connected to the potentiostat driven by a function generator.

Volatile electrolysis products are ionized in the ionization chamber by electron bombardment, then the produced ions are accelerated (through quadrupole rods (7)) and analyzed with a quadrupole mass filter (m/e ratio), and finally detected by a secondary electron multiplier (10). The control of the whole instrument and data acquisition is carried out by a computer.

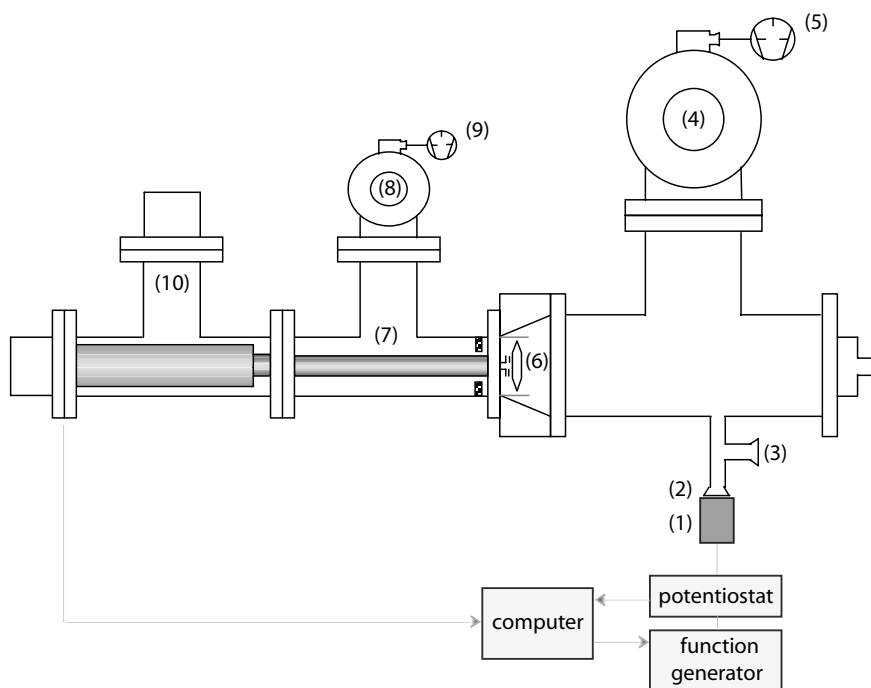


Figure 2.7. Schematic representation of a typical experimental DEMS setup; (1) electrochemical cell, (2) MS connection to the electrochemical cell, (3) connection to the calibration leak, (4) turbomolecular pump, (5) rotary pump, (6) ion source, (7) quadrupole rods, (8) turbomolecular pump, (9) rotary pump, (10) secondary electron multiplier [36, 37].

2.2.2 DEMS analysis

Using DEMS, the rate of product formation during electrochemical reaction can be easily monitored by recording the corresponding ion current. The mass spectrometrically determined ion intensity of a given species is directly proportional to its incoming flux (Eq. 2.19):

$$I_i = K^o J_i \quad (2.19)$$

where I_i (A) is the mass intensity of a given species i , K^o (C mol^{-1}) is a constant which includes all mass spectrometric constants / settings and the ionization probability of the corresponding species, and J_i (mol s^{-1}) is the flux of the species through the membrane into the ionization chamber. When the species are produced electrochemically, J_i is given by the faradaic current corresponding to that process:

$$J_i = N \frac{I_f}{zF} \quad (2.20)$$

where N is the collection efficiency, in other words, the ratio of the amount of the mass spectrometrically detected species to the total amount of species produced electrochemically, I_f (A) is the faradaic current, z is the number of electrons necessary to produce one product molecule, F (C mol^{-1}) is the Faraday constant. Combining Eqs. 2.19–2.20 one obtains:

$$I_i = NK^o \frac{I_f}{zF} \quad (2.21)$$

It is important to note that N may be less than 1 if a part of the produced species diffuses away from the electrode into the electrolyte. This occurs when not complete mixing of the electrolyte is achieved in the electrochemical cell (usually at flow rates $> 2 \mu\text{l s}^{-1}$). In this case, another equation is more appropriate:

$$I_i = K^* \frac{I_f}{z} \quad (2.22)$$

where

$$K^* = \frac{K^o N}{F} \quad (2.23)$$

Using a known electrochemical reaction, such as hydrogen / oxygen evolution, calibration of the instrument in order to find K^* for collection of H_2 / O_2 can be easily achieved using Eq. 2.22. Similarly, often the oxidation of CO adsorbed on Pt electrode is used to calibrate the mass spectrometer for CO_2 . In this case, the integrated faradaic oxidation current and ion current for CO_2 are used. Alternatively, calibration of the mass spectrometer can also be achieved via a calibration leak (valve in the position (3) in Fig. 2.7) and the K^o value can be obtained.

In summary, differential electrochemical mass spectrometry is a powerful on-line method used for both the detection of electrochemical reaction products and the study of adsorbates. Using DEMS, reaction and desorption products can be determined semi-quantitatively. As this technique is fast (response time max 2 s) and highly sensitive, the volatile reaction products below one nmol can be easily detected. Furthermore, using isotopically labelled compounds, additional information about the mechanism of the studied reaction can be obtained.

2.3 Activation of molecular oxygen

The oxygen molecule itself is a very reactive entity and forms compounds with nearly all elements. As a result, the earth's crust contains about 50% by weight of bound oxygen [41]. Activation of molecular oxygen is of importance mainly in natural systems. In a typical example, the respiratory pigments (e.g., hemoglobin) are able to fix oxygen molecules and transport them to their reaction sites. During this process oxygen carriers retain their activity, i.e., they are not irreversibly oxidized. The importance of the activation of molecular oxygen has been recognized not only in medicine and biochemistry but also in food chemistry, organic chemistry, and environmental chemistry [42, 43, 44]. In this section, activation of oxygen by organic radicals formed under irradiation is discussed [45, 46, 47, 48].

It has been reported that the direct decomposition of organic compounds (RH) under irradiation (e.g., UV-light in photolysis or X-ray / γ -ray in radiolysis) leads to formation of organic radical R^\bullet in aqueous systems (Eq. 2.24).



R^\bullet can be also formed indirectly, i.e., by interaction between RH and HO^\bullet (Eq. 2.25). The latter is formed during irradiation of water or hydrogen peroxide, as shown by Eq. 2.26–2.27.



If dissolved oxygen is present in solution, R^\bullet can react with molecular oxygen to form organic peroxy radicals RO_2^\bullet :



The yield of this process depends strongly on both the excitation rate of organics (i.e., the energy needed to form R^\bullet) and the concentration of dissolved molecular oxygen in aqueous solution.

RO_2^\bullet is a powerful oxidant and initiates subsequent chain reactions of oxidative degradation of organic compounds present in solution. It has been shown, that during this process, the peroxy radical is converted to a hydroperoxide $ROOH$, by interaction with RH or some other compound serving as a hydrogen donor (Eq. 2.29).

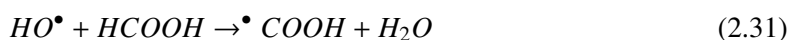


This reaction leads to regeneration of the organic free radical R^\bullet . In the absence of an efficient hydrogen atom donor or in the presence of a sufficiently high free peroxy radical concentration, RO_2^\bullet can be decomposed to hydroxyl radical (Eq. 2.30).



This chain reactions, via various possible intermediates / reactions, proceeds further leading finally to carbon dioxide, water, and inorganic salts.

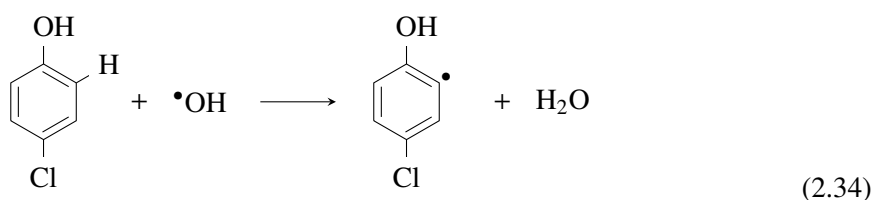
A typical example of the oxygen activation process in radiolysis is the γ -radiation induced oxidation of aerated aqueous solution of formic acid (Eqs. 2.31–2.32) [49].

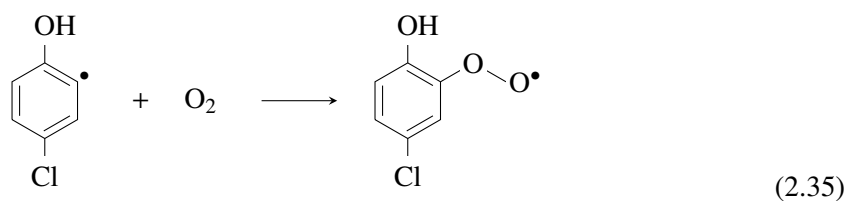


Similar example can be given for the degradation of 4-chlorophenol (4-CP) by the Fenton system, in which hydroxyl radical is generated in reaction of hydrogen peroxide with ferrous ion (Eq. 2.33).



This hydroxyl radical abstracts a hydrogen atom from 4-CP yielding a 4-chlorohydroxycyclohexadienyl radical (CIHP $^\bullet$), which subsequently reacts with oxygen to form *ortho*-parachlorophenolperoxy radical (CIPP $^\bullet$), as given by Eqs. 2.34–2.35 [46].





To sum up, in aerated aqueous solutions, dissolved oxygen increases the extent of oxidation of organic compounds. This effect is mainly due to the formation of organic peroxy radicals, which are formed by the association of organic radicals with molecular oxygen. These peroxy radicals initiate the subsequent chain reactions leading to complete oxidation of organics.

Chapter 3

Theoretical Part

In this chapter the theoretical aspect of hydroxyl radicals electrogeneration on the electrode surface in acid aqueous solutions is discussed. It is shown that, from thermodynamical point of view, electrogeneration of free hydroxyl radicals requires high anodic potential (2.38 V vs. SHE) which reflects their strong oxidizing power. In practice, the reversible potential of HO• formation is influenced notably by the anode material, i.e., by the strength of HO• adsorption on the electrode surface. On boron-doped diamond electrodes, adsorption of HO• can be assumed as negligible. Considering that quasi free hydroxyl radicals mediate the oxidation processes on BDD, the concentration profile of hydroxyl radicals during both oxygen evolution and oxidation of organic compounds can be determined. Furthermore, the change in the onset potential of HO• formation during organics oxidation, relative to that for oxygen evolution, can be predicted. This difference in the onset potential affects the current-potential curves causing their shift toward lower potentials.

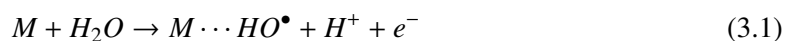
This chapter is based on the following publication:

A. Kapalka, G. Fóti and C. Comninellis. The importance of electrode material in environmental electrochemistry. Formation and reactivity of free hydroxyl radicals on boron-doped diamond electrodes, *Electrochim. Acta*, in press.

3.1 Electrogeneration of hydroxyl radicals on the electrode surface in acid aqueous solution

3.1.1 Formation of hydroxyl radicals by water discharge

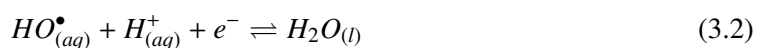
It is commonly assumed that the first step of the electrochemical oxygen evolution, from aqueous acid electrolytes, is the formation of hydroxyl radicals from water. On non-electrocatalytic electrodes (such as boron-doped diamond electrode) water is discharged at potentials above its thermodynamic stability, producing hydroxyl radicals, according to Eq. 3.1.



Although the exact nature of the interactions between the electrode surface and the hydroxyl radicals is not known, we might consider that these hydroxyl radicals are quasi free or loosely adsorbed (physisorbed). As discussed in the previous chapter, the reactivity of these hydroxyl radicals is very different from that of chemically bonded hydroxyl radicals. As a general rule, the weaker the interaction between hydroxyl radicals and electrode material, the lower is the electrochemical activity toward oxygen evolution and the higher is the chemical reactivity toward organics oxidation, as discussed extensively in [50] (see also chapter 2, sec. 2.1.4).

3.1.2 Thermodynamic aspect of free HO^\bullet formation

Considering that free hydroxyl radicals are formed in acid aqueous solution according to reaction 3.2, it is possible to calculate the thermodynamic standard potential of its formation using Eq. 3.3 [51]



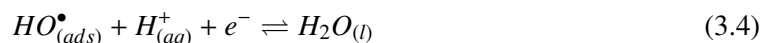
$$E^\circ = -\frac{\Delta G_r^\circ}{zF} \quad (3.3)$$

where E° (V) is the standard thermodynamic potential of reaction 3.2, ΔG_r° (kJ mol⁻¹) is the standard Gibbs free energy of the reaction, z is the number of transferred electrons, and F (C mol⁻¹) is the Faraday constant. Taking the Gibbs free energy of liquid water as -237.178 kJ mol⁻¹ [52] and that of hydroxyl radicals in the aqueous state as -7.74 kJ mol⁻¹ [52], one obtains the thermodynamic standard potential for HO^\bullet formation equal to 2.38 V [52]. Thus, from thermodynamical

point of view, electrogeneration of free hydroxyl radicals in acid aqueous solutions requires high anodic potentials. Such a high positive E° value reflects the extremely strong oxidizing power of hydroxyl radicals.

3.1.3 The influence of the anode material on the thermodynamic potential of HO• formation

The calculation of the thermodynamic potential, according to Eq. 3.3, is valid considering lack of any interactions between the HO• and the electrode material. In other words, it might be applied if the reaction occurs at an inert electrode, which only acts as a source or sink for electrons. In case of any interactions between reactants and electrode surface, one must take the Gibbs energies of adsorption of the species of interest, which, in general, are difficult to obtain [52].



It has been reported that the thermodynamic potential of HO_{ads}• formation (Eq. 3.4) is influenced notably by the strength of its adsorption on the electrode surface. As a general rule, the stronger is the adsorption, the lower is the potential of its formation [53]. Assuming that discharge of hydroxyl ions is the rate determining step of oxygen evolution in alkaline solution, Ruetschi and Delahay [54] demonstrated that the overpotential for O₂ evolution decreases approximately linearly as the electrode-hydroxyl radicals (M–OH) bond strength increases (Fig. 3.1). This observation indirectly indicates that the potential of hydroxyl radicals formation depends strongly on the strength of its adsorption on the electrode surface.

Anderson et al. [55] have reported that the reversible potential of HO• formation decreases also as the difference between HO• and H₂O adsorption energy increases. Table 3.1 gives the energy of HO• and H₂O adsorption on several metal surfaces M [56, 57, 58, 59]. The difference between M–OH and M–H₂O adsorption energy (ΔU in Table 3.1) indicates that the lowest reversible potential of HO• formation should be observed on Ni electrode. E° of HO• should increase further on Ag, Ru, Pd and Pt electrode, respectively. In fact, these results are in agreement with experimentally observed overpotentials for oxygen evolution, given in Fig. 3.1.

It can be concluded that any changes in bond strengths within reagents influence the thermodynamic potential of HO• formation and, consequently, the overpotential for oxygen evolution.

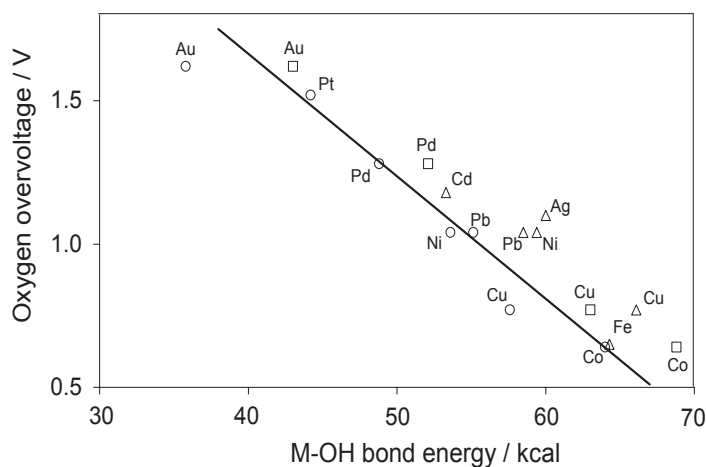


Figure 3.1. Overvoltage for O_2 evolution as a function of the metal(M)-OH bond energy. Bond energies for M-OH were calculated by three different thermodynamic cycles involving the standard enthalpy of formation of (\square) metal hydroxide, (\circ) metal oxide, and (\triangle) spectroscopic data for the dissociation of the molecule M-O. Electrolysis was performed in 1 M KOH at 1 A cm^{-2} ; $T = 25^\circ\text{C}$ [54].

Table 3.1. Energy of HO^\bullet and H_2O adsorption on several metal surfaces, calculated at the most energetically favorable (stable) positions [56, 57, 58, 59]. ΔU is the difference between HO^\bullet and H_2O adsorption energy.

Electrode M	Energy of M- H_2O (kJ mol^{-1})	Energy of M-OH (kJ mol^{-1})	ΔU kJ mol^{-1}
Ni(111)	50.2	364.0	314
Ag(100)	16.7	318.8	302
Ru(0001)	40.5	339.6	299
Pd(111)	21.2	232.5	211
Pt(111)	21.2	222.9	202

3.1.4 Electrogeneration of HO^\bullet on BDD electrode

It has been shown that, on boron-doped diamond electrodes, the onset potential of oxygen evolution reaction is about 2.3 V vs. SHE [60]. At this potential, it is thermodynamically possible to form hydroxyl radicals, as it has been discussed in section 3.1.2. In fact, Marselli et al. [29] have detected hydroxyl radicals on BDD electrode, by means of spin trapping, using electron spin resonance.

The fact that O_2 is evolved at the thermodynamic potential of HO^\bullet formation (and at potentials positive of it) may indicate that electrogenerated hydroxyl radicals on BDD surface are quasi free. This assumption is justifiable, taking into account the inert nature of diamond surface, which contains closely packed sp^3 carbon atoms, and a lack of adsorption sites [19]. It is important to note that oxygen evolution on BDD occurs at a high overpotential with respect to the thermodynamic

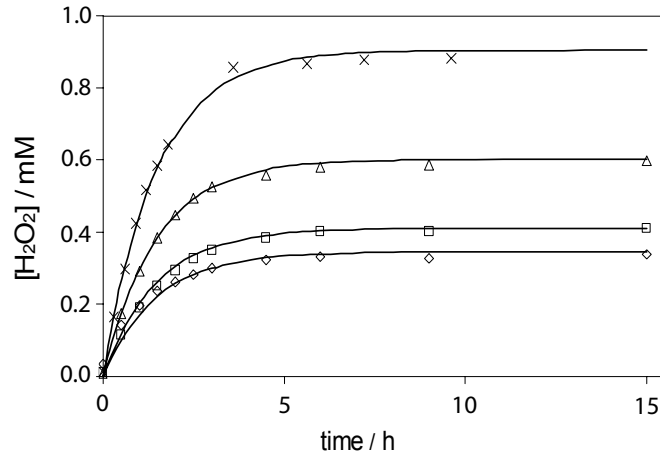


Figure 3.2. Formation of hydrogen peroxide on boron-doped diamond electrode during electrolysis in 1 M HClO₄ at different current densities: (×) 1600, (Δ) 950, (□) 470, (◇) 230 A m⁻², T = 25°C [60].

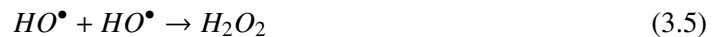
potential for O₂ formation ($E_{OER}^{\circ} = 1.23$ V vs. SHE), but very close to the thermodynamic potential of HO• formation ($E_{HO^{\bullet}}^{\circ} = 2.38$ V vs. SHE).

3.2 Concentration profile of hydroxyl radicals on BDD electrodes

In the light of the discussion in the previous section, we may consider that anodically polarized BDD electrode acts as a generator of quasi free hydroxyl radicals which mediate the oxidation processes. These reactions would take place in the reaction layer in the vicinity of the electrode surface.

3.2.1 Concentration profile of HO• during oxygen evolution

In the absence of organic compounds, electrogenerated free hydroxyl radicals can react with each other to form hydrogen peroxide, as given by Eq. 3.5. In fact, Michaud et al. [60] have detected hydrogen peroxide on BDD during electrolysis in 1 M HClO₄ at different current densities (Fig. 3.2).



Hydrogen peroxide can be further oxidized to oxygen either by its direct discharge on the electrode surface (Eq. 3.6) or via assistance of hydroxyl radicals (Eq. 3.7).



Assuming that the first step (Eq. 3.5) is the rate determining step and that 4 hydroxyl radicals (4 electrons) are needed for oxygen evolution, by applying one-dimensional Fick law referred to the molecular diffusion in a stagnant layer, the mass balance for hydroxyl radicals in an element of width Δx can be expressed as [22]:

$$-D_{HO^\bullet} \left[\frac{dc_{HO^\bullet}}{dx} \right]_x - 4k_{HO^\bullet} c_{HO^\bullet}^2 \Delta x = -D_{HO^\bullet} \left[\frac{dc_{HO^\bullet}}{dx} \right]_{x+\Delta x} \quad (3.8)$$

where D_{HO^\bullet} ($m^2 s^{-1}$) is the diffusion coefficient of HO^\bullet , k_{HO^\bullet} ($m^3 mol^{-1} s^{-1}$) is the rate constant of reaction 3.5, and c_{HO^\bullet} ($mol m^{-3}$) is the concentration of HO^\bullet .

If Δx goes to 0, we can write:

$$D_{HO^\bullet} \frac{d^2 c_{HO^\bullet}}{dx^2} = 4k_{HO^\bullet} c_{HO^\bullet}^2 \quad (3.9)$$

The boundary conditions are obtained by assuming that far from the electrode ($x = \infty$) concentration of hydroxyl radicals is 0, whereas at the electrode ($x = 0$) there is a surface concentration of hydroxyl radicals ($c_{HO^\bullet}^s$).

$$c_{HO^\bullet} = 0 \quad \text{at} \quad x = \infty$$

$$c_{HO^\bullet} = c_{HO^\bullet}^s \quad \text{at} \quad x = 0$$

Considering these boundary conditions, the solution of differential Eq. 3.9 gives the concentration profile of hydroxyl radicals, as a function of the distance x from the electrode surface, during oxygen evolution.

$$c_{HO^\bullet} = \frac{3D_{HO^\bullet}}{2k_{HO^\bullet} \left(x + \sqrt{\frac{3D_{HO^\bullet}}{2k_{HO^\bullet} c_{HO^\bullet}^s}} \right)^2} \quad (3.10)$$

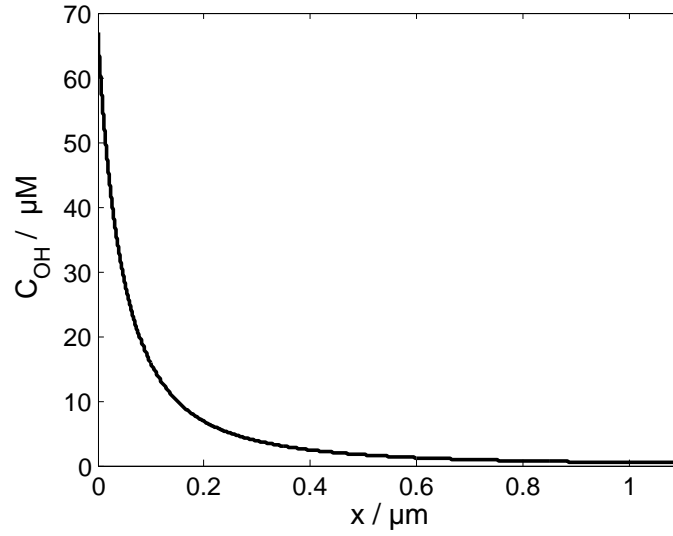


Figure 3.3. Simulated concentration profile of hydroxyl radicals during oxygen evolution according to Eq. 3.10 and 3.14; $j = 300 \text{ A m}^{-2}$, $D_{HO\bullet} = 2.2 \times 10^{-9} \text{ m}^2 \text{ s}^{-1}$, $k_{HO\bullet} = 5.5 \times 10^6 \text{ m}^3 \text{ mol}^{-1} \text{ s}^{-1}$ [61].

The gradient of the concentration can be expressed as:

$$\frac{dc_{HO\bullet}}{dx} = -\frac{3D_{HO\bullet}}{k_{HO\bullet} \left(x + \sqrt{\frac{3D_{HO\bullet}}{2k_{HO\bullet}c_{HO\bullet}^3}} \right)^3} \quad (3.11)$$

Using Eq. 3.11, it is possible to calculate the flux of hydroxyl radicals at the electrode surface, $[J_{HO\bullet}]_{x=0}$, as given by Eq. 3.12.

$$[J_{HO\bullet}]_{x=0} = -D_{HO\bullet} \left[\frac{dc_{HO\bullet}}{dx} \right]_{x=0} = 1.63 \sqrt{\left(c_{HO\bullet}^s \right)^3 k_{HO\bullet} D_{HO\bullet}} \quad (3.12)$$

The flux of hydroxyl radicals at the electrode surface can also be expressed in terms of the current density j

$$[J_{HO\bullet}]_{x=0} = \frac{j}{F} \quad (3.13)$$

where F (C mol^{-1}) is the Faraday constant.

Thus, comparing Eq. 3.12 with 3.13, the surface concentration of hydroxyl radicals during oxygen evolution (OER) can be obtained.

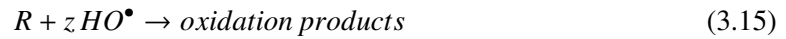
$$c_{HO\bullet_{OER}}^s = \sqrt[3]{\frac{j^2}{2.67F^2 k_{HO\bullet} D_{HO\bullet}}} \quad (3.14)$$

Figure 3.3 shows the simulated concentration profile of hydroxyl radicals during oxygen evolution as a function of the distance from the electrode surface. It can be seen that, for the investigated current density ($j = 300 \text{ A m}^{-2}$), the reaction layer thickness is about one micrometer whereas the maximum (surface) concentration of hydroxyl radicals reaches the value of several tenths of μM .

3.2.2 Concentration profile of HO^\bullet during oxidation of organic compounds

By analogy to Eq. 3.8–3.14 it is possible to determine the concentration profile of hydroxyl radicals during oxidation of organic compounds under hypotheses that:

- oxidation of organic compounds R proceeds only via assistance of hydroxyl radicals in the vicinity of the electrode surface



- concentration of organic compound is high enough to be considered as a constant in the reaction layer
- oxygen evolution, via H_2O_2 oxidation, is negligible

The two latter hypotheses apply to the charge-transfer controlled region in which the reaction is controlled by the applied current, as reported previously in [50] (see also chapter 2, sec. 2.1.3).

Under these hypotheses, the mass balance for hydroxyl radicals leads to Eq. 3.16 and 3.17

$$-D_{\text{HO}^\bullet} \left[\frac{dc_{\text{HO}^\bullet}}{dx} \right]_x - z k_R c_{\text{HO}^\bullet} c_R \Delta x = -D_{\text{HO}^\bullet} \left[\frac{dc_{\text{HO}^\bullet}}{dx} \right]_{x+\Delta x} \quad (3.16)$$

$$D_{\text{HO}^\bullet} \frac{d^2 c_{\text{HO}^\bullet}}{dx^2} = z k_R c_{\text{HO}^\bullet} c_R \quad (3.17)$$

where z is the number of electrons involved in oxidation of organic compound, k_R ($\text{m}^3 \text{ mol}^{-1} \text{ s}^{-1}$) is the rate constant of reaction 3.15, and c_R (mol m^{-3}) is the concentration of organic compound. The boundary conditions are obtained by assuming that far from the electrode ($x = \infty$) concentration of hydroxyl radicals is 0, whereas at the electrode ($x = 0$) there is a surface concentration of hydroxyl radicals ($c_{\text{HO}^\bullet}^s$).

$$c_{\text{HO}^\bullet} = c_{\text{HO}^\bullet}^s \quad \text{at} \quad x = 0$$

$$c_{HO^\bullet} = 0 \quad \text{at} \quad x = \infty$$

Thus, by solving Eq. 3.17 one can obtain the concentration profile of hydroxyl radicals during oxidation of organic compounds.

$$c_{HO^\bullet} = c_{HO^\bullet}^s \exp\left(-\sqrt{\frac{zk_R c_R}{D_{HO^\bullet}}} x\right) \quad (3.18)$$

The gradient of the concentration can be expressed as:

$$\frac{dc_{HO^\bullet}}{dx} = -c_{HO^\bullet}^s \sqrt{\frac{zk_R c_R}{D_{HO^\bullet}}} \exp\left(-\sqrt{\frac{zk_R c_R}{D_{HO^\bullet}}} x\right) \quad (3.19)$$

Using Eq. 3.19, the flux of hydroxyl radicals at the electrode surface, $[J_{HO^\bullet}]_{x=0}$, can be expressed as:

$$[J_{HO^\bullet}]_{x=0} = -D_{HO^\bullet} \left[\frac{dc_{HO^\bullet}}{dx} \right]_{x=0} = c_{HO^\bullet}^s \sqrt{zk_R c_R D_{HO^\bullet}} \quad (3.20)$$

Comparing Eq. 3.20 with 3.13, the surface concentration of hydroxyl radicals during oxidation of organic compounds is obtained.

$$c_{HO^\bullet}^s = \frac{j}{F \sqrt{zk_R c_R D_{HO^\bullet}}} \quad (3.21)$$

In the presence of organic compound, the concentration of hydroxyl radicals decreases exponentially (Eq. 3.18) with the distance from the electrode surface. The thickness of the reaction layer (reaction cage) depends on the concentration of organic compound, the rate constant of organics oxidation via hydroxyl radicals, and the applied current density. As a typical example, Fig. 3.4 shows the simulated HO^\bullet concentration profile during oxidation of formic acid (0.25–1 M) at 300 A m^{-2} . It can be seen that the higher is the formic acid concentration, the lower is the surface concentration of HO^\bullet and the smaller is the thickness of the reaction layer. For the investigated concentrations of formic acid, the thickness of the reaction layer (reaction cage) drops down to barely tenths of nanometers, which is significantly lower as compared with that in the absence of organics (Fig. 3.3). Figure 3.5 shows the comparison of HO^\bullet concentration profile for 1 M formic acid, methanol, and ethanol. Depending on the rate constant, the thickness of the reaction layer varies between few nanometers and tenths of nanometers.

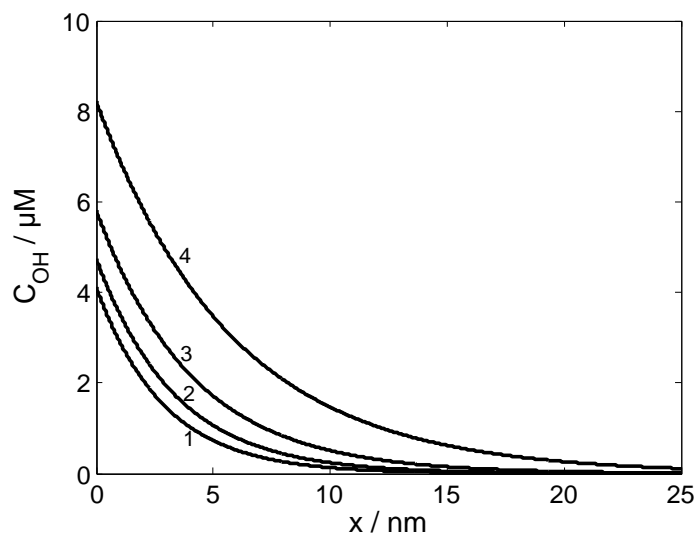


Figure 3.4. Simulated concentration profile of hydroxyl radicals during oxidation of (1) 1 M, (2) 0.75 M, (3) 0.5 M, and (4) 0.25 M formic acid, according to Eq. 3.18 and 3.21; $j = 300 \text{ A m}^{-2}$, $D_{HO\cdot} = 2.2 \times 10^{-9} \text{ m}^2 \text{ s}^{-1}$, $k_{HCOOH} = 1.3 \times 10^5 \text{ m}^3 \text{ mol}^{-1} \text{ s}^{-1}$ [61], $z = 2$.

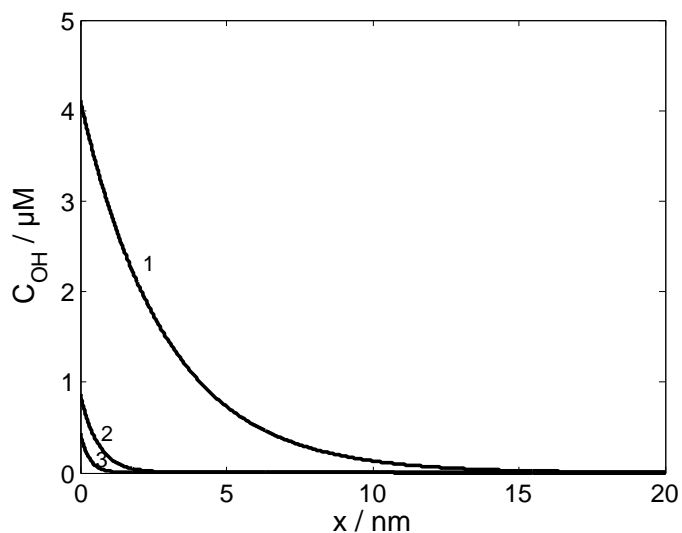


Figure 3.5. Simulated concentration profile of hydroxyl radicals during oxidation of 1 M (1) formic acid, and (2) methanol, (3) ethanol, according to Eq. 3.18 and 3.21; $j = 300 \text{ A m}^{-2}$, $D_{HO\cdot} = 2.2 \times 10^{-9} \text{ m}^2 \text{ s}^{-1}$, $k_{HCOOH} = 1.3 \times 10^5 \text{ m}^3 \text{ mol}^{-1} \text{ s}^{-1}$, $k_{CH_3OH} = 9.7 \times 10^5 \text{ m}^3 \text{ mol}^{-1} \text{ s}^{-1}$, $k_{C_2H_5OH} = 1.9 \times 10^6 \text{ m}^3 \text{ mol}^{-1} \text{ s}^{-1}$ [61], $z = 2, 6$ and 12 for formic acid, methanol and ethanol, respectively.

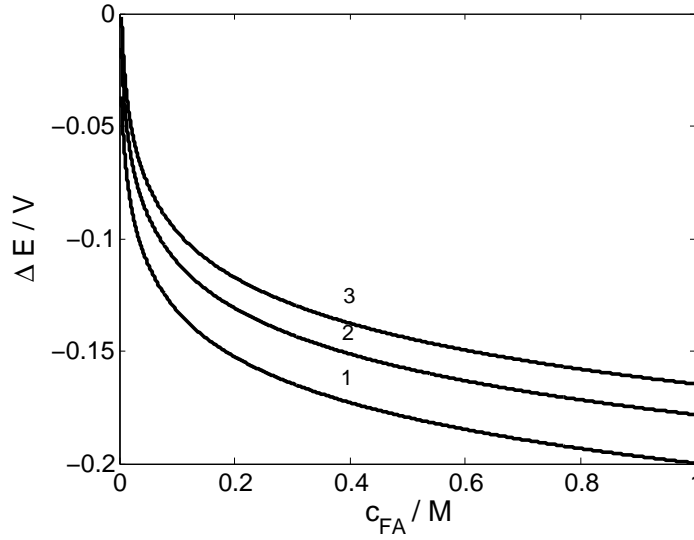


Figure 3.6. The shift of the potential, ΔE , according to Eq. 3.25 as a function of formic acid concentration at several current densities: (1) 50 A m^{-2} , (2) 150 A m^{-2} , (3) 300 A m^{-2} ; $D_{HO^\bullet} = 2.2 \times 10^{-9} \text{ m}^2 \text{ s}^{-1}$, $k_{HO^\bullet} = 5.5 \times 10^6 \text{ m}^3 \text{ mol}^{-1} \text{ s}^{-1}$, $k_{HCOOH} = 1.3 \times 10^5 \text{ m}^3 \text{ mol}^{-1} \text{ s}^{-1}$ [61], $z = 2$.

3.3 Shift of water discharge potential during organics oxidation

Consider the discharge of water to hydroxyl radicals in acid aqueous solution given in Eq. 3.22.



As discussed in the previous section, due to the high reactivity of formed HO^\bullet , the following coupled reactions can occur in the absence (Eq. 3.23) and presence of organic compound in the solution (3.24). For simplicity, in the latter case, the oxygen evolution reaction, via H_2O_2 oxidation, is neglected.



Oxidation of organics (reaction 3.24) adds a channel for disappearance of HO^\bullet . As a consequence, the HO^\bullet concentration profile does not extend as far into the bulk, as it would in the absence of coupled reaction 3.24. This difference in the concentration (disappearance rate) of HO^\bullet affects the current-potential curves causing a shift of the potential in the presence of organic compounds.

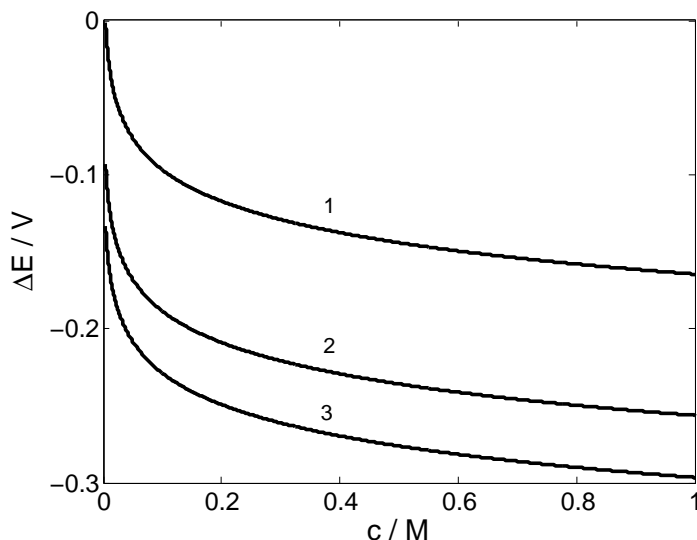


Figure 3.7. The shift of the potential, ΔE , according to Eq. 3.25 as a function of concentration for several organic compound: (1) formic acid, (2) methanol, (3) ethanol; $j = 300 \text{ A m}^{-2}$, $D_{HO^\bullet} = 2.2 \times 10^{-9} \text{ m}^2 \text{ s}^{-1}$, $k_{HO^\bullet} = 5.5 \times 10^6 \text{ m}^3 \text{ mol}^{-1} \text{ s}^{-1}$, $k_{HCOOH} = 1.3 \times 10^5 \text{ m}^3 \text{ mol}^{-1} \text{ s}^{-1}$, $k_{CH_3OH} = 9.7 \times 10^5 \text{ m}^3 \text{ mol}^{-1} \text{ s}^{-1}$, $k_{C_2H_5OH} = 1.9 \times 10^6 \text{ m}^3 \text{ mol}^{-1} \text{ s}^{-1}$ [61], $z = 2, 6$ and 12 for formic acid, methanol and ethanol, respectively.

Applying Nernst equation for reaction 3.22, the shift of potential, ΔE , caused by organics oxidation, relative to oxygen evolution, can be expressed as:

$$\Delta E = \frac{RT}{zF} \ln \frac{c_{HO_R^\bullet}^s}{c_{HO_{OER}^\bullet}^s} \quad (3.25)$$

where z is the number of exchanged electrons ($z = 1$), R ($\text{J mol}^{-1} \text{ K}^{-1}$) is the gas constant, T (K) is the temperature, and $c_{HO_R^\bullet}^s$ and $c_{HO_{OER}^\bullet}^s$ (mol m^{-3}) is the surface concentration of hydroxyl radicals during oxidation of organic compound and during oxygen evolution, respectively.

The ΔE value gives the shift of the potential in a negative direction, i.e., the shift of the current-potential curves toward lower potentials provided that $c_{HO_R^\bullet}^s < c_{HO_{OER}^\bullet}^s$. Under this condition, during organics oxidation, HO^\bullet should disappear from the electrode surface faster than during oxygen evolution. Inserting the surface concentration of hydroxyl radicals estimated during oxygen evolution and organics oxidation (Eqs. 3.14 and 3.21, respectively) to Eq. 3.25, in presence of organics, the shift of the potential with respect to the potential for oxygen evolution can be determined.

Figure 3.6 shows ΔE as a function of formic acid concentration for the current density in the range of $50\text{--}300 \text{ A m}^{-2}$. For investigated current densities and concentrations, the maximal shift toward lower potentials is in the range of $0.16\text{--}0.20 \text{ V}$. At first, ΔE changes very fast with the concentration (up to $\sim 100 \text{ mM}$), and then tends to stabilize. Furthermore, the higher is the

current density, the smaller is ΔE . Figure 3.7 shows ΔE for formic acid, methanol and ethanol, investigated at 300 A m^{-2} . It can be seen that the higher is the rate constant of organics oxidation, k_R , the higher shift of potential is obtained.

3.4 Conclusions

On boron-doped diamond electrodes, the onset potential of oxygen evolution reaction is at about 2.3 V vs. SHE. This potential is close to the thermodynamic potential of hydroxyl radicals formation (2.38 V vs. SHE) which allows to suppose that quasi free hydroxyl radicals are formed on BDD surface during water discharge. This assumption is acceptable in view of the inert nature of the diamond surface.

Anodically polarized BDD electrode can be considered as a generator of free HO^\bullet which mediate the oxidation processes in the vicinity of the electrode surface. Oxidation of organic compounds via hydroxyl radicals affects the current-potential (I – V) curves causing their shift toward lower potentials with respect to the potential of the electrolyte decomposition (oxygen evolution). In fact, the higher is the rate constant of organics oxidation and organics concentration, the higher shift of potential is expected. Supposing that water discharge to free hydroxyl radicals on BDD is governed by Nernst equation, the shift of the I – V curves toward lower potential can be evaluated using the concentration of hydroxyl radicals at the anode surface in the absence and presence of organics compounds.

Chapter 4

Oxygen Evolution Reaction on BDD; A Kinetic Study

In this chapter, kinetics of OER is investigated in 1 M HClO₄ on the BDD macroelectrode and the BDD microelectrodes-array (MEA). The correction of the anodic polarization curve for ohmic drop has been performed on BDD macroelectrode taking into account the total uncompensated resistance of the studied system. On BDD MEA, no correction of the polarization curve was necessary due to the small contribution of ohmic drop to the measured potential. The analysis of experimental data showed that at low overpotential (< 1.2 V), abnormally high Tafel slopes (340 and 680 mV dec⁻¹ on BDD MEA and BDD, respectively) have been observed, whereas in the high overpotential region (> 1.2 V), the Tafel slope has been found to equal 120 mV dec⁻¹. The apparent activation enthalpy for OER, evaluated at the equilibrium potential, was 91 kJ mol⁻¹. Such high apparent activation enthalpy is consistent with high overpotential for OER on diamond electrodes with respect to E_{OER}^o . The Tafel slope of 120 mV dec⁻¹ and zero reaction order with respect to H⁺ concentration allowed to draw conclusions about the rate determining step of OER on BDD.

This chapter is based on the following publications:

A. Kapałka, G. Fóti and C. Comninellis. Investigations of electrochemical oxygen transfer reaction on boron-doped diamond electrodes, *Electrochim. Acta*, 53 (2007) 1954

A. Kapałka, G. Fóti and C. Comninellis. Determination of the Tafel slope for oxygen evolution on boron-doped diamond electrodes, *Electrochem. Comm.*, 10 (2008) 607

4.1 Introduction

It has been reported that the oxygen evolution reaction on boron-doped diamond (BDD) electrodes appears at high overpotentials (higher than 1 V) and results in abnormally high Tafel slope (b -coefficient). Santana et al. [16] reported b -coefficients between 220 and 415 mV dec⁻¹, Janssen and Blijlevens [62] 430 mV dec⁻¹, Beck et al. [17] between 200 and 500 mV dec⁻¹, Katsuki et al. [18] between 150 and 250 mV dec⁻¹, Panizza and Cerisola [63] 230 mV dec⁻¹. Such unusually high Tafel slope has been attributed either to a potential drop in the space-charge layer of BDD (considered as a p -type semiconductor) [17], or to the accumulation of bubbles/oxygen species on the electrode surface (blockage of the surface) [18]. Nevertheless, no evidence for any of those hypotheses has been found so far.

In fact, the investigation of kinetics of the gas-evolving reactions is difficult due to the formation of gas bubbles at the electrode surface [64, 65]. The nucleation of bubbles depends on the saturation degree of the gas in the liquid, which is controlled by the mass transfer and the current density. In general, during gas evolution, the electrode surface is covered with a fixed layer of gas bubbles, depending on the current density and the nature of the anode surface. The state of the electrode surface is important because the bubbles are formed at active nucleation sites i.e. on irregularities of the surface. Thus, taking it into account, the nucleation of bubbles on BDD surface might be important due to its high roughness [66]. Bubble formation not only reduces the active surface area of the electrode but also influences the ohmic resistance. Both of these factors may influence the electrochemical response resulting in distortion of the polarization curves. Thus, in order to obtain meaningful data it is necessary to perform an appropriate correction of polarization curves before their analysis.

In this chapter, kinetics of OER in 1 M HClO₄ on both BDD macroelectrode and BDD microelectrodes-array (MEA) has been studied. Microelectrodes have many advantages over macroelectrodes, like small ohmic drop, small capacitive background current, superior mass transportation (spherical diffusion) and possibility to work at very high scan rates [67]. The correction of the anodic polarization curves for ohmic drop has been performed using the method of Shub et Reznik [68]. The investigation of Tafel slope, the reaction order with respect to H⁺ and the apparent enthalpy for OER has been carried out. On the basis of obtained results, a mechanism of OER and the involved rate-determining step have been proposed.

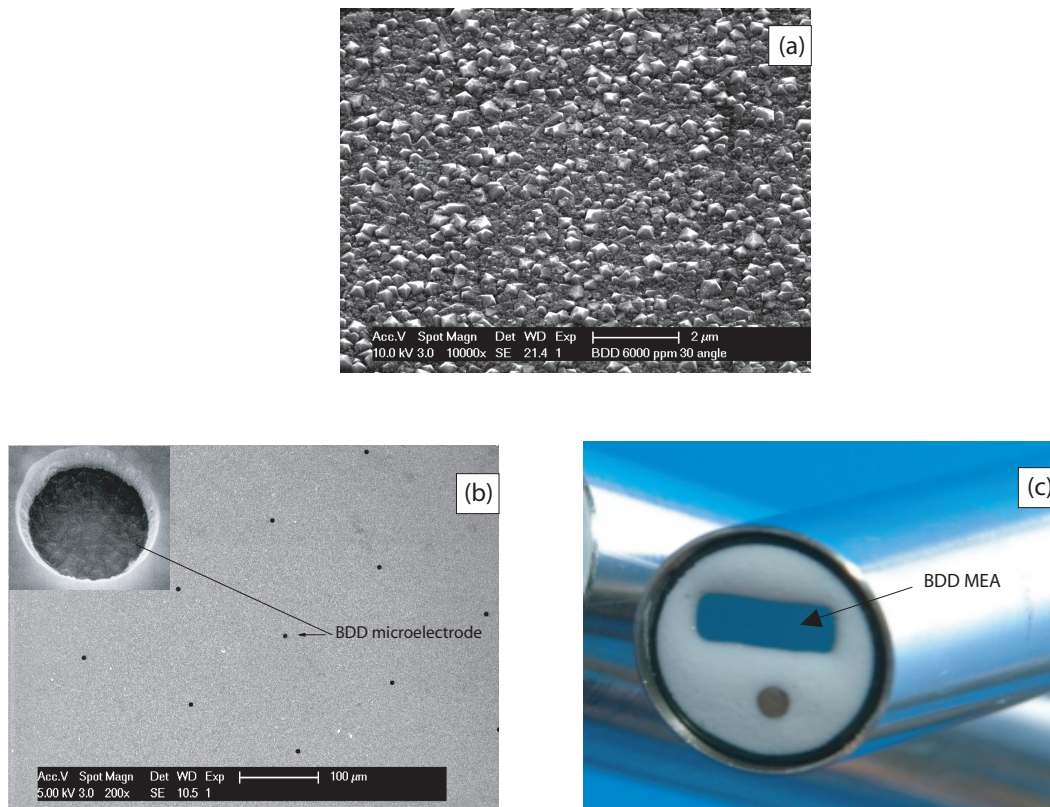


Figure 4.1. SEM micrograph of (a) the boron-doped diamond (BDD) thin film electrode, (b) the boron-doped diamond microelectrodes-array (BDD MEA); the diameter of the single microelectrode in BDD MEA (shown in inset) is 5 μm and the spacing between microelectrodes is 150 μm ; (c) BDD MEA used device.

4.2 Experimental details

Preparation of BDD anodes

The boron-doped diamond thin film electrodes were synthesized at the Centre Suisse d'Electronique et de Microtechnique SA (CSEM), Switzerland, by the hot-filament chemical vapor deposition technique (HF-CVD) using a low-resistivity p-Si substrate (p-Si/BDD). The filament temperature was 2500°C and that of the substrate was about 830°C. The reactive gas was a mixture of 1 % CH_4 in H_2 containing $\text{B}(\text{CH}_3)_3$ as a boron source. A gas flow of 5 $\text{dm}^3 \text{min}^{-1}$ was supplied to the reaction chamber giving a diamond film growth rate of 0.24 $\mu\text{m h}^{-1}$. As a result, the randomly textured, polycrystalline diamond layer on p-Si substrate was obtained (Fig. 4.1a). The boron

/carbon ratio (B/C) in the diamond film was either 1000 or 6000 ppm.

The boron-doped diamond microelectrodes-arrays (BDD MEA) were fabricated at Adamant Technologies SA, Switzerland, by covering the BDD layer (B/C 1000 ppm) with a Si_3N_4 film, 0.5 μm in thickness. The patterning of the Si_3N_4 layer was performed by a standard photolithography technique through dry etching to form a hexagonal array of 473 microdiscs, 5 μm in diameter and separated by 150 μm (Fig. 4.1b).

Electrochemical measurements

Electrochemical measurements were carried out in a single-compartment, three-electrode cell using an Autolab PGSTAT 30. The counter electrode was a Pt wire, the working electrode was BDD macroelectrode or BDD MEA (both B/C 1000 ppm) and the reference electrode was $\text{Hg}/\text{Hg}_2\text{SO}_4/\text{K}_2\text{SO}_4$ (sat) (MSE; 0.64 V vs. SHE). The area of BDD was 0.785 cm^2 whereas the area of BDD MEA was calculated as a sum of individual microelectrodes in the array ($9.3 \times 10^{-5} \text{ cm}^2$). Before starting the measurements, BDD MEA was treated by potential scanning from 0.5 to 2.1 V vs. MSE at 2 mV s^{-1} , whereas BDD macroelectrode was treated for 30 minutes at 10 mA cm^2 . All voltammetric measurements were performed in 1 M HClO_4 as a supporting electrolyte. The voltammograms, at scan rates $> 10 \text{ V s}^{-1}$, were recorded on BDD MEA using fast scan voltammetry.

Ohmic drop correction

The correction of polarization curves for ohmic drop was performed according to the method described in [68, 69, 70] assuming that the experimentally observed overpotential η (V) at any current is given by Eq. 4.1

$$\eta = a + b \ln j + jR \quad (4.1)$$

where a (V) is the Tafel constant, b (V dec^{-1}) is the Tafel slope, j (A cm^{-2}) is the current density, and R ($\Omega \text{ cm}^2$) is the total area-specific uncompensated resistance of the system assumed to be constant and independent of current. Differentiating Eq. 4.1 with respect to current density gives Eq. 4.2 from which b and R can be easily obtained by plotting $d\eta/dj$ vs. $1/j$.

$$\frac{d\eta}{dj} = \frac{b}{j} + R \quad (4.2)$$

Knowledge of R allows correction of the experimental overpotential by subtraction of ohmic drop, jR , according to Eq. 4.3.

$$\eta_{corr} = \eta - jR \quad (4.3)$$

In the numerical calculation, the derivative $d\eta/dj$ was replaced by $\Delta\eta/\Delta j$ calculated from each pair of consecutive experimental points.

Activation enthalpy

The apparent activation enthalpy was derived from the polarization curves recorded at different temperatures according to the theory in [71, 72, 73]. For electrochemical reactions, the rate of reaction is proportional to the current density j and can be written in terms of Arrhenius equation (Eq. 4.4)

$$j = P \exp\left(-\frac{\Delta H}{RT}\right) \quad (4.4)$$

where P is a constant, independent of temperature and electrode potential, and ΔH (kJ mol^{-1}) is the apparent activation enthalpy of oxidation expressed with Eq. 4.5

$$\Delta H = \Delta H^o - \alpha F \eta \quad (4.5)$$

where η (V) is the overpotential, α is the charge transfer coefficient assumed to be independent of both temperature and potential, and ΔH^o (kJ mol^{-1}) is the activation enthalpy at the equilibrium potential assumed to be independent of temperature. ΔH^o is related to the internal energy of activation as given below [67]:

$$\Delta H^o = \Delta E^o + \Delta(pV) \quad (4.6)$$

where p is the pressure and V is the volume of the system. Thus, by plotting $\log j$ vs. $1/T$ at a constant overpotential the activation enthalpy, ΔH , can be derived from the slope of the polarization curves.

The overpotential η for OER was calculated with respect to $E_{\text{OER}}^o = 1.23$ V vs. SHE assuming negligible effect of the temperature on E_{OER}^o .

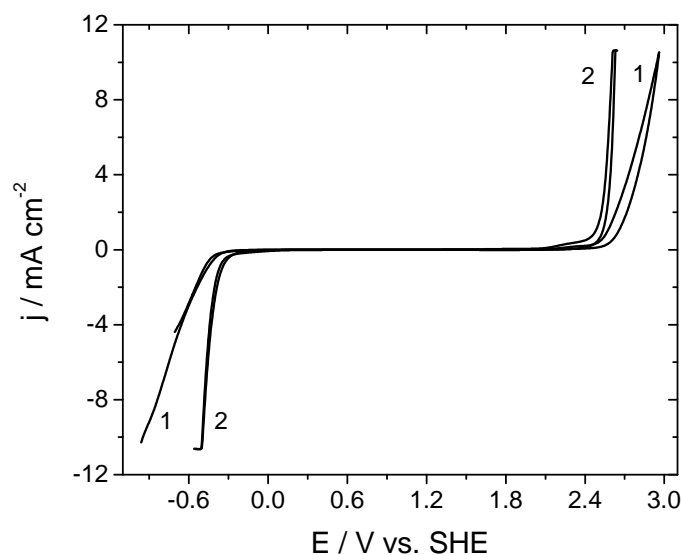


Figure 4.2. Cyclic voltammogram of (1) boron-doped diamond (BDD) macroelectrode and (2) BDD microelectrodes-array (MEA) recorded in 1 M HClO₄ at 50 mV s⁻¹; T = 25°C.

Reaction order

The electrochemical reaction order p_i was derived from the dependence of the \log of concentration c_i of particular species on the \log of reaction rate (expressed in terms of current density j) at a constant potential E (Eq. 4.7), according to the theory in [74].

$$\left(\frac{\partial \log j}{\partial \log c_i} \right)_{c_{j \neq i}, E} = p_i \quad (4.7)$$

4.3 Results

4.3.1 Comparison of the electrochemical response of BDD and BDD MEA

4.3.1.1 Potential window

Figure 4.2 shows the voltammograms recorded on BDD macroelectrode (curve 1) and the BDD microelectrodes-array (MEA) (curve 2) in 1 M HClO₄ at 50 mV s⁻¹. In both cases, a very large potential window with respect to hydrogen and oxygen evolution can be observed, which is typical for diamond electrodes [19]. It is interesting to note, however, that potential window of BDD MEA is slightly smaller than that of BDD macroelectrode. Moreover, both hydrogen and oxygen evolution proceed on BDD MEA at smaller overpotentials. In order to understand better

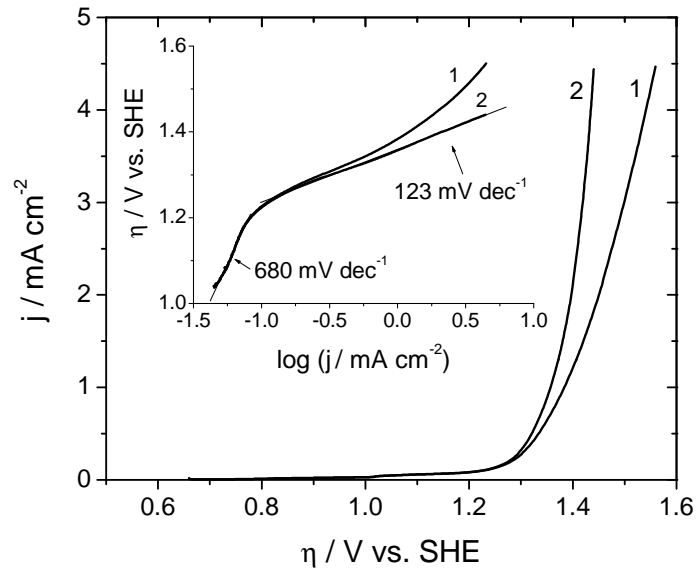


Figure 4.3. Current-overpotential curves (1) before and (2) after ohmic drop correction recorded in 1 M HClO_4 on boron-doped diamond (BDD) electrode at 1 mV s^{-1} ; $T = 25^\circ\text{C}$. Inset shows the corresponding Tafel plots.

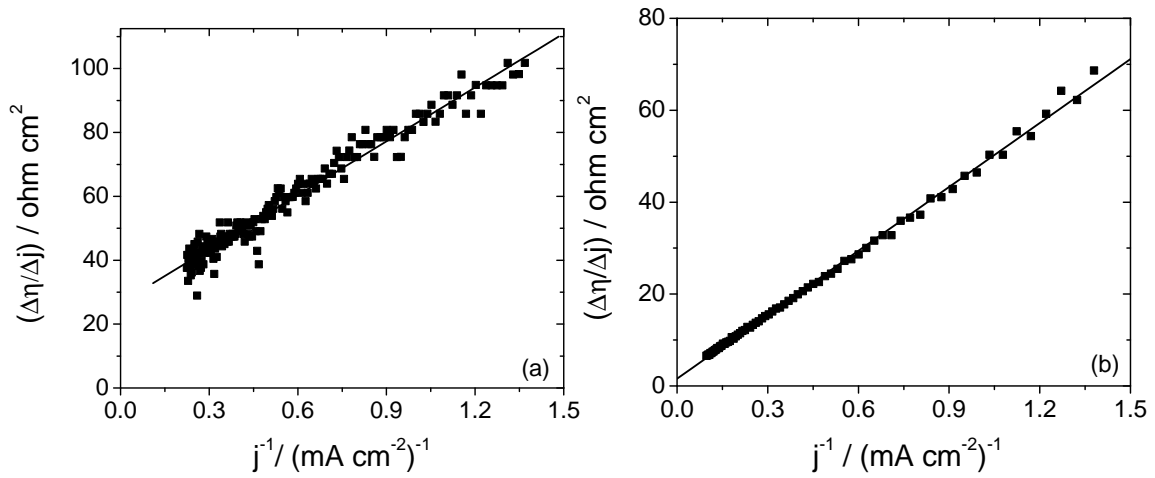


Figure 4.4. Graphical determination of uncompensated resistance (according to Eq. 4.2) from anodic polarization curves recorded on (a) boron-doped diamond (BDD) electrode (curve 1 in Fig. 4.3) and (b) boron-doped diamond microelectrodes-array (BDD MEA) (curve 1 in Fig. 4.5).

the difference between both electrodes, the Tafel plot analysis was performed.

4.3.1.2 Anodic Tafel plot

The anodic polarization curve for oxygen evolution was recorded in 1 M HClO_4 on BDD macro-electrode at the scan rate of 1 mV s^{-1} . Figure 4.3 shows the measured curve before (curve 1) and after (curve 2) correction for ohmic drop. The ohmic drop correction was performed according to

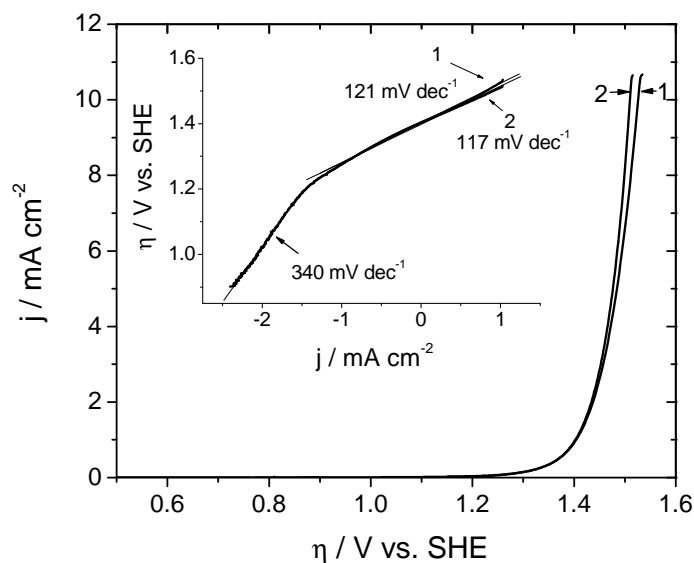


Figure 4.5. Current-overpotential curves (1) before and (2) after ohmic drop correction recorded in 1 M HClO₄ on boron-doped diamond microelectrodes-array (BDD MEA) at 2 mV s⁻¹; T = 25°C. Inset shows the corresponding Tafel plots.

Eqs. 4.1–4.3. The area-specific uncompensated resistance, equal to 27 Ω cm², was derived from the intercept of the plot of $\Delta\eta/\Delta j$ vs. $1/j$ at current densities superior to 0.7 mA cm² (> 1.35 V), i. e., in the region of pronounced contribution of ohmic drop to potential (Fig. 4.4a). From both the experimental and the corrected polarization curves, the Tafel lines were plotted in the overpotential region > 1.0 V (inset of Fig. 4.3). It can be seen that in both cases, the Tafel plot changes its slope above 1.2 V. In the high overpotential region (> 1.2 V), the uncorrected curve (curve 1) deviates strongly from linearity. Thus, no unique slope can be attributed to this curve. On the contrary, the jR -corrected polarization curve is perfectly linear and results in a Tafel slope of 123 mV dec⁻¹. In the low overpotential region (< 1.2 V), the correction for ohmic drop does not influence the Tafel plot, the slope being equal to 680 mV dec⁻¹.

Similar experiment was performed on BDD MEA. In this case, the area-specific uncompensated resistance R was found to be only 1.6 Ω cm² (Fig. 4.4b). As a consequence, the difference between polarization curve before (curve 1) and after (curve 2) ohmic drop correction is negligible (Fig. 4.5). The corresponding Tafel plots (inset of Fig. 4.5) have a slope of 340 mV dec⁻¹ in the low overpotential region and 120 mV dec⁻¹ in the high overpotential region. The change of the slope appears at overpotential of 1.2 V. It is interesting to note that, in the high overpotential region, a Tafel slope of 120 mV dec⁻¹ is obtained without ohmic drop correction.

Therefore, as electrochemical response of BDD MEA is not distorted by ohmic drop, further

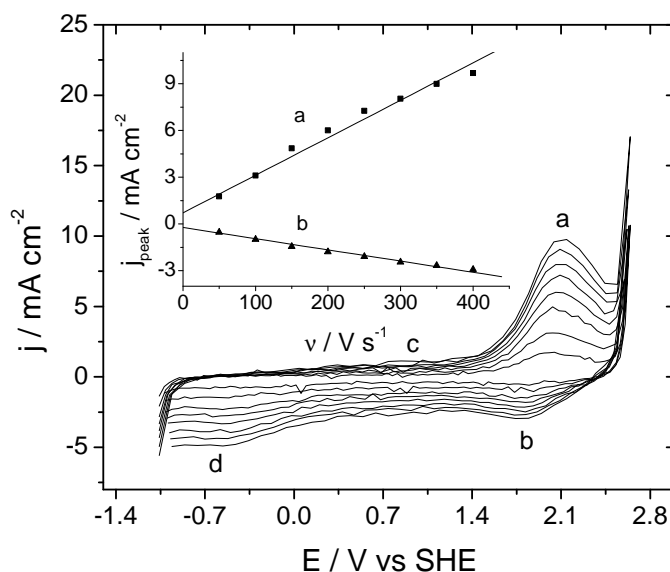


Figure 4.6. Cyclic voltammograms recorded on BDD MEA in 1 M HClO_4 at fast scan rates: 50, 100, 150, 200, 250, 300, 350, 400 V s^{-1} ; $T = 25^\circ\text{C}$. Inset shows current peak as a function of scan rate.

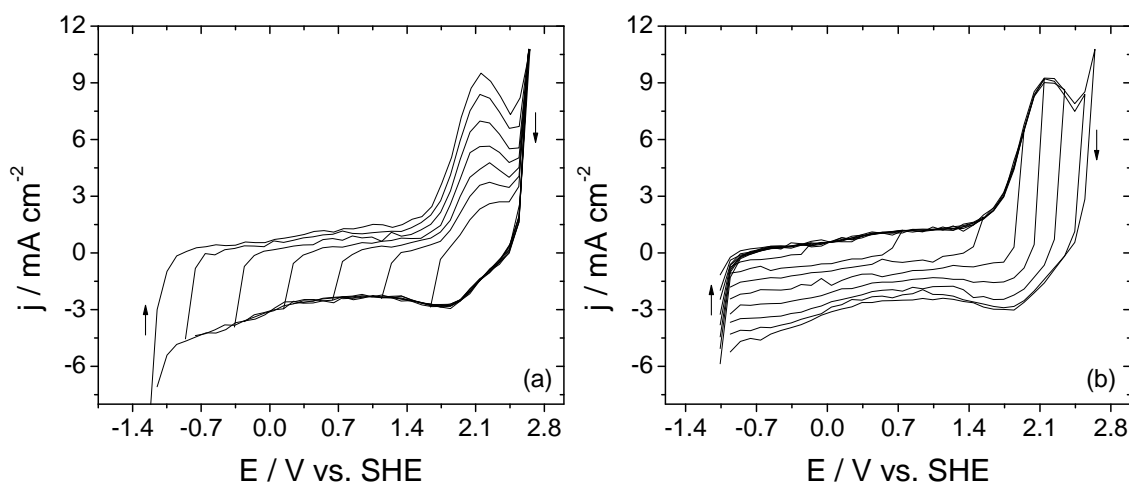


Figure 4.7. Cyclic voltammograms (5th scan) recorded on BDD MEA in 1 M HClO_4 varying the a) lower potential limit from 1.6 V to -1.2 V vs. SHE, b) upper potential limit from -0.1 V to 2.6 V vs. SHE; scan rate 400 V s^{-1} ; $T = 25^\circ\text{C}$.

measurements in this chapter are performed only on this electrode.

4.3.2 Surface redox couples

Figure 4.6 presents cyclic voltammograms recorded on BDD MEA in 1 M HClO_4 at scan rates between 50 and 400 V s^{-1} . The obtained voltammograms show that in the vicinity of oxygen evolution well-defined anodic (*a*) and cathodic (*b*) peak appear increasing linearly with the scan

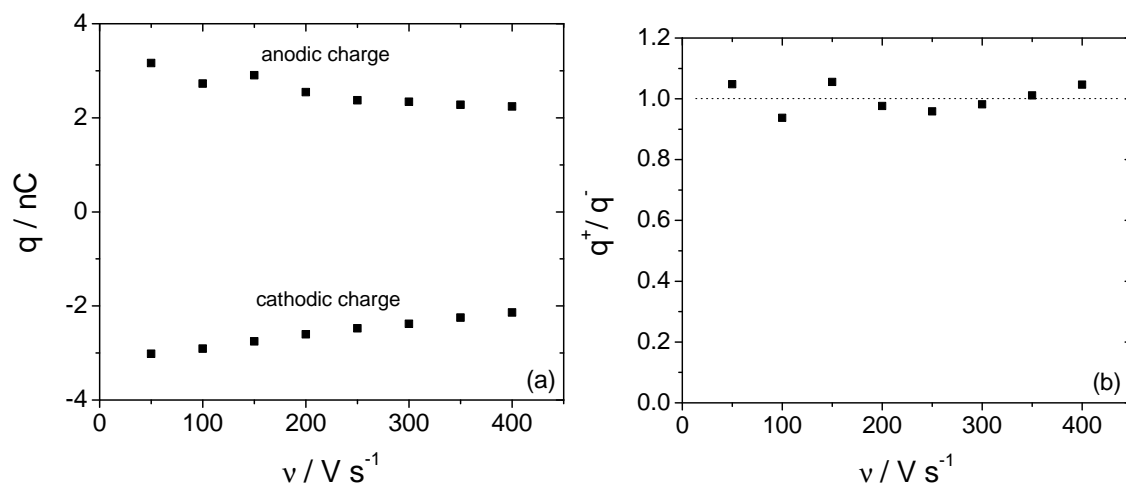


Figure 4.8. (a) Dependence of the anodic and cathodic charge, determined from Fig. 4.6, on the potential scan rate; (b) The ratio between the anodic (q^+) and cathodic (q^-) charges.

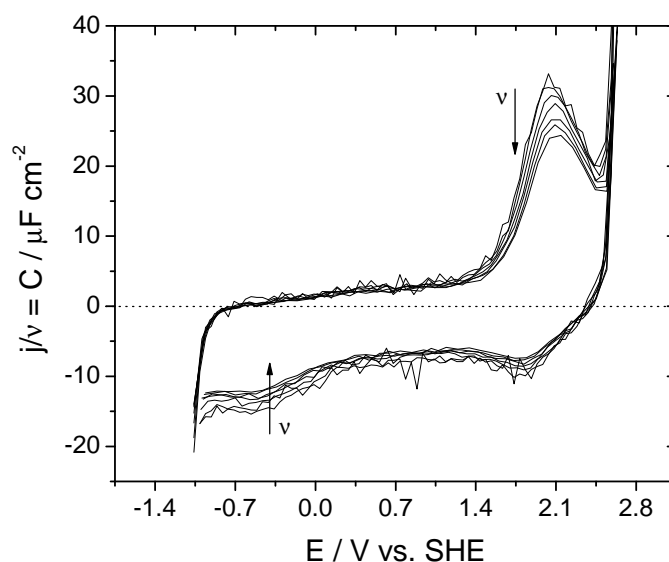


Figure 4.9. Capacitance, determined from Fig. 4.6 by dividing the current density by the scan rate, as a function of the potential; investigated scan rates: 100, 150, 200, 250, 300, 350, 400 $V s^{-1}$; $T = 25^\circ C$. The arrows show direction of the increasing scan rate.

rate (inset of Fig. 4.6). Furthermore, in the lower potential region, some additional but less pronounced peaks are present (peaks *c* and *d*). The measured pre-OER current can be attributed, as a first approximation, to existence of a redox couple at the electrode surface. In order to check its reversibility, two series of measurements were performed at the scan rate of 400 $V s^{-1}$ by changing either lower or upper limit of applied potential. Figure 4.7a presents a set of cyclic voltammograms in which the lower potential limit was decreased from 1.6 V to -1.2 V vs. SHE. It can be seen

that the lower the potential limit the higher the current in the pre-OER region (peak *a*). Varying the upper potential limit from -0.1 V to 2.6 V vs. SHE (Fig. 4.7b) both cathodic peaks (*b* and *d*) increase. These observations point out a strongly irreversible character (very slow surface process) of the redox couple observed in the lower potential region (peaks *c* and *d*). On the contrary, in the pre-OER region, appearing peaks *a* and *b* are quasi-reversible indicating relatively fast surface process.

Figure 4.8 shows the anodic and cathodic charge (evaluated from Fig. 4.6) as a function of the scan rate. Figure 4.8a demonstrates that both anodic and cathodic charges decrease slightly with the scan rate. Furthermore, the ratio between the anodic and cathodic charges is close to unity (for all investigated scan rates) indicating that the anodic current, observed mainly in the vicinity of oxygen evolution (peak *a* in Fig. 4.6), is completely regained during the cathodic sweep (Fig. 4.8b).

Figure 4.9 shows the capacitance, determined from Fig. 4.6 by dividing the current density by the scan rate, as a function of the potential. It can be seen that the capacitance depends on the scan rate mainly in the pre-OER region and between -1.2 – 0.0 V vs. SHE, whereas in the potential region between 0.3 – 1.4 V vs. SHE the signal is almost superimposed. Such behavior might be related to the existence of mainly two types of capacitance: the double layer capacitance (typically for diamond $1 - 3 \mu F \text{ cm}^{-2}$ [75]), which is independent on the scan rate, and a redox surface capacitance. The latter decreases slightly with the scan rate what is in agreement with the results in Fig. 4.8a showing a slight decrease of the charge with the scan rate.

4.3.3 Activation enthalpy

Figure 4.10a shows the polarization curves recorded on BDD MEA in 1 M HClO_4 at various temperatures (27 – 65°C). As expected, the anode potential at a given current decreased when the temperature increased due to the higher reaction rates. The apparent activation enthalpy was evaluated from the polarization curves in Fig. 4.10a according to Eqs. 4.4–4.5. By plotting $\log j$ vs. $1/T$ (Fig. 4.10b) at a constant overpotential, the activation enthalpy, ΔH , was derived from the slope of these curves. In Fig. 4.11 the apparent activation enthalpy, ΔH , is presented as a function of overpotential. In the investigated region of overpotential (potential $2.5 - 2.7$ V) ΔH is found to be between 27 and 34 kJ mol^{-1} . Extrapolation to $\eta = 0$ gave ΔH^o of 91 kJ mol^{-1} , which is about two times higher than ΔH^o reported for Pt electrodes (47 kJ mol^{-1} [76]). This high ΔH^o value is consistent with high overpotential for O_2 on BDD with respect to Pt electrode.

According to Eq. 4.5, the charge transfer coefficient, α , can be determined from the slope of

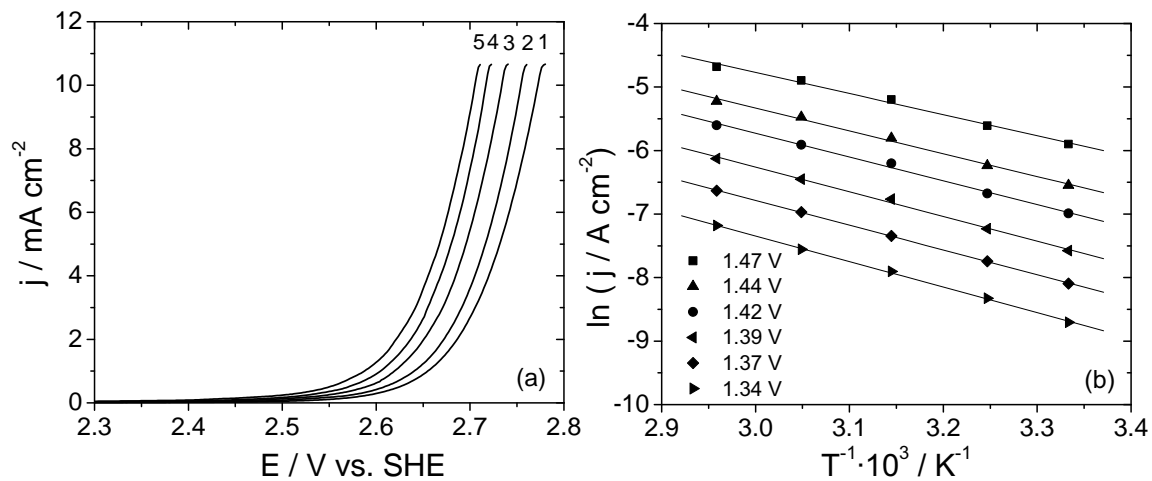


Figure 4.10. (a) Current-potential curves of BDD MEA for different temperatures (1) 27°C, (2) 35°C, (3) 45°C, (4) 55°C, (5) 65°C recorded at 2 mV s^{-1} in 1 M HClO_4 ; (b) Arrhenius plots at several overpotentials.

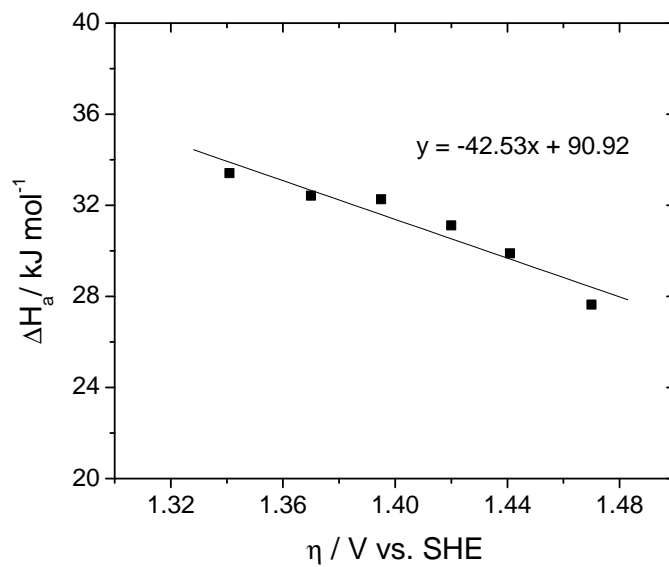


Figure 4.11. Dependence of the apparent enthalpy of electrochemical activation on overpotential; Experimental conditions as in Fig. 4.10.

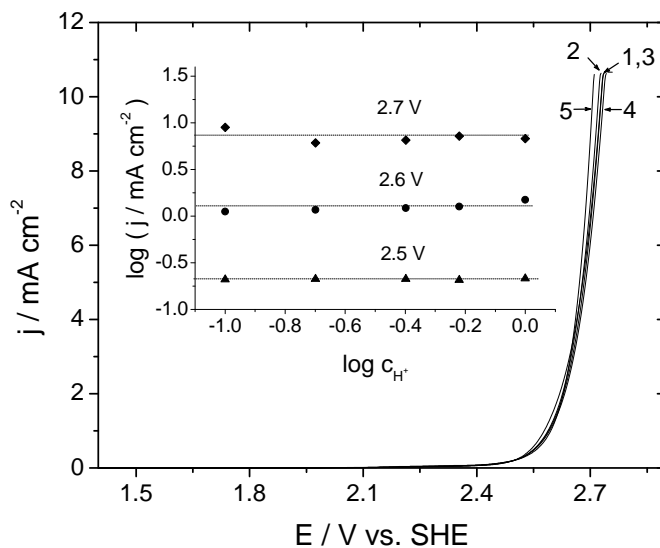


Figure 4.12. Current-potential curves of BDD MEA for various 1 M HClO_4 concentrations: (1) 1 M, (2) 0.6 M, (3) 0.4 M, (4) 0.2 M, (5) 0.1 M at constant ionic strength (1 M ClO_4^-); $T = 25^\circ\text{C}$. Inset shows dependence of log of current density on log of H^+ concentration for various potentials (2.5, 2.6, 2.7 V).

the curve in Fig. 4.11. The obtained value is equal to 0.44 and is close to the value of 0.5 assumed from the Tafel curve investigations in the same current density region (overpotential > 1.2 V).

4.3.4 Reaction order

Figure 4.12 shows current-potential curves recorded on BDD MEA for several HClO_4 concentrations (1–0.1 M). The ionic strength was adjusted to 1 M ClO_4^- by adding NaClO_4 to the solutions. It can be seen, that the current-potential curves do not vary remarkably with HClO_4 concentration. From the polarization curves the rate of oxygen evolution at constant potentials in the region of 2.5–2.7 V (overpotential > 1.2 V) was derived. The inset of Fig. 4.12 presents the log of the rate as a function of the log of H^+ concentration. As $\log j$ at constant potential does not vary with $\log c_{\text{H}^+}$ ($\partial \log j / \partial \log c_{\text{H}^+} = 0$) the order of the reaction with respect to H^+ is zero.

4.4 Discussion

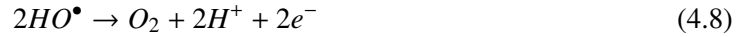
At BDD macroelectrode, the contribution of the ohmic drop to the measured potential leads to distortion of the anodic polarization curve resulting in a deviation of the Tafel plot from linearity (Fig. 4.3). Thus, in order to determine a Tafel slope, it is necessary to perform the correction for ohmic drop taking into account the total area-specific uncompensated resistance of the studied

system that includes not only the resistance of the electrolyte (which can increase in presence of gas bubbles) but also that of the electrode and the contacts in the outer circuit. Such an approach allowed to obtain, in the high overpotential region, a Tafel slope for OER equal to 123 mV dec^{-1} . Contrary to the Tafel slopes reported in literature (b -values between $150\text{--}500 \text{ mV dec}^{-1}$, sec. 4.1), a Tafel slope of 120 mV dec^{-1} is kinetically significant, and can be used to draw conclusions about the mechanism of the reaction.

Consider a simplified mechanism of oxygen evolution on BDD electrodes, in which the first step is the discharge of water leading to formation of quasi free hydroxyl radicals.



These hydroxyl radicals are further discharged to oxygen, probably via formation of hydrogen peroxide [60], according to the global reaction 4.8.



According to [76, 77], the Tafel slope of 120 mV dec^{-1} and zero reaction order with respect to H^+ suggest that the first step (Eq. 2.2) is the rate determining step.

We have shown in section 4.3.1 that the area-specific uncompensated resistance is almost 17 times higher on BDD macroelectrode than on BDD microelectrodes-array (MEA). Such a big difference between two electrodes can not result from the resistance of the anode material itself. Thus, the hypothesis of potential drop in the space-charge layer of diamond electrodes [17] is doubtful and rather the effect of the gas bubbles at the electrode surface should be considered [18]. The nucleation of bubbles requires sufficient oversaturation of the gas in the liquid. On microelectrodes, the enhanced mass transportation away from the electrode surface (due to the spherical diffusion) prevents from the local oversaturation of the gas in the liquid what makes the nucleation of bubbles more difficult. Taveres et al. [78] reported that nucleation of bubbles on microelectrodes is inhibited up to 2 A cm^{-2} . Therefore, the lack of bubbles on microelectrodes might be a key factor of relatively low R . As a consequence, the polarization curves on BDD MEA are not distorted and give directly (without ohmic drop correction) a Tafel slope of 120 mV dec^{-1} in the high overpotential region. In the low overpotential region ($< 1.2 \text{ V}$), the Tafel plot for OER has unusually high slope in case of both studied electrodes (340 and 680 mV dec^{-1} on BDD MEA and BDD, respectively). The high Tafel slope may result from the presence of surface re-

dox couples, as shown in Fig. 4.6, believed to be surface semi-hydroquinone / semi-benzoquinone functional groups [79]. Martin et al. [80] compared the voltammetric response of polycrystalline BDD macroelectrode with a single-crystal BDD. The authors observed the pre-OER redox couple only in case of polycrystalline BDD macroelectrode and associate it with grain-boundary reactivity of BDD. According to [80], this redox couple combines a reversible oxidation at the grain boundaries (by a change in oxygen functionality) and an irreversible oxidation (etching) process. In fact, the redox couples / functional groups can act as a barrier for OER leading to both high Tafel slope and high overpotential for oxygen evolution. The difference in Tafel slopes between BDD (680 mV dec^{-1}) and BDD MEA (340 mV dec^{-1}) may reflect the history of the electrode. As shown in [81, 79], the state of the electrode surface and the pre-treatment influence strongly the electrochemical response of diamond electrodes.

4.5 Conclusions

In order to perform an appropriate correction for the ohmic drop on BDD macroelectrodes it is necessary to estimate, in situ, the total resistance of the studied system. In fact, the resistance of the electrolyte itself is not sufficient for the correction of the polarization curves. Based only on the electrolyte resistance, misleading values of Tafel slopes may be obtained. On BDD microelectrodes-array (MEA), the correction of the polarization curve is not necessary due to the small contribution of ohmic drop to the measured potential. Thus, the analysis of the polarization curves can be performed directly.

In the high overpotential region ($> 1.2 \text{ V}$), the ohmic drop-corrected anodic polarization curve on BDD macroelectrode gave a Tafel slope of 120 mV dec^{-1} , which is the theoretical value considering a first electron transfer step as the rate determining step. Similar value was obtained (without ohmic drop correction) on BDD MEA. In the low overpotential region ($< 1.2 \text{ V}$), unusually high Tafel slope (340 and 680 mV dec^{-1} on BDD MEA and BDD, respectively) may result from the presence of surface redox couples / functional groups which can act as a barrier for oxygen evolution.

Chapter 5

Electrochemical Oxidation of C₁– Organic Compounds on BDD; Voltammetric and DEMS Study

In the presence of organic compounds in the electrolyte, oxygen evolution on BDD is considered to be a side reaction, being in competition with electrooxidation of organics. In this chapter, the electrochemical oxidation of simple C₁–organic compounds (methanol and formic acid) was studied on BDD using voltammetry and differential mass spectrometry (DEMS). DEMS was used to identify volatile products and intermediates of an oxidation, monitored on-line during the potential sweep. The analysis of experimental data showed that oxidation of organics proceeds at potential close to that of oxygen evolution reaction. With respect to the supporting electrolyte, a shift of the polarization curves to lower potential is observed in presence of organics, whereas the Tafel slopes remain close to 120 mV dec⁻¹. Considering a simplified mechanism of oxygen evolution reaction, presented in chapter 4, further discussion concerning mechanism of both oxygen evolution and C₁–organics electrooxidation is undertaken.

This chapter is based on the following publication:

A. Kapalka, G. Fóti and C. Comninellis. The importance of electrode material in environmental electrochemistry. Formation and reactivity of free hydroxyl radicals on boron-doped diamond electrodes, *Electrochim. Acta*, in press.

5.1 Introduction

A major uncertainty for the electrochemical oxidation of organic compounds on the BDD anode is whether the oxidation occurs via indirect or direct electron-transfer reaction. The indirect oxidation may proceed on the electrode surface by mediation of hydroxyl radicals formed during water discharge and other activated intermediates ($\text{H}_2\text{S}_2\text{O}_8$, O_3 , H_2O_2) [29, 60, 22]. In fact, on BDD, the electrochemical oxidation of most of the organic compounds (such as alcohols and carboxylic acids) occurs in the vicinity of oxygen evolution (> 2.3 V vs. SHE) [50]. That is why it is believed that hydroxyl radicals assist in the complete oxidation of organics. Nevertheless, some authors disagree with this opinion suggesting rather a direct electron-transfer reaction pathway [82, 83, 84]. They claim that oxidation of organics proceeds slightly before oxygen evolution region, thus without assistance of hydroxyl radicals.

Strong evidences for the direct oxidation were found at lower anodic potentials (< 2.3 V vs. SHE) in case of aromatic compounds [32, 85, 84]. The direct oxidation of aromatic compounds, however, results in electrode deactivation due to the formation of a polymeric film. In order to restore the electrode activity, it is necessary to apply high anodic potential (> 2.3 V vs. SHE) at which the polymeric film can be destroyed, probably via hydroxyl radical-mediated reactions. Therefore, as the evidences for both reaction pathways (indirect and direct) were reported, an oxidation mechanism of organics on BDD anode is still under discussion.

In this chapter, the electrochemical oxidation of simple C₁-organic compounds, such as methanol and formic acid, is investigated on BDD anode using voltammetry and differential mass spectrometry (DEMS). DEMS was used to identify products and intermediates of an oxidation, monitored on-line during the potential sweep. As a result, in parallel to faradaic current, the ionic current of $m/z = 44$ (CO_2), $m/z = 32$ (O_2), and $m/z = 31$ (CH_3OH) were recorded during oxidation of 1 mM methanol / formic acid in 1 M HClO_4 . The Tafel plot analysis was performed on BDD microelectrodes-array (MEA), on which the electrochemical response is not distorted by ohmic drop (as discussed in chapter 4). On the basis of obtained results, a discussion concerning indirect / direct oxidation is undertaken and a mechanism of C₁–organics electrooxidation is proposed.

5.2 Experimental details

Voltammetric measurements

Anodic polarization curves of methanol and formic acid were recorded in a single-compartment, three-electrode cell using an Autolab PGSTAT 30. The counter electrode was a Pt wire, the working electrode was BDD MEA (Fig. 4.1b–c), and the reference electrode was Hg/Hg₂SO₄/K₂SO₄ (sat) (MSE; 0.64 V vs. SHE). All voltammetric measurements were performed at room temperature, in 1 M HClO₄ as a supporting electrolyte.

The limiting current of methanol / formic acid oxidation was evaluated from Eq. 5.1 considering domination of spherical diffusion, without overlapping, at each microelectrode in the array of BDD MEA [67]

$$I_{lim} = n4zFDc_Rr \quad (5.1)$$

where z is the number of exchanged electrons (6 and 2 for methanol and formic acid, respectively), D (cm² s⁻¹) is the diffusion coefficient (1.9×10^{-5} and 1.7×10^{-5} [86] for methanol and formic acid [87], respectively), c_R (mol cm⁻³) is the organic concentration, r (cm) is the radius of a single microelectrode in the array, and n is the number of microelectrodes in the array (473).

Differential electrochemical mass spectrometry (DEMS)

DEMS measurements were performed on BDD macroelectrode in a dual thin layer electrochemical cell [36] under constant flow of 5 μ l s⁻¹ (see also chapter 2, sec. 2.2). This cell consist of two separate compartments: (i) the electrochemical compartment with the electrolyte inlet, and (ii) the mass spectrometric compartment with the electrolyte outlet (Fig. 5.1). The reaction products formed in the electrochemical compartment are transported through capillaries to the mass spectrometric compartment, where the volatile species can evaporate through the Teflon membrane to the quadrupole mass spectrometer (Pfeiffer Vacuum QMG 422). Thus, during DEMS measurements, the ionic current corresponding to a given species can be recorded in parallel to the faradaic current.

A reversible hydrogen electrode (RHE) was used as a reference electrode and two platinum wires as counter electrodes. The electrolyte volume and the geometric surface area (0.28 cm²) of the working electrode (BDD, B/C 6000 ppm) are defined by a thin (50–100 μ m) Teflon ring (spacer) placed on the disc shaped electrode. All measurements were performed at room temper-

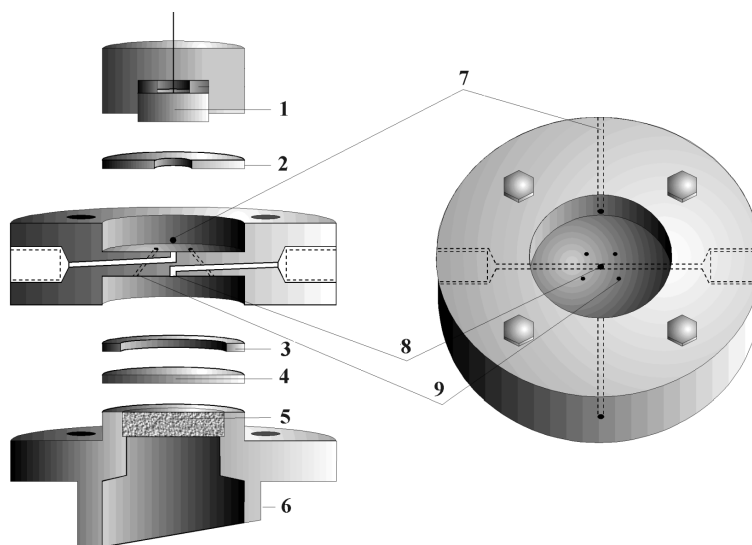


Figure 5.1. Side and top view of the dual thin layer cell (1) BDD electrode, (2–3) Teflon spacer, (4) porous Teflon membrane, (5) stainless steel frit, (6) connection to the vacuum system and the mass spectrometer, (7) capillaries for flushing with gas, (8) inlet-outlet capillaries, (9) connecting capillaries [36].

ature, in 1 M HClO₄ as a supporting electrolyte. Both faradaic and ionic current were measured as a function of potential to obtain the cyclic voltammograms (CV) and the mass spectrometric cyclic voltammograms (MSCV), respectively. The solutions were deaerated with argon during measurements.

Calibration of DEMS for CO₂ and O₂

To calibrate the mass spectrometer for CO₂, the oxidation of adsorbed CO on polycrystalline Pt-electrode was performed, according to [88]. After activation of the electrode by scanning the potential between 0.05 and 1.6 V vs. RHE in 1 M HClO₄, the potential was stopped at the adsorption potential (0.05 V) and the electrolyte in the cell was substituted for saturated CO in 1 M HClO₄. When adsorption of CO on the electrode surface was finished, the solution was replaced with a pure electrolyte and the anodic scan was continued in order to oxidize adsorbed CO. During the whole experiment, the faradaic current and the ionic current of CO₂ were registered simultaneously, as shown in Fig. 5.2.

The integrated faradaic oxidation current and ionic current for CO₂ were used to determine the calibration constant $K^*(44)$ for CO₂ collection, according to Eq. 5.2 [36]

$$K^*(44) = \frac{2Q_i}{0.8Q_f} \quad (5.2)$$

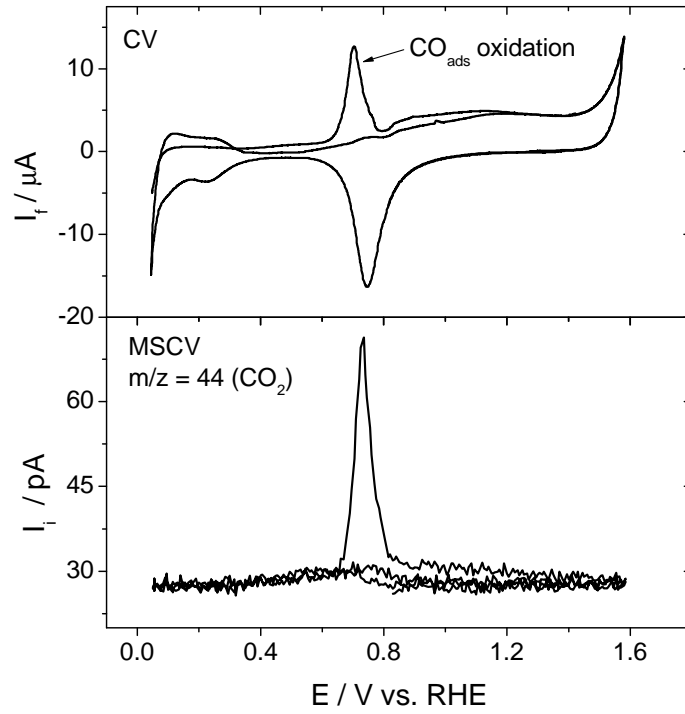
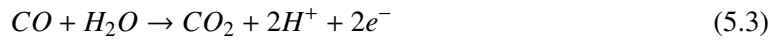


Figure 5.2. Simultaneously recorded cyclic voltammogram (CV) and mass spectrometric CV (MSCV) for CO_2 ($m/z = 44$) during oxidation of adsorbed CO on polycrystalline Pt-electrode; electrolyte 1 M HClO_4 ; scan rate 10 mV s^{-1} , flow rate $5 \mu\text{l s}^{-1}$.

where Q_i and Q_f is the ionic and faradaic charge corresponding to CO_2 formation, 2 is the number of electrons for CO oxidation to CO_2 (Eq. 5.3), and 0.8 is the correction factor for double layer charging effect in the presence of CO on the electrode surface. The calibration constant, $K^*(44)$, was found to be 9.4×10^{-6} .



To calibrate the mass spectrometer for O_2 , the ionic current $I_i(32)$ of O_2 and the faradaic current I_f was measured simultaneously on a polycrystalline Pt-electrode, in 1 M HClO_4 , at 1.7 V vs. RHE for 20 seconds. The calibration constant $K^*(32)$ was calculated according to Eq. 5.4, and was found to be 6.05×10^{-6}

$$K^*(32) = \frac{4I_i(32)}{I_f} \quad (5.4)$$

where 4 is the number of electrons for O_2 formation according to Eq. 5.5.



The current efficiency for CO₂ and O₂ formation

The current efficiency *CE* of CO₂ formation was determined from the faradaic current I_f and ionic current $I_i(44)$ of CO₂, according to Eqs. 5.6–5.7 [89]

$$I_f^*(CO_2) = \frac{zI_i(44)}{K^*(44)} \quad (5.6)$$

$$CE(CO_2) = \frac{I_f^*(CO_2)}{I_f} \quad (5.7)$$

where $I_f^*(CO_2)$ is the faradaic current corresponding to the formation of CO₂, z is the number of electrons for organics oxidation to CO₂ and $K^*(44)$ is the calibration constant.

By analogy to Eqs. 5.6–5.7, the current efficiency of O₂ was calculated as given by Eqs. 5.8–5.9.

$$I_f^*(O_2) = \frac{zI_i(32)}{K^*(32)} \quad (5.8)$$

$$CE(O_2) = \frac{I_f^*(O_2)}{I_f} \quad (5.9)$$

For all measurements, the current efficiency was evaluated in the potential region of 2.50–2.85 V vs. RHE, in which the potential was held for 20 s at every 50 mV in order to read the faradaic and ionic current.

5.3 Results

5.3.1 Voltammetric study of methanol and formic acid oxidation

Figure 5.3 shows the current-potential curves (I – V) recorded on BDD microelectrodes-array (MEA) in presence of methanol and formic acid, respectively. The measurements were performed below the limiting current evaluated from Eq. 5.1. In the potential region of water stability, no significant change in electrochemical response with respect to the supporting electrolyte is observed (Fig. 5.3). On the contrary, in the region of water decomposition, the current density increases for a given potential with increase of organic concentration. The corresponding Tafel plots for different concentrations of methanol and formic acid are shown in insets of 5.3a and 5.3b, respectively. For both methanol and formic acid, the Tafel coefficients are in the region of 90–130 mV dec^{–1}.

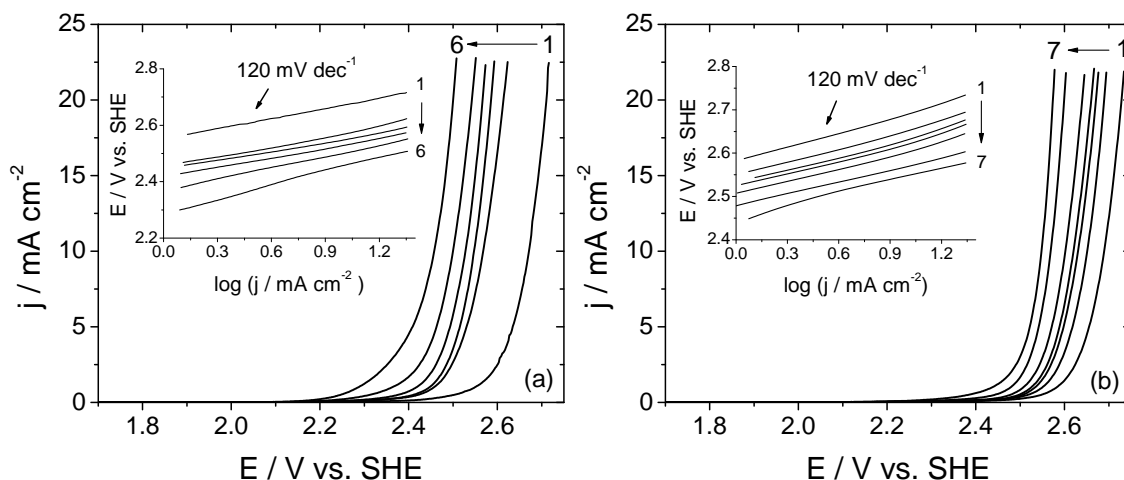


Figure 5.3. Current-potential curves recorded on BDD MEA at 2 mV dec^{-1} in presence of (a) methanol: (1) blank, (2) 1.25 mM, (3) 2.5 mM, (4) 3.75 mM, (5) 5 mM, (6) 50 mM; (b) formic acid: (1) blank, (2) 1.25 mM, (3) 2.5 mM, (4) 3.75 mM, (5) 5.0 mM, (6) 10 mM, (7) 100 mM; electrolyte 1 M HClO_4 ; $T = 25^\circ\text{C}$. Insets show the corresponding Tafel plots.

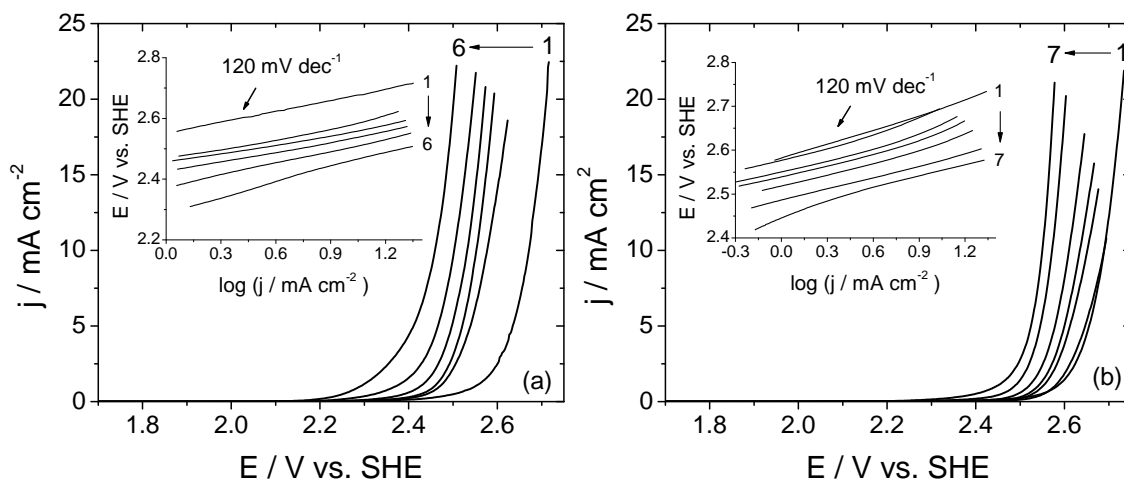


Figure 5.4. Current-potential curves, as in Fig 5.3, after background subtraction for the reaction of O_2 evolution (curve 1). Insets show the corresponding Tafel plots.

Figure 5.4 shows the I - V curves and the corresponding Tafel plots of methanol and formic acid obtained after subtraction of the background current for the reaction of O_2 evolution (curve 1). It can be seen that the elimination of the background current does not influence the Tafel slopes, which remain in the region of 90 – 130 mV dec^{-1} . On the contrary, the background current subtraction makes the shift of the current-potential curves toward lower potentials less important. Figure 5.5a and b show the shift of potential, ΔE , as a function of methanol and formic acid concentration, respectively, at 5 mA cm^{-2} . For each organics concentration, ΔE was calculated with respect to the supporting electrolyte (curve 1). It can be seen that ΔE is more important in case of methanol

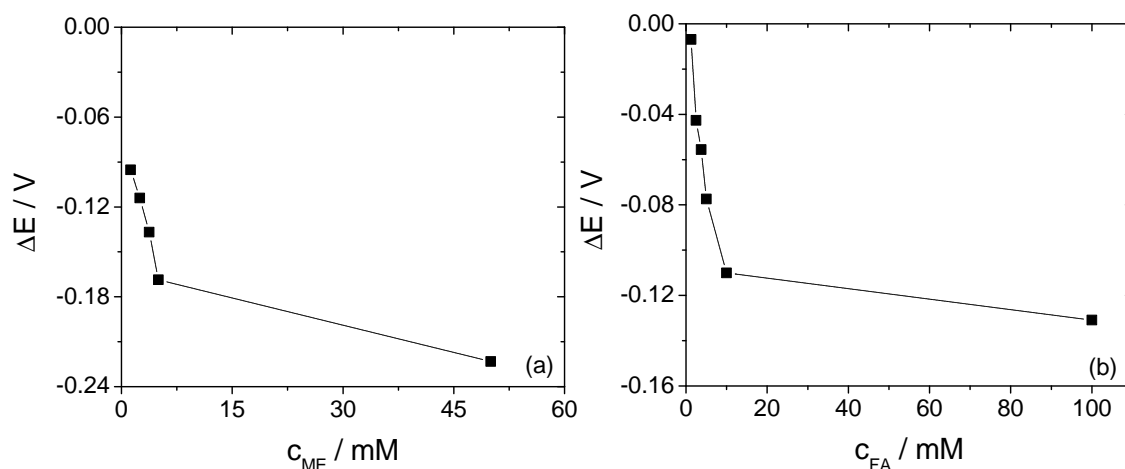


Figure 5.5. Shift of potential ΔE calculated from Fig. 5.4 at 5 mA cm^{-2} , with respect to the supporting electrolyte, for (a) methanol, and (b) formic acid.

than formic acid. Moreover, for both organic compounds ΔE at first changes very fast with the concentration, and then tends to stabilize.

5.3.2 DEMS study of methanol and formic acid oxidation

5.3.2.1 Response of the supporting electrolyte

Figure 5.6 shows the cyclic voltammogram (CV) and the mass spectrometric cyclic voltammogram (MSCV) for $m/z = 32$ (O_2) and $m/z = 44$ (CO_2) simultaneously recorded on BDD in 1 M HClO_4 . It can be seen that during anodic scan of potential, in parallel to oxygen evolution (5.6b), some traces of CO_2 were detected. Using Eq. 5.7, the current efficiency of CO_2 formation at 2.85 V vs. RHE (at the highest investigated potential) was found to be $\sim 0.3 \%$.

Figure 5.7 shows the current efficiency for O_2 formation ($CE(\text{O}_2)$) as a function of potential. It can be seen that in investigated potential region, $CE(\text{O}_2)$ reaches (within an experimental error) 100% .

5.3.2.2 Methanol oxidation

Figure 5.8 shows the CV and the MSCV for $m/z = 31$ (CH_3OH), $m/z = 32$ (O_2) and $m/z = 44$ (CO_2) simultaneously recorded on BDD during oxidation of $1 \text{ mM CH}_3\text{OH}$ in 1 M HClO_4 . Figure 5.8a shows that faradaic current I_f starts to increase at $\sim 2.3 \text{ V}$ vs. RHE simultaneously to the decrease of the ionic current for methanol $I_i(31)$ (5.8b). $I_i(31)$ reaches a limitation at higher potentials which can be attributed, as a first approximation, to the mass transfer limitation. As a consequence,

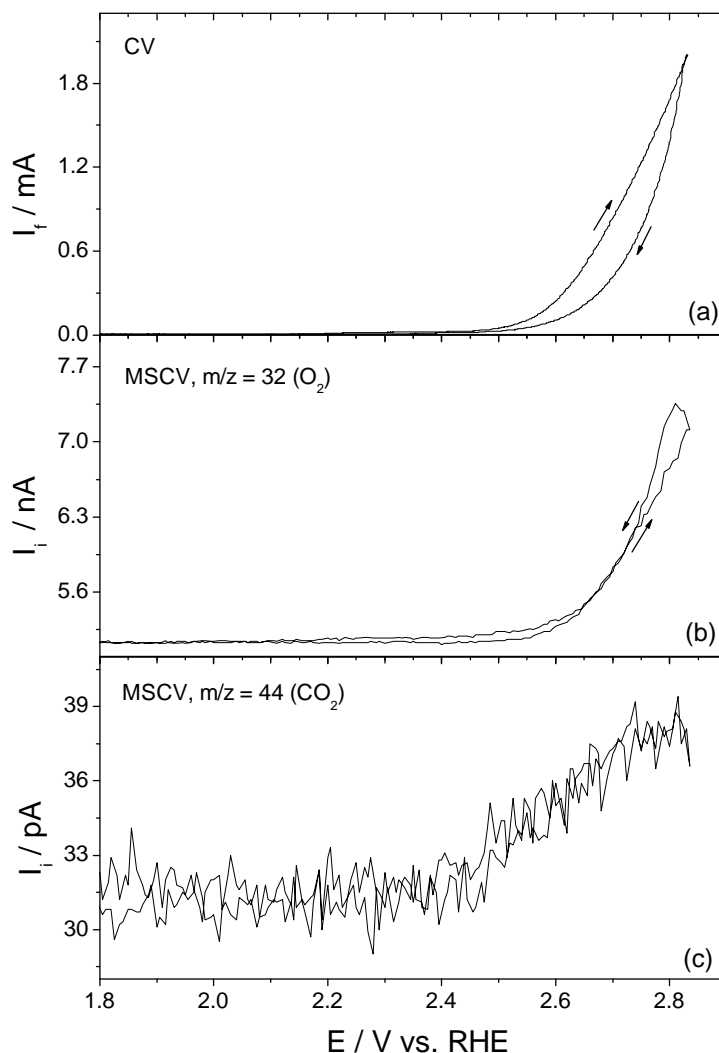


Figure 5.6. Simultaneously recorded (a) cyclic voltammogram (CV) and mass spectrometric CV (MSCV) for (b) O_2 ($m/z = 32$), (c) CO_2 ($m/z = 44$) on BDD in 1 M HClO_4 ; scan rate 10 mV s^{-1} , flow rate $5 \mu\text{l s}^{-1}$; $T = 25^\circ\text{C}$.

the effect of $I_i(31)$ limitation on I_f can be observed in the form of an oxidation wave in the vicinity of oxygen evolution (Fig. 5.8a). Figure 5.8c shows that oxygen evolution starts to proceed from $\sim 2.6 \text{ V vs. RHE}$, i.e., once the $I_i(31)$ limitation is attained.

The ionic current for CO_2 , $I_i(44)$, increases from $\sim 2.5 \text{ V vs. RHE}$ reaching a limitation in parallel to $I_i(31)$. The difference between the onset potential of CH_3OH oxidation and CO_2 formation is about 0.2 V , what may indicate the formation of intermediates. Indeed, methylformate was found as an intermediate of methanol oxidation. Figure 5.9 shows the MSCV of methylformate ($m/z = 60$) recorded during oxidation of 1, 5 and 10 mM CH_3OH . It can be seen that methylformate starts to be formed at $\sim 2.25 \text{ V vs. RHE}$ and reaches a limitation at $\sim 2.5 \text{ V}$. This indicates that, above $\sim 2.5 \text{ V}$, oxidation of methylformate dominates its formation, leading to the

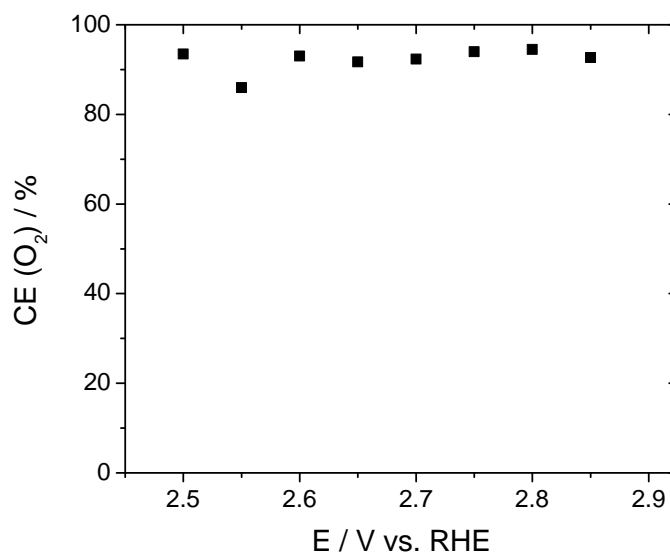


Figure 5.7. Current efficiency for O₂ evolution as a function of potential in 1 M HClO₄ on BDD. Experimental conditions as in Fig. 5.6.

peak-shaped response. This potential corresponds well to the onset potential of CO₂ formation.

Figure 5.10 shows the corresponding to Fig. 5.8 current efficiency for CO₂ and O₂ formation as a function of potential in the range of 2.50–2.80 V vs. RHE. $CE(\text{CO}_2)$ at first increases, and then passes through the maximum at 2.65 V. From this potential, $CE(\text{O}_2)$ continuously increases. By adding $CE(\text{CO}_2)$ to $CE(\text{O}_2)$ and subtracting from 100%, the efficiency for intermediates formation was evaluated. It can be seen that the formation of intermediates is important in the potential region below CO₂ limitation (< 2.65 V), i.e., in the charge-transfer control region, as it has been reported previously in [32] (see also chapter 2, sec. 2.1.3).

5.3.2.3 Formic acid oxidation

Figure 5.11 shows the CV and the MSCV for $m/z = 44$ (CO₂) and $m/z = 32$ (O₂) simultaneously recorded on BDD during oxidation of 1 mM HCOOH in 1 M HClO₄. Formic acid starts to be oxidized from ~2.4 V vs. RHE, resulting in increase of both the faradaic current I_f and the ionic current, $I_i(44)$, for CO₂. During its oxidation, no intermediates were found. Similar to methanol, $I_i(44)$ of formic acid reaches a limitation (probably, mass transfer limitation) at higher potentials. The oxygen evolution, a secondary reaction, starts to proceed from ~2.6 V.

Figure 5.12 shows the corresponding to Fig. 5.11 current efficiency for CO₂ and O₂ formation as a function of potential in the range of 2.50–2.85 V vs. RHE. It seems that the maximum of $CE(\text{CO}_2)$ appears at the potential below 2.5 V. Thus, in the investigated potential region, $CE(\text{CO}_2)$

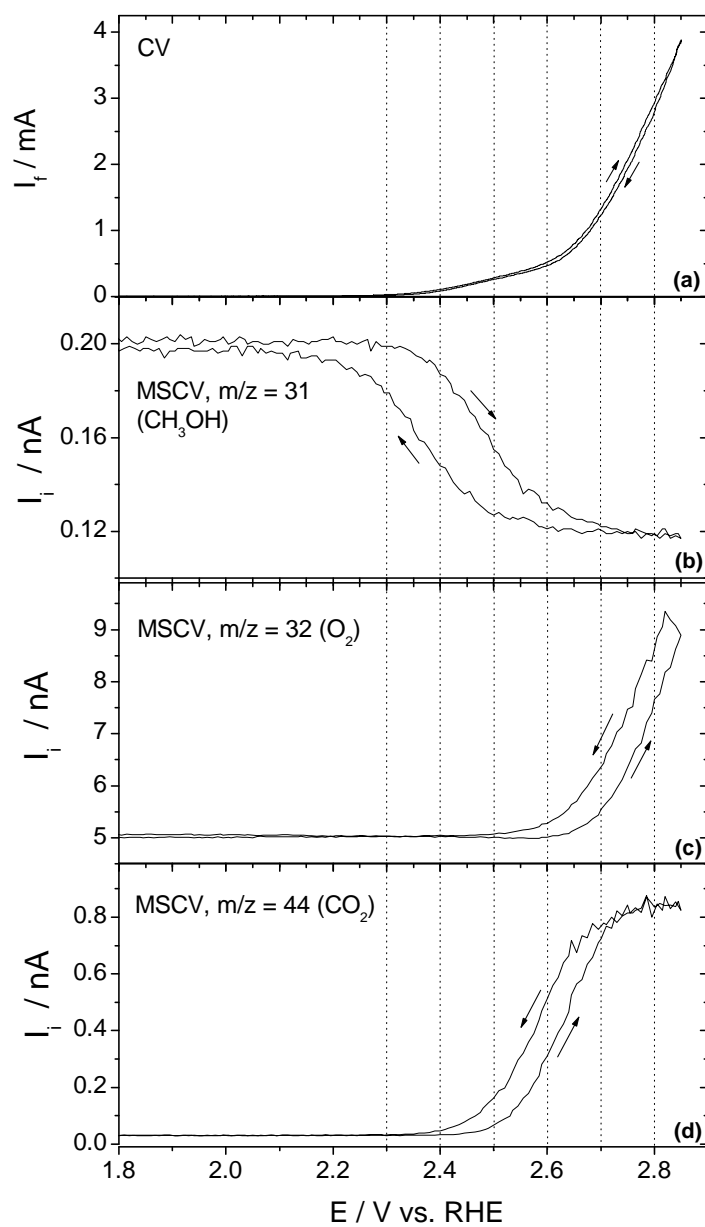


Figure 5.8. Simultaneously recorded CV (a) and MSCV for (b) $m/z = 31$ (CH_3OH), (c) $m/z = 32$ (O_2) and (d) $m/z = 44$ (CO_2) on BDD in 1 mM CH_3OH ; scan rate 10 mV s^{-1} , flow rate $5 \mu\text{l s}^{-1}$, electrolyte 1 M HClO_4 ; $T = 25^\circ\text{C}$.

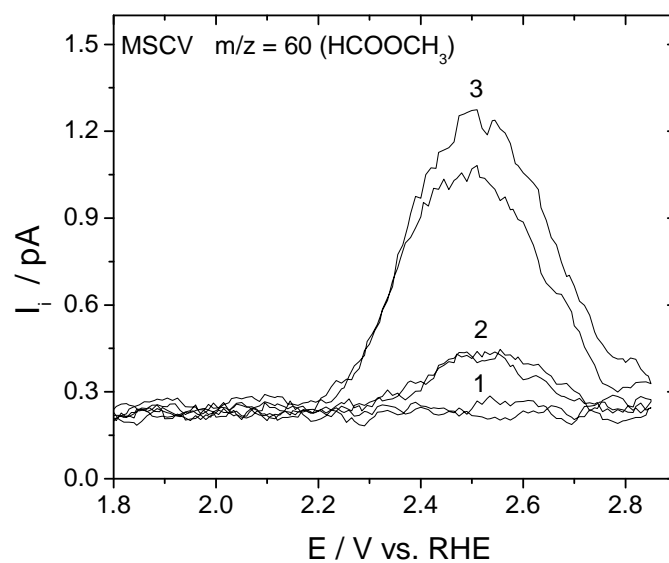


Figure 5.9. MSCV of $m/z = 60$ (HCOOCH_3) recorded on BDD in (1) 1 mM, (2) 5 mM and (3) 10 mM CH_3OH ; Experimental conditions as in Fig. 5.8.

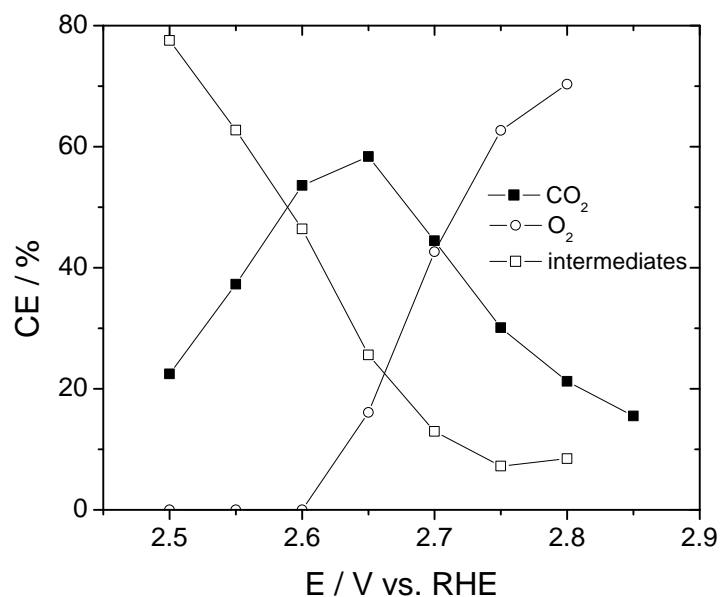


Figure 5.10. The current efficiency CE for CO_2 , O_2 , and intermediates formation during oxidation of 1 mM CH_3OH on BDD. Experimental conditions as in Fig. 5.8

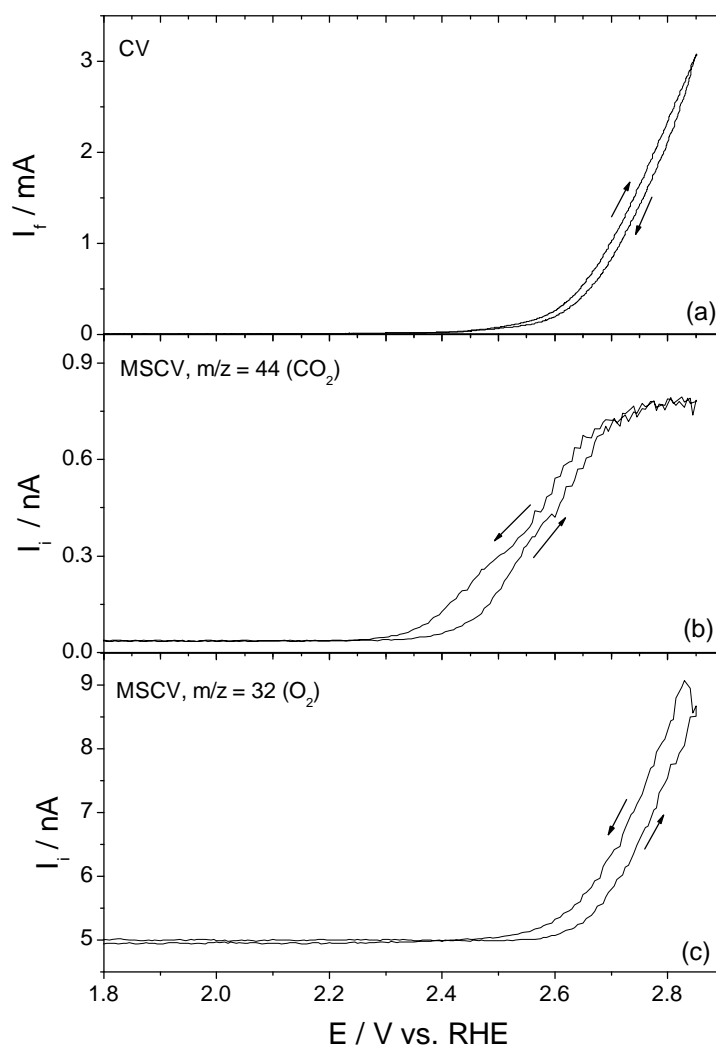


Figure 5.11. Simultaneously recorded CV (a) and MSCV for (b) $m/z = 44$ (CO_2) and (c) $m/z = 32$ (O_2) on BDD in 1 mM HCOOH ; scan rate 10 mV s^{-1} , flow rate $5 \mu\text{l s}^{-1}$, electrolyte 1 M HClO_4 ; $T = 25^\circ\text{C}$.

continuously decreases, whereas CE (O_2) increases up to 80 %.

5.4 Discussion

Voltammetric measurements

Considering a simplified mechanism of oxygen evolution on BDD anode, presented in chapter 4 (Eqs. 2.2, 4.8), the indirect oxidation of C_1 –organic compounds R mediated by quasi free hydroxyl radicals on BDD surface can be expressed as:



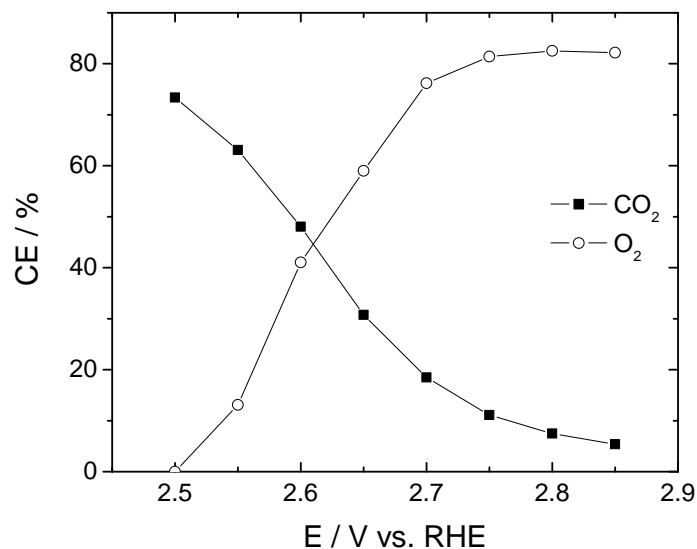


Figure 5.12. The current efficiency CE for CO_2 and O_2 formation during oxidation of 1 mM HCOOH on BDD. Experimental conditions as in Fig. 5.11.

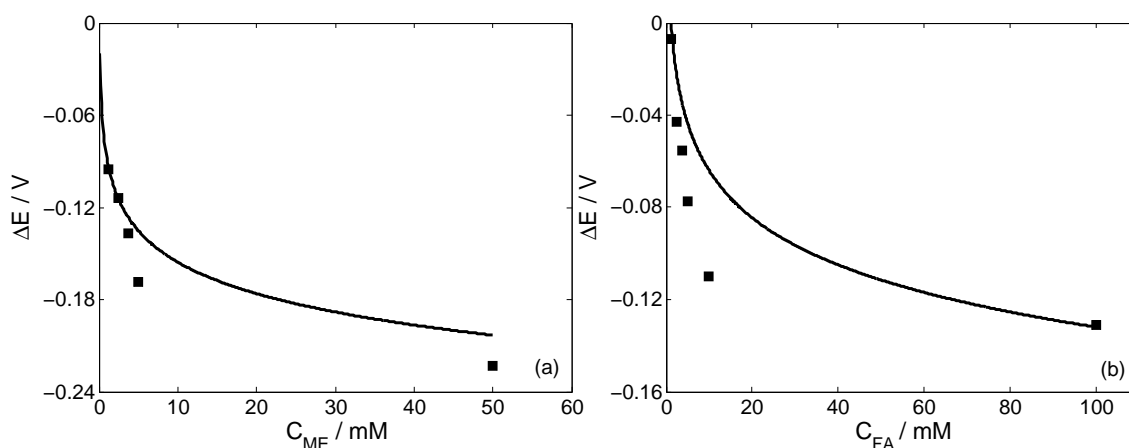


Figure 5.13. Comparison of the potential shift (ΔE) obtained experimentally (■) for methanol (a) and formic acid (b) (Fig. 5.5) with ΔE evaluated from Eqs. 3.14, 3.21, and 3.25 (—); current density 5 mA cm²; $D_{\text{HO}^\bullet} = 2.2 \times 10^{-9} \text{ m}^2 \text{ s}^{-1}$, $k_{\text{HO}^\bullet} = 5.5 \times 10^6 \text{ m}^3 \text{ mol}^{-1} \text{ s}^{-1}$, $k_{\text{HCOOH}} = 1.3 \times 10^5 \text{ m}^3 \text{ mol}^{-1} \text{ s}^{-1}$, $k_{\text{CH}_3\text{OH}} = 9.7 \times 10^5 \text{ m}^3 \text{ mol}^{-1} \text{ s}^{-1}$ [61]; $z = 2$, and 6 for formic acid and methanol, respectively.



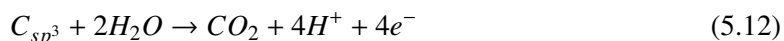
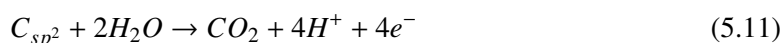
In the supporting electrolyte, the Tafel slope of 120 mV dec⁻¹ indicates that the water discharge (Eq. 2.2) is a rate determining step of OER (as discussed in chapter 4). It is interesting to note that

when methanol or formic acid is added, the Tafel slope remains 120 mV dec^{-1} (inset of Fig. 5.3), and so the rate determining step does not change. This indicates that oxidation of both methanol and formic acid is a fast reaction.

Electrooxidation of both organic compounds affects the current-potential curves, causing its shift toward lower potentials with respect to the potential of electrolyte decomposition (Fig. 5.3–5.5). As discussed in chapter 3, such a shift (ΔE) may result from a difference in the rate of HO^\bullet disappearance during oxygen evolution in the supporting electrolyte and oxidation of organic compounds. In fact, using Eqs. 3.14, 3.21 and 3.25 in chapter 3, ΔE can be evaluated. Figure 5.13 shows the comparison of ΔE obtained experimentally (Fig. 5.5) and evaluated from Eq. 3.25. It can be seen that for both methanol and formic acid there is a satisfactory agreement between predicted values and experimental data.

DEMS measurements

Figure 5.6 shows that in 1 M HClO_4 , oxygen evolution reaction starts to proceed remarkably from 2.5 V vs. RHE resulting in simultaneous increase of both the faradaic current and the ionic current for O_2 . The current efficiency for O_2 evolution reaches 100% indicating that O_2 , as expected, is a main product formed in this potential region (2.50–2.85 V vs. RHE). As these measurements were performed in perchloric acid, detected in parallel CO_2 results certainly from the corrosion of the electrode. According to [79], two reactions may occur during anodic scan:



Reaction 5.11, however, is more probable because sp^2 are more electrochemically active than sp^3 . Relatively high current efficiency for CO_2 formation (0.3%) can be explained by a high sp^2 removal from fresh BDD electrode which was used. In fact, after several measurements, $CE(\text{CO}_2)$ dropped down to $\sim 0.13\%$.

Addition of 1 mM methanol / formic acid (Fig. 5.8 and 5.11, respectively) results in an increase of the faradaic current with respect to the base electrolyte. The oxidation of organics starts at $\sim 2.3 \text{ V vs. RHE}$ and $\sim 2.4 \text{ V vs. RHE}$ for methanol and formic acid, respectively, i.e., in the vicinity of oxygen evolution reaction. The oxidation of organics continuously proceeds with increasing

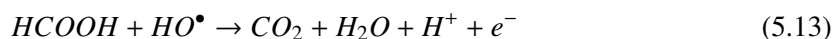
potential, reaching a limitation (probably, a mass transfer limitation) at higher potentials. In this potential region, the oxygen evolution and oxidation of intermediates (methylformate in case of methanol, Fig. 5.9) starts to proceed. Considering indirect oxidation of organics, in the mass transfer control region, the oxidation of methylformate and oxygen evolution may result from a high local concentration (relative to methanol) of hydroxyl radicals [32].

It is interesting to note that oxygen evolution reaction shifts towards higher potentials for about 100 mV and 50 mV in presence of methanol and formic acid, respectively. This confirms that oxygen evolution is a side reaction proceeding once the limiting current for organics oxidation is attained (Fig. 5.10 and 5.12). These experimental results are in agreement with the previous work performed in our group [50].

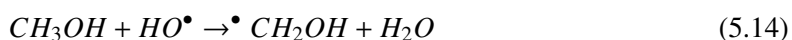
As mentioned in the introduction, some authors claim that electrooxidation of organics proceeds at a potential below that for water discharge, thus without assistance of hydroxyl radicals [83]. Their main argument is the fact that during oxidation of organics an oxidation wave appears before oxygen evolution. According to our results, electrooxidation of organics starts in the very close vicinity of O₂ evolution resulting in the shift of the latter towards higher potentials. As shown in chapter 4 sec. 4.3.1.2, in this potential region (overpotential with respect to OER >1.1 V), in the supporting electrolyte, the discharge of water already proceeds (because the current increases), although the oxygen evolution is not much pronounced. Thus, in this potential region, the assistance of hydroxyl radicals in electrooxidation of organics should not be excluded.

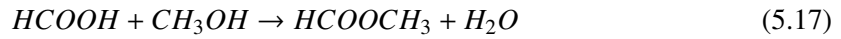
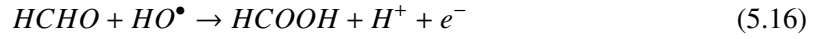
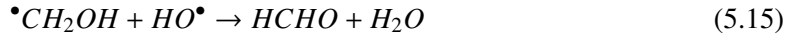
Mechanism of formic acid and methanol electrooxidation

Considering indirect oxidation of formic acid, the following reaction can be proposed:



In case of methanol, a more complex mechanism is expected. Taking into account that oxidation of methanol proceeds via formation of methylformate (Fig. 5.9), it can be thought that formic acid is also produced, although it was not detected by DEMS due to its low volatility. Thus, considering indirect mechanism, possible main reactions can be expressed as:





5.5 Conclusions

On the basis of obtained results, the indirect mechanism of electrooxidation of methanol and formic acid, mediated by quasi free hydroxyl radicals, is assumed. It has been shown that oxidation of both methanol and formic acid is a fast reaction, whereas the rate determining step is the water discharge to hydroxyl radicals. In presence of organics, oxygen evolution is a secondary reaction and proceeds once the limiting current for organics oxidation is attained. As a consequence, oxygen evolution shifts toward higher potentials.

The electrochemical oxidation of both methanol and formic acid results in a shift of the current-potential curves toward lower potentials with respect to decomposition of the supporting electrolyte (oxygen evolution). This phenomenon can be explained by a change in an onset potential of $\text{HO}\bullet$ formation in the presence and absence of organic compounds, as discussed in chapter 3. In fact, using Nernst equation, a satisfactory agreement between the experimental results and proposed model (chapter 3) has been obtained.

Chapter 6

Electrochemical Oxidation of Formic Acid on BDD with 100% current efficiency

In this chapter the electrochemical oxidation of formic acid is investigated on BDD anode in a batch recirculation reactor operating in a galvanostatic mode. The experimental conditions were varied, by changing the applied current, in order to study the oxidation process under: 1) current limitation, 2) mixed current-mass transport control, and 3) mass transport control. The experimental results were compared with the theoretical model developed by Michaud [22]. In order to achieve 100% current efficiency throughout oxidation process, electrolysis was carried out under programmed current, in which the current density was adjusted to the limiting value. The very good fit between experimental results and theoretical model confirmed that oxidation of formic acid at boron-doped diamond electrode is a fast reaction, controlled by the mass transport to the anode surface.

This chapter is based on the following publications:

A. Kapałka, G. Fóti and C. Comninellis. Investigations of electrochemical oxygen transfer reaction on boron-doped diamond electrodes, *Electrochim. Acta*, 53 (2007) 1954.

A. Kapałka, G. Fóti and C. Comninellis. Kinetic Modelling of the Electrochemical Mineralization of Organic Pollutants for Wastewater Treatment, *J. Appl. Electrochem.*, 38 (2008) 7.

6.1 Introduction

As reported in the previous chapter, electrogenerated hydroxyl radicals are involved in both the main reaction of organics oxidation (Eq. 2.4) and the side reaction of oxygen evolution (Eq. 2.5).



For this simplified reaction scheme, a theoretical kinetic model has been developed by Michaud [22] to predict the evolution of the chemical oxygen demand and the current efficiency of the electrochemical oxidation of organic compounds on boron-doped diamond anodes (see also chapter 2, sec. 2.1.3). This model was formulated for a batch recirculation system operating under galvanostatic conditions. The following supposition has been made:

- oxidation of organics in bulk by oxidants like H_2O_2 or O_3 is not considered,
- adsorption of the organic compounds at the electrode surface is negligible,
- diffusion coefficient does not depend on the nature of organics,
- the electrochemical mineralization of organics is a fast reaction and it is controlled by the mass transport of organics to the anode surface.

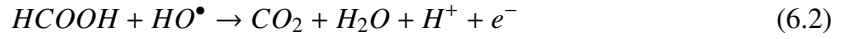
The consequence of the last assumption is that the rate of the mineralization reaction is independent of the chemical nature of the organic compound present in the electrolyte. Thus, in principle, this theoretical kinetic model is valid for any organic compound oxidized on BDD anode, as confirmed by preparative electrolysis of different classes of compounds [50]. In this chapter, the principles of this model will be presented on formic acid as an example.

Theoretical model for formic acid electrooxidation on BDD anodes

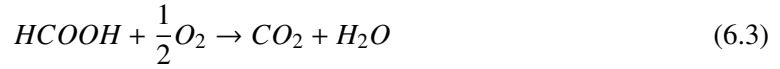
Assuming that the anodic oxidation of organics is under diffusion control, the limiting current density for the electrochemical oxidation of formic acid can be written as:

$$j_{lim} = 2Fk_m c_R \quad (6.1)$$

where j_{lim} ($A\ m^{-2}$) is the limiting current density for formic acid electrooxidation, F ($C\ mol^{-1}$) is the Faraday constant, k_m ($m\ s^{-1}$) is the mass transport coefficient, c_R ($mol\ m^{-3}$) is the concentration of formic acid, and 2 is the total number of electrons involved in formic acid electrooxidation according to Eq. 6.2,



From the equation of the chemical mineralization of formic acid to CO_2 and H_2O (Eq. 6.3), it is possible to obtain the relation between the formic acid concentration and the chemical oxygen demand COD ($mol\ O_2\ m^{-3}$), which represents the amount of oxygen required to oxidize formic acid (Eq. 6.4).



$$c_R = 2COD \quad (6.4)$$

From Eqs. 6.1 and 6.4 and at a given time t during electrolysis, one can relate the limiting current density of the electrochemical mineralization of formic acid with the chemical oxygen demand.

$$j_{lim}(t) = 4Fk_m COD(t) \quad (2.6)$$

Depending on applied current density relative to the limiting value, two different operating regimes can be identified:

- $j_{apply} < j_{lim}$: the electrolysis is under current control, organic intermediates are formed during the oxidation, the instantaneous current efficiency (ICE) is 100% and COD decreases linearly with time. This behavior persists until a critical time (t_{cr}) at which the applied current density is equal to the limiting current density

Table 6.1. Equations describing *COD* and *ICE* as a function of time during oxidation of organics at BDD anodes; $COD^o = COD(t = 0)$; V_r is the reservoir volume, k_m is the mass transport coefficient, A is the electrode surface area, and $\alpha = j_{apply}/j_{lim}$.

	Instantaneous current efficiency <i>ICE</i>	Chemical oxygen demand <i>COD</i>
$j_{apply} < j_{lim}$; current control	1	$COD^o \left(1 - \frac{\alpha A k_m}{V_r} t\right)$
$j_{apply} > j_{lim}$; mass-transport control	$\exp\left(-\frac{A k_m}{V_r} t + \frac{1-\alpha}{\alpha}\right)$	$\alpha COD^o \exp\left(-\frac{A k_m}{V_r} t + \frac{1-\alpha}{\alpha}\right)$

- $j_{apply} > j_{lim}$: the electrolysis is under mass transport control, organic compounds are mineralized to CO_2 and secondary reactions (such as oxygen evolution or electrolyte decomposition) commence, resulting in a decrease of current efficiency. Under these conditions, the instantaneous current efficiency is below 100% and the *COD* removal follows an exponential trend.

Table 6.1 summaries the equations of the theoretical model for both current control and mass transport control regimes, developed by Michaud [22].

6.2 Optimization of the electrochemical mineralization on BDD anodes

In order to work at 100% of current efficiency throughout the oxidation process, electrolysis has to be carried out under programmed current, in which applied current density during electrolysis is continuously adjusted to the limiting value [22]. To do so, it is necessary to estimate the initial current density j_{lim}^o for the electrochemical mineralization using following equation:

$$j_{lim}^o = 4Fk_m COD^o \quad (2.7)$$

where COD^o is the initial chemical oxygen demand.

Then, using equation for *COD* evolution under mass transfer control (Table 6.1) and considering $\alpha = 1$ (applied current density equals to calculated initial limiting current density given in Eq. 2.7) one obtains:

$$COD = COD^o \exp\left(-\frac{A k_m}{V_r} t\right) \quad (6.5)$$

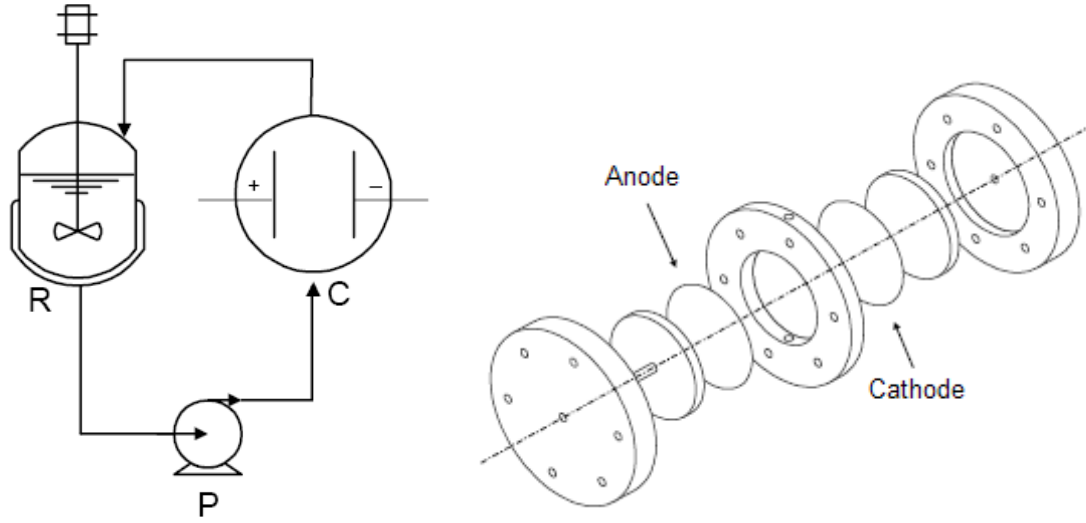


Figure 6.1. Scheme of the one-compartment electrochemical flow cell used for bulk oxidation of formic acid on BDD anode; *R* is the reservoir, *P* is the pump, *C* is the electrochemical cell, shown in more details on the right.

Inserting Eq. 6.5 to 2.6, the theoretical temporal evolution of the limiting current during electrolysis is given as:

$$j_{lim} = j_{lim}^o \exp\left(-\frac{Ak_m}{V_r} t\right) \quad (6.6)$$

Therefore, in order to work at 100% of current efficiency, it is necessary to start electrolysis by application of a current density corresponding to the initial limiting value j_{lim}^o . During electrolysis the applied current density has to be continuously adjusted to the time dependent limiting value according to Eq. 6.6.

From Eq. 2.7 and 6.6 it is also possible to estimate the electrolysis time τ in order to achieve the target final *COD* value, COD_{final} , using the relation:

$$\tau = -\frac{V_r}{Ak_m} \ln \frac{COD_{final}}{COD^o} \quad (6.7)$$

In order to validate experimentally this kinetic model, in the experimental part of this chapter, the preparative electrolysis of formic acid on BDD anode is presented under conditions of current control, mass-transfer control, mixed current-mass transfer control and under programmed current.

6.3 Experimental details

Bulk electrolysis

Electrolysis of formic acid in 1 M HClO₄ was performed in a one compartment electrolytic flow cell (Fig. 6.1) operating in a galvanostatic mode. The anode and the cathode were discs of boron-doped diamond (B/C 1000 ppm) and zirconium, respectively, with a geometric area of 50 cm². Both electrodes were attached, with a silver paste (EPO-TEK, 410E, Polyscience AG), to the aluminium support. The electrolyte was stored in a 0.5 dm³ thermoregulated glass tank and circulated through the electrolytic cell by means of a centrifugal pump. The flow rate of the electrolyte in the cell was 200 dm³ h⁻¹.

Determination of the mass transfer coefficient

The mass transfer coefficient k_m was determined using equimolar ferri/ferrocyanide redox couple (20–80 mM) in 1 M NaOH, as described in [22]. The measurement was carried out on nickel anode and cathode. Considering the symmetry of the electrochemical cell and supposing that the diffusion coefficients are the same for reduced and oxidized species, the k_m was determined from the following equation:

$$k_m = \frac{j_{lim}}{zFc} \quad (6.8)$$

where j_{lim} (A m⁻²) is the limiting current density, z is the number of electrons ($z = 1$), F (C mol⁻¹) is the Faraday constant, and c (mol m⁻³) is the concentration of [Fe(CN)₆⁴⁻]. The limiting current was measured by linear sweep voltammetry. Obtained value of k_m was equal to 2×10^{-5} m s⁻¹.

Instantaneous current efficiency

The current efficiency for the anodic oxidation of formic acid during electrolysis was obtained through the measurements of the chemical oxygen demand (COD) using an HACH DR/2010 analyser. COD represents the amount of oxygen needed to oxidize the organic matter in the solution. The oxidation took place in a vial containing silver catalyst and mercuric sulfate. 2 ml of formic acid solution was added to this vial and the mixture reacted for 2 hours at 150°C. After cooling, COD was measured using a spectrophotometer DR/2010, calibrated with a potassium hydrogen phthalate solution.

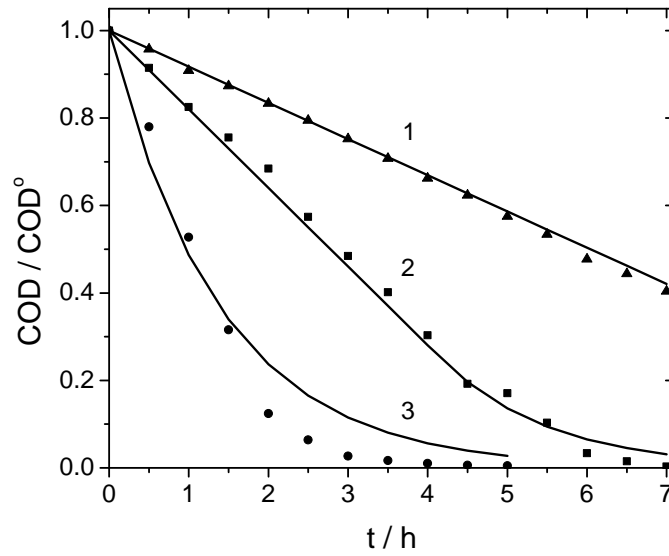


Figure 6.2. Evolution of chemical oxygen demand COD, normalized to the initial value, during electrochemical oxidation of formic acid (30 mM) in 1 M HClO₄ on BDD anode at: 1) current control (1.4 mA cm²), 2) mixed current-mass transport control (3 mA cm²), 3) mass transport control (15 mA cm²). Comparison of experimental data (points) with the theoretical model (solid line).

The instantaneous current efficiency ICE , defined as a part of the current used for formic acid electrooxidation, was calculated from the variation of COD , measured at regular intervals (Δt), using the following equation:

$$ICE = 4FV \frac{(COD)_t - (COD)_{t+\Delta t}}{I\Delta t} \quad (6.9)$$

where $(COD)_t$ and $(COD)_{t+\Delta t}$ (mol O₂ m⁻³) are the chemical oxygen demands at times t and Δt , respectively, I (A) is the current, and V (m⁻³) is the volume of the electrolyte.

6.4 Results and discussion

6.4.1 Bulk electrolysis of formic acid under different electrolysis regimes

The bulk electrolysis of 30 mM formic acid in 1 M HClO₄ was performed on BDD electrode in a reactor shown in Fig. 6.1. Using Eq. 2.7, the initial limiting current density was calculated to be 12 mA cm². In order to study the different electrolysis regimes: (1) current control, (2) mixed current-mass transport control, and (3) mass transport control, the electrolysis of formic acid was carried out at several current densities in the range of 1.4–15 mA cm². Figures 6.2 shows the evolution of the chemical oxygen demand COD , normalized to the initial value COD^0 , as a

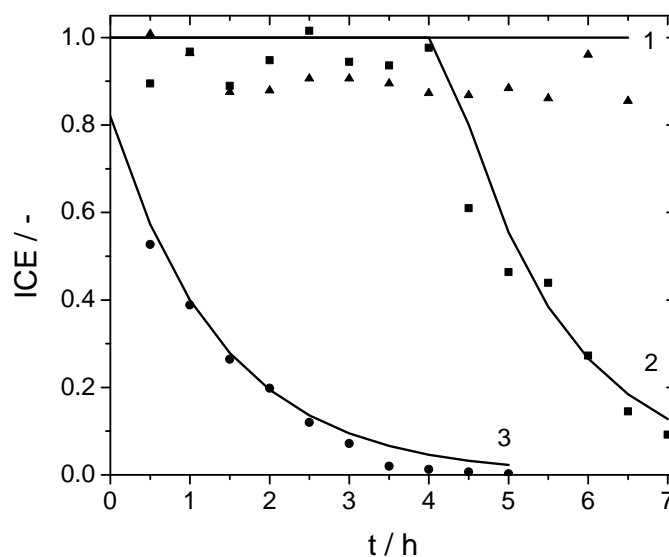


Figure 6.3. Evolution of ICE during electrochemical oxidation of formic acid on BDD anode. Experimental conditions as in Fig. 6.2.

function of time in three investigated cases. The corresponding instantaneous current efficiency ICE , calculated using Eq. 6.9, is shown in Fig. 6.3. The experimental data (points) are compared with the theoretical model (solid line) which is summarized in Table 6.1.

The COD values exhibit a linear decrease with time (curve 1 in Fig. 6.2) under conditions of current control ($j_{apply} < j_{lim}$) corresponding to an instantaneous current efficiency of $\sim 100\%$ (curve 1 in Fig. 6.3). In the mixed regime (curve 2 in Fig. 6.2 and 6.3), the COD decreases linearly, whereas ICE remains near 100% , in the initial part of the experiment (current control). After a critical time, both COD and ICE decrease exponentially what corresponds to the mass transport control ($j_{apply} > j_{lim}$). Curve 3 in Fig. 6.2 and 6.3 corresponds to pure mass transport-control in which, throughout experiment, both COD and ICE decrease exponentially. In this electrolysis regime, oxygen evolution proceeds simultaneously to formic acid oxidation. For all three investigated cases a good agreement between experimental results and the theoretical kinetic model is observed.

6.4.2 Bulk electrolysis of formic acid under programmed current

As shown in section 6.2, in order to work at 100% of current efficiency throughout experiment, electrolysis needs to be carried out under programmed current, in which the applied current density is continuously adjusted to the limiting current density. In order to validate this model, the multiple

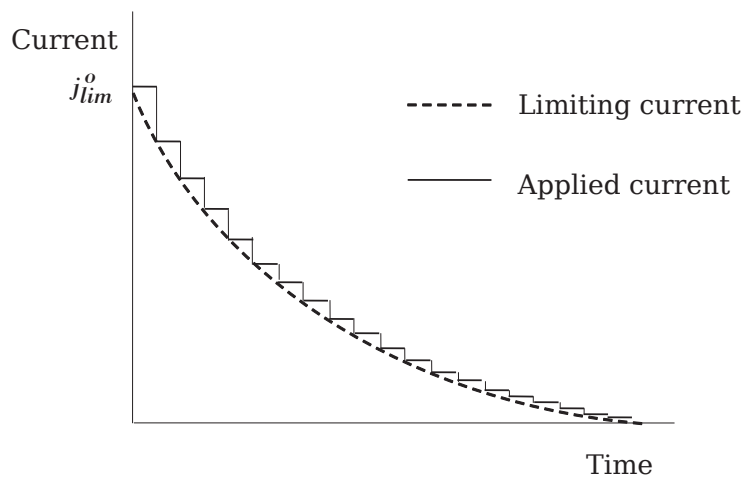


Figure 6.4. Schematic current-time curve during multiple step electrolysis.

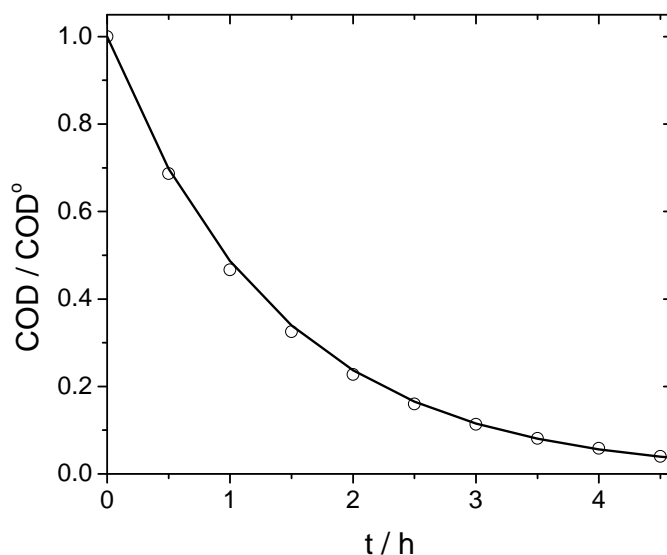


Figure 6.5. Evolution of COD during electrochemical oxidation of formic acid (30 mM) in 1 M HClO₄ on BDD anode. The applied current was adjusted during experiment to the limiting current. Comparison of the experimental data (points) with the theoretical model (solid line).

steps electrolysis of formic acid was performed, as schematically shown in Fig. 6.4. Thus, the electrolysis started by application of a initial limiting current density equal to 12 mA cm². After each 30 min, the sample was taken and the *COD* and j_{lim} were evaluated in order to adjust the applied current to the limiting value j_{lim} .

Figure 6.5 presents evolution of the chemical oxygen demand *COD*, normalized to the initial value COD^0 , as a function of time. The corresponding instantaneous current efficiency *ICE*, calculated using Eq. 6.9, is shown in Fig. 6.6. The experimental data (points) are compared with

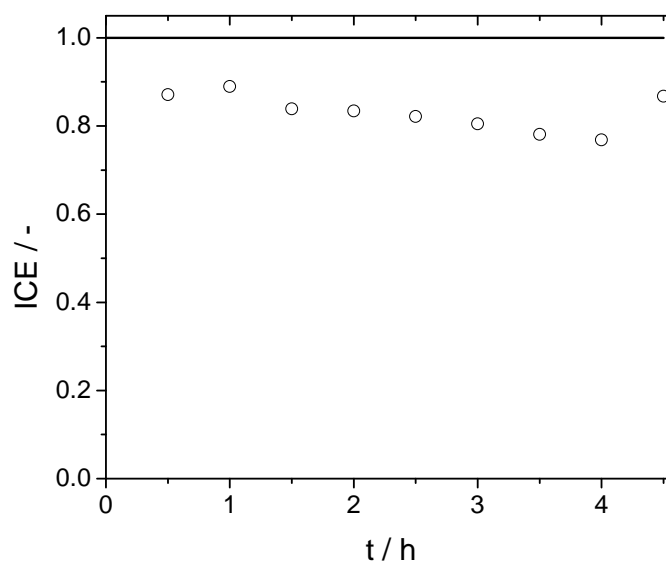


Figure 6.6. Evolution of ICE during electrochemical oxidation of formic acid on BDD anode. Comparison of the experimental data (points) with the theoretical model (solid line). Experimental conditions as in Fig. 6.5.

theoretical model (solid line). It can be seen that throughout experiment, *COD* decreases exponentially whereas *ICE* remains close to 100 %. Again, there is a good agreement between the experimental and predicted values.

6.5 Conclusions

In this chapter, a theoretical model for prediction of the evolution of chemical oxygen demand and instantaneous current efficiency [22] has been used to optimize the performance of batch recirculation system for degradation of organic compounds on boron-doped diamond electrode. The electrolysis performed under programmed current allowed to achieve fast (exponential) mineralization of formic acid with the current efficiency near 100% . Thus, by operating at the limiting current throughout electrolysis, the secondary reactions, such as oxygen evolution, are minimized, i.e., the applied current is used only for organics degradation what reduces consumption of energy.

Chapter 7

Electrochemical Oxidation of Acetic Acid on BDD; Voltammetric and Chronoamperometric Study

The electrochemical oxidation of most of the organic compounds proceeds on BDD in a similar way to that of C₁-organic compounds (chapter 5). The electrooxidation of acetic acid, however, revealed that acetic acid adsorbs on a BDD surface resulting in an auto-inhibition of its oxidation (oxidation is shifted toward higher potentials). Both the adsorption and auto-inhibition are fully reversible with respect to the concentration, indicating the existence of physical interactions between acetic acid and the electrode surface. Acetic acid appeared to be an inhibitor not only for its own oxidation but also for that of other compounds (Ce³⁺ and HCOOH) that undergo oxidation at high anodic potentials (i.e., in the vicinity of oxygen evolution). This inhibition effect can be explained by the adsorption of acetic acid on the BDD surface leading to the displacement of water from the surface and consequent decrease of water discharge rate.

This chapter is based on the following publication:

A. Kapałka, G. Fóti and C. Comninellis. Investigations of the anodic oxidation of acetic acid on boron-doped diamond electrodes, *J. Electrochem. Soc.*, 155 (2008) E27.

7.1 Introduction

Acetic acid is one of the most refractory organic compounds towards oxidation [90, 91]. In fact, the oxidation of acetic acid with O_2 (air) is difficult even at a high temperature ($300^\circ C$) and pressure (100 bar) in the wet air oxidation process (WAO). As a consequence, acetic acid appears as a final product of oxidation of many organic compounds [92].

On boron-doped diamond electrodes, acetic acid is one of the main intermediates formed during electrochemical mineralization of wastewaters containing aromatic compounds [93, 94]. Nevertheless, its electrooxidation has widely been studied mainly on platinum electrodes, whereas on BDD only a few results have been reported [95, 96, 97]. A number of studies performed on platinum electrodes showed that adsorption plays an important role in electrooxidation of acetates [98, 99, 100]. Wieckowski et al. [101, 102] found that, in acidic solutions, acetic acid adsorbs on platinum, rhodium and gold electrode. The adsorption process was reversible with respect to both the electrode potential and the bulk concentration of acetic acid and it was not accompanied by an electron transfer. Boron-doped diamond electrodes, however, are well known from their rather weak adsorption properties [19]. Thus, in principle, the adsorption of acetic acid on BDD is not expected.

In this chapter, the electrochemical oxidation of acetic acid, in a wide range of concentrations, is studied in 1 M $HClO_4$ on BDD anode. Electrochemical methods, such as voltammetry and chronoamperometry were used to study the kinetics of its electrooxidation. Furthermore, the influence of acetic acid on the electrochemical behavior of the $Ce^{3+/4+}$ redox couple and formic acid electrooxidation is also investigated.

7.2 Experimental details

Electrochemical measurements were carried out in a single-compartment, three-electrode cell using an Autolab PGSTAT 30. The counter electrode was a Pt wire, the working electrode was BDD macroelectrode (geometric area 0.38 cm^2 , B/C 6000 ppm) or BDD MEA (Fig. 4.1) and the reference electrode was $Hg/Hg_2SO_4/K_2SO_4$ (sat) (MSE; 0.64 V vs. SHE). All voltammetric measurements were performed at room temperature, in 1 M $HClO_4$ as a supporting electrolyte.

The diffusion coefficient of Ce^{3+} and Ce^{4+} was evaluated from Eq. 7.1 considering domination

of spherical diffusion, without overlapping, at each microelectrode in the array of BDD MEA [67]

$$I_{lim} = n4zFDcr \quad (7.1)$$

where I_{lim} (A) is the limiting current, z is the number of exchanged electrons, D ($\text{cm}^2 \text{s}^{-1}$) is the diffusion coefficient, c (mol cm^{-3}) is the $\text{Ce}^{3+/4+}$ concentration, r (cm) is the radius of a single microelectrode in the array, and n is the number of microelectrodes in the array (473).

The diffusion coefficient of formic acid on BDD macroelectrode was calculated from Eq. 7.2, considering a totally irreversible system [67]

$$I_p = 2.99 \times 10^5 z \alpha^{1/2} A c_R D^{1/2} \nu^{1/2} \quad (7.2)$$

where I_p (A) is the current peak, A (cm^2) is the electrode surface, ν (V s^{-1}) is the scan rate, c_R (mol cm^{-3}) is the organic concentration, and α is the transfer coefficient calculated from Eq. 7.3

$$|E_p - E_{p/2}| = \frac{47.7}{\alpha} \quad (7.3)$$

where E_p (mV) is the peak potential and $E_{p/2}$ (mV) is the potential where the current is at half of the peak value.

7.3 Results

7.3.1 Anodic polarization curves

Figure 7.1 shows polarization curves recorded on BDD microelectrodes-array (MEA) in the absence and presence of different concentrations of CH_3COOH in 1 M HClO_4 supporting electrolyte. It can be seen that in the potential region of water stability on BDD electrodes, no significant change in electrochemical response with respect to the supporting electrolyte is observed in the presence of acetic acid. However, in the oxygen evolution region, the polarization curves are shifted in presence of acetic acid. This shift depends strongly on the acetic acid concentration. At low acetic acid concentrations, the polarization curves (curves 2–6) are shifted towards lower potentials, although the inverse situation occurs close to the onset oxidation potential. In fact, the shift of the I – V curves to lower potentials has already been observed in the case of other organic compounds, such as formic acid and methanol, and has been explained by a fast reaction between

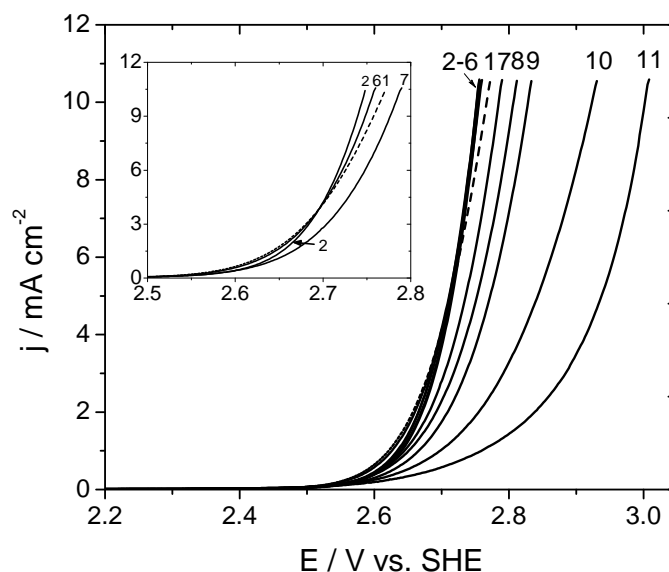


Figure 7.1. Polarization curves recorded on BDD MEA at 2 mV s^{-1} in presence of acetic acid : (1) 0 mM, (2) 2.5 mM, (3) 5.0 mM, (4) 7.5 mM, (5) 10 mM, (6) 25 mM, (7) 50 mM, (8) 75 mM, (9) 100 mM, (10) 250 mM, (11) 500 mM; electrolyte 1 M HClO_4 ; $T = 25^\circ\text{C}$.

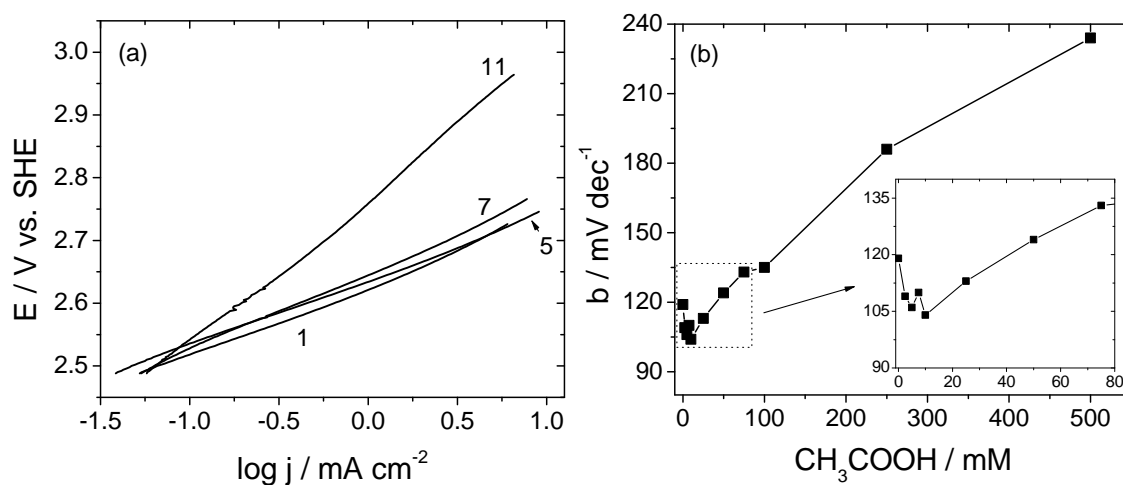


Figure 7.2. (a) The Tafel plots obtained from the I – V curves in Fig. 7.1, (b) the corresponding Tafel slopes as a function of acetic acid concentration.

organics and hydroxyl radicals (chapter 5, sec. 5.4). Above a critical acetic acid concentration, the entire I – V curves are shifted towards more positive potentials (curves 7–11).

7.3.2 Anodic Tafel plots

Figure 7.2a shows the Tafel plots for 0, 10, 50 and 500 mM CH_3COOH obtained from I – V curves in Fig. 7.1. In the whole investigated potential region ($> 2.5 \text{ V vs. SHE}$), the Tafel plots show a

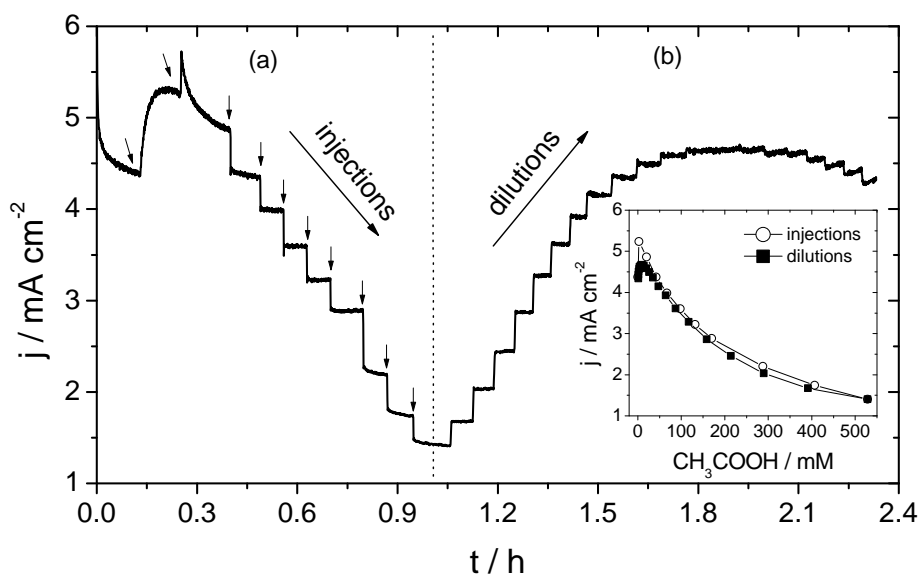


Figure 7.3. Current response of a BDD MEA electrode, polarized at 2.65 V vs. SHE, to step-by-step additions of acetic acid (a) and subsequent dilutions (b). Inset shows the current density as a function of concentration during injections of acetic acid (—○—) and dilutions of the solution (—■—) in the electrochemical cell; electrolyte 1 M HClO_4 ; $T = 25^\circ\text{C}$.

good linearity. Figure 7.2b presents corresponding Tafel slopes as a function of acetic acid concentration. The b value obtained in 1 M HClO_4 (120 mV dec^{-1}) indicates that the rate determining step of oxygen evolution on BDD is the discharge of water to hydroxyl radicals (Eq. 2.2). Furthermore, this figure shows that in presence of acetic acid the Tafel slopes first decrease reaching a minimum (corresponding to the critical acetic acid concentration), then increase with increasing acetic acid concentration reaching a value of 240 mV dec^{-1} at 500 mM acetic acid.

7.3.3 Effect of the concentration on acetic acid electrooxidation

Figure 7.3a shows the current response of a BDD MEA electrode polarized at 2.65 V vs. SHE to step-by-step addition of acetic acid in a 1 M HClO_4 supporting electrolyte. This figure shows that for the first additions, corresponding to low acetic acid concentrations ($< 40 \text{ mM}$), the current density increases, as expected from the I – V measurements (Fig. 7.1), then it decreases with further increase of acetic acid concentration. It is interesting to see that dilution of the solution in the cell with fresh electrolyte results in a complete recovery of the initial current density (Fig. 7.3b). Inset of Fig. 7.3 presents the corresponding current density as a function of concentration during injections of acetic acid and dilutions of the solution in the electrochemical cell. A high reversibility of acetic acid oxidation with respect to the concentration can be observed.

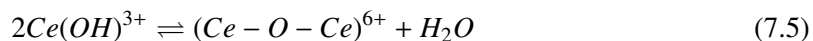
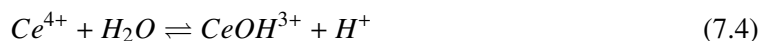
7.3.4 Effect of the potential on acetic acid electrooxidation

Figure 7.4 shows the current response of a BDD MEA electrode, polarized at three different potentials (2.55, 2.60 and 2.65 V vs. SHE), to step-by-step addition of acetic acid in a 1 M HClO₄ supporting electrolyte. For the three investigated potentials, the current density firstly increases, passes through a maximum (at the critical concentration) then decreases as the concentration of acetic acid increases. Insets of Fig. 7.4 show corresponding current density as a function of acetic acid concentration.

Figure 7.5 shows the current density from Fig. 7.4 in terms of current of acetic acid electrooxidation normalized to its maximum. This figure shows that the higher is the potential, the lower is the critical concentration, at which the maximum rate is obtained, and the stronger is decay of the current density.

7.3.5 Behavior of Ce^{3+/4+} redox couple in presence of acetic acid

Figure 7.6a shows the cyclic voltammograms recorded for several equimolar solutions of Ce^{3+/4+} in 1 M HClO₄ at BDD MEA. Ce^{3+/4+} has high positive redox potential ($E^o = +1.70$ V in 1 M HClO₄ [67]), thus, the anodic plateau interferes with the oxygen evolution reaction. Both the anodic and the cathodic plateau current density depend linearly on the concentration of cerium. Using Eq. 7.1, the diffusion coefficient of Ce³⁺ and Ce⁴⁺ was found to be 0.90×10^{-5} cm² s⁻¹ and 0.34×10^{-5} cm² s⁻¹, respectively, in accordance with [103]. In HClO₄, the difference in the diffusion coefficients and in the height of anodic and cathodic signal (Fig. 7.6a) is attributed to hydrolysis of Ce⁴⁺ (Eq. 7.4) and dimerization of the hydrolysis product (Eq. 7.5) [104, 103].



As reported by Maeda et al. [103], in the case of the Ce^{3+/4+} redox couple, the anodic signal is approximately two times higher than the cathodic one.

Figure 7.6b shows the comparison of cyclic voltammograms recorded at BDD MEA for 2 mM Ce^{3+/4+} and varying acetic acid (0–500 mM) solutions. It is seen that acetic acid does not influence the reduction of Ce⁴⁺, whereas the oxidation of Ce³⁺ is shifted towards higher potentials. As

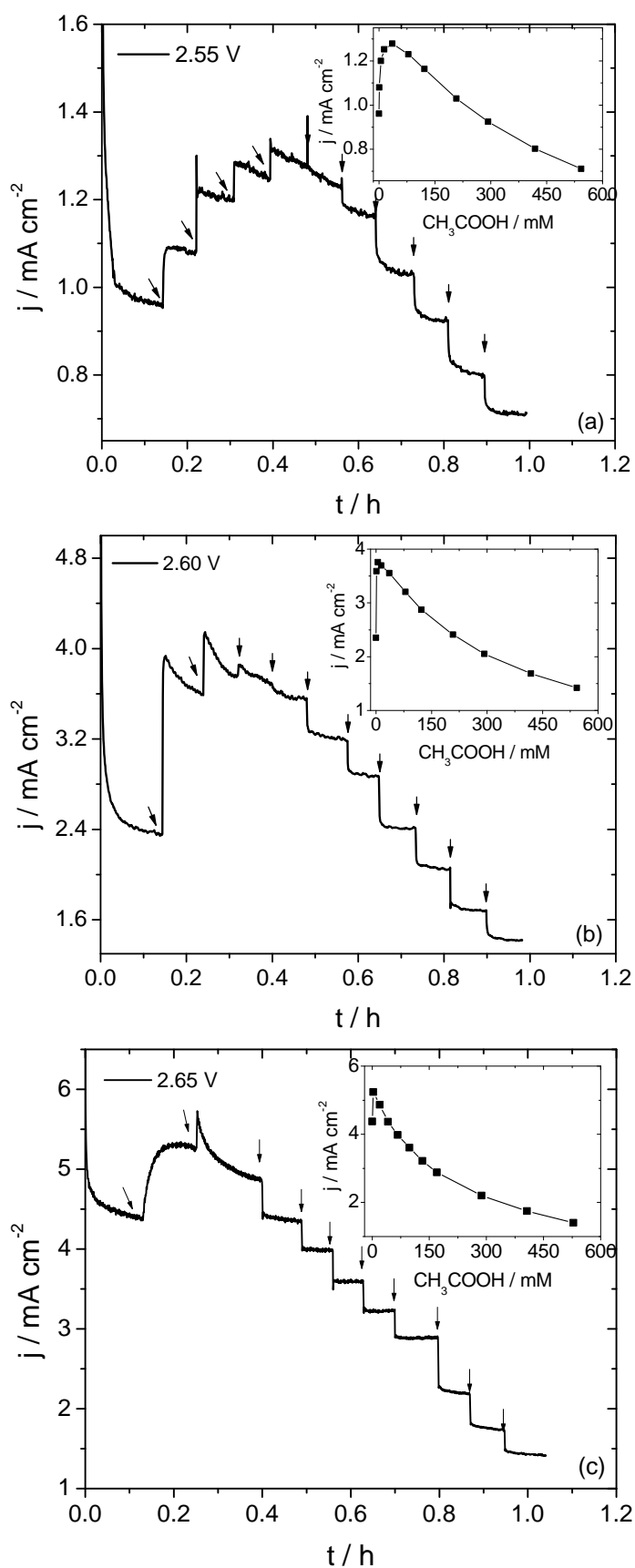


Figure 7.4. Current response of BDD MEA to step-by-step injections of acetic acid (marked by arrows) at several polarization potentials: 2.55 (a), 2.60 (b) and 2.65 V vs. SHE (c); electrolyte 1 M HClO_4 ; $T = 25^\circ\text{C}$. Insets show the current density as a function of acetic acid concentration.

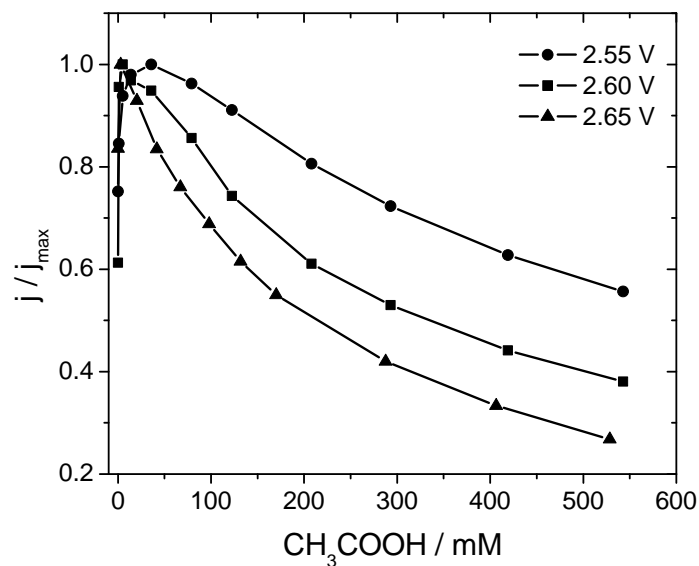


Figure 7.5. Normalized current of acetic acid electro-oxidation as a function of its concentration, calculated from data in Fig. 7.4.

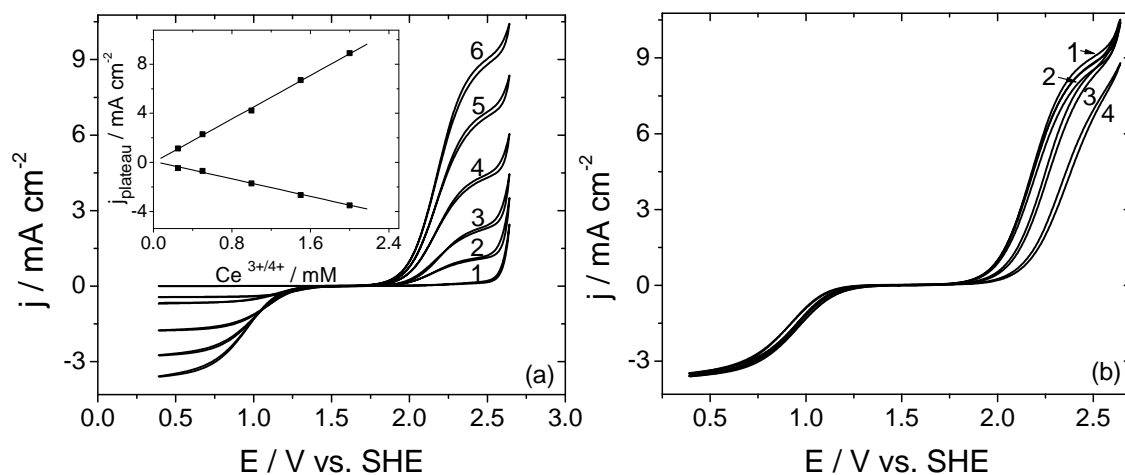


Figure 7.6. Cyclic voltammograms recorded on BDD MEA in equimolar $\text{Ce}^{3+/4+}$ solutions; scan rate 50 mV s^{-1} ; electrolyte 1 M HClO_4 ; $T = 25^\circ\text{C}$. (a) As a function of cerium concentration: (1) 0 mM, (2) 0.25 mM, (3) 0.5 mM, (4) 1.0 mM, (5) 1.5 mM, (6) 2 mM. The inset shows the plateau current density as a function of cerium concentration. (b) In $2 \text{ mM Ce}^{3+/4+}$ as a function of acetic acid concentration: (1) 0 mM, (2) 5 mM, (3) 50 mM, (4) 500 mM.

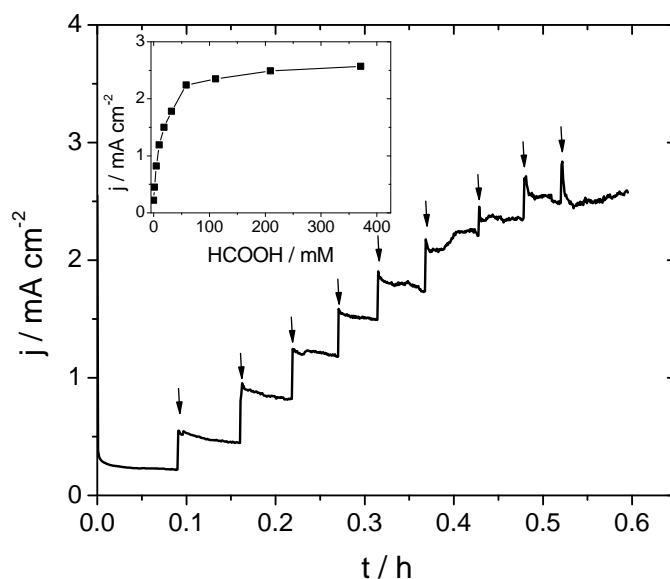


Figure 7.7. Current response of BDD MEA polarized at 2.55 V vs. SHE, to step-by-step injections of formic acid (marked by arrows). Inset shows the current density as a function of formic acid concentration; electrolyte 1 M HClO_4 ; $T = 25^\circ\text{C}$.

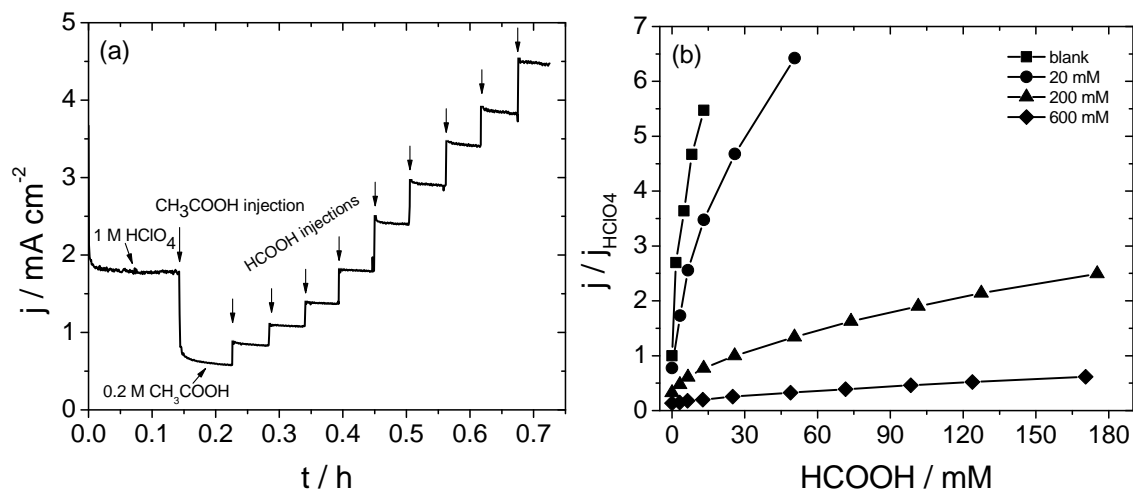


Figure 7.8. (a) Current response of BDD MEA, polarized at 2.65 V vs. SHE, to step-by-step injections of formic acid to the solution of 1 M HClO_4 +0.2 M CH_3COOH ; b) Normalized current as a function of formic acid concentration for several acetic acid solutions in 1 M HClO_4 : (—■—) 0 mM, (—●—) 0.02 M (—▲—) 0.2 M, (—◆—) 0.6 M. All data were recorded at polarization potential of 2.65 V vs. SHE; $T = 25^\circ\text{C}$.

a consequence, the anodic plateau overlaps completely with oxygen evolution and is no longer visible.

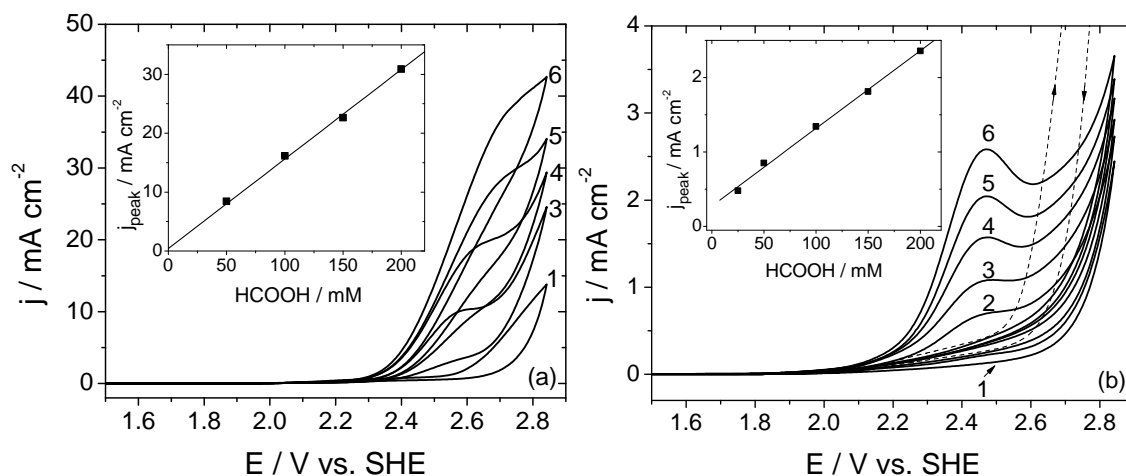


Figure 7.9. Cyclic voltammograms for the electrooxidation of formic acid (1) 0 mM, (2) 25 mM, (3) 50 mM, (4) 100 mM, (5) 150 mM, (5) 200 mM in the absence (a) and presence (b) of 500 mM acetic acid at BDD electrode; scan rate 50 V vs. SHE; electrolyte 1 M HClO_4 ; $T = 25^\circ\text{C}$. Dotted line in Fig. 7.9b shows the voltammogram of the supporting electrolyte in absence of acetic acid (identical to curve (1) in Fig. 7.9a). The insets show the peak current density as a function of formic acid concentration.

7.3.6 Formic acid electrooxidation in presence of acetic acid

Figure 7.7 shows the current response of a BDD MEA electrode, polarized at 2.55 V vs. SHE, to step-by-step addition of formic acid to 1 M HClO_4 supporting electrolyte. Contrary to the case of acetic acid (Fig. 7.3(a)), increasing concentration of formic acid seems to not affect the rate of its oxidation as the current continuously increases with subsequent injections reaching a plateau. This increase of the current is also observed when formic acid is added to a solution containing 200 mM acetic acid (Fig. 7.8a). Figure 7.8b shows the normalized current with respect to that of supporting electrolyte as a function of formic acid concentration for several acetic acid solutions (0, 20, 200 and 600 mM). It can be seen that the rate of formic acid oxidation decreases as the concentration of acetic acid increases. This is an indication that acetic acid influences oxidation of formic acid.

Figure 7.9 shows the cyclic voltammograms of several formic acid solutions in the absence (Fig. 7.9a) and presence (Fig. 7.9b) of acetic acid (500 mM) recorded on BDD macroelectrode. The oxidation of formic acid results in appearance of an oxidation wave close to the oxygen evolution region (Fig. 7.9a). This reaction is mass transfer limited since the current density of the pseudo-plateau varies linearly with the formic acid concentration (inset of Fig. 7.9a). In presence of acetic acid, the current density corresponding to both formic acid oxidation and oxygen evolution decreases radically (Fig. 7.9b). Furthermore, the oxygen evolution reaction seems to be

shifted to the higher potential region. As a consequence, the oxidation of formic acid does not overlap with oxygen evolution resulting in a well-shaped peak response. The peak current density varies linearly with formic acid concentration (inset of Fig. 7.9b), however the trend line does not pass through the origin. From Fig. 7.9a and using Eq. 7.2, the diffusion coefficient of formic acid in absence of acetic acid is found to be $1.84 \times 10^{-5} \text{ cm}^2 \text{ s}^{-1}$. This value corresponds well to that found in the literature ($1.69 \times 10^{-5} \text{ cm}^2 \text{ s}^{-1}$ [87]). In presence of acetic acid, the diffusion coefficient of formic acid, calculated from Fig. 7.9b using Eq. 7.2, is found to be $8.34 \times 10^{-8} \text{ cm}^2 \text{ s}^{-1}$.

7.4 Discussion

Considering a simplified mechanism of organics oxidation on BDD anode, presented in chapter 5 (Eq. 2.2, 5.10, 4.8), in presence of acetic acid, the initial decrease in the Tafel slope with respect to the supporting electrolyte (Fig. 7.2) could be related to the indirect oxidation of acetic acid via electrogenerated hydroxyl radicals (Eq. 5.10), which becomes the rate determining step. The presence of a minimum and the further increase of Tafel slopes at high acetic acid concentrations could indicate a competition between the indirect oxidation of acetic acid via electrogenerated hydroxyl radicals (Eq. 5.10) and the inhibition of the water discharge reaction (Eq. 2.2). This inhibition seems to be strongly dependent on the acetic acid concentration. The global effect is a decrease in the rate of acetic acid oxidation at a given potential with increasing acetic acid concentration. We are dealing with an auto-inhibition of acetic acid oxidation on BDD electrodes. Nevertheless, the oxidation of acetic acid is still possible at the higher anodic potentials (Fig. 7.1). In fact, these results are in agreement with Gandini et al. [95] who showed that complete mineralization of acetic acid on BDD is feasible.

Conclusion about the auto-inhibiting effect of acetic acid on its oxidation can also be drawn from Fig. 7.3. Although from these experimental data the exact nature of surface interactions can not be concluded, to a first approximation, one can speculate that physisorption of acetic acid onto BDD surface induces the auto-inhibition effect. In fact, the observed reversibility towards acetic acid concentration (inset of Fig. 7.3) indicates that the auto-inhibition effect of acetic acid is related to weak interactions (no chemical bond formation). Moreover, inhibition by acetate ions is less probable as its concentration in 1 M HClO_4 is negligible (pK_a of acetic acid is 4.77).

Figures 7.4 and 7.5 show that the higher is the potential, the lower is the critical concentration at which the maximum rate of electrooxidation is obtained, and the stronger is the auto-inhibition

effect. These experimental results show that the extent of acetic acid adsorption on BDD is much more potential dependent than the rate of acetic acid oxidation. It is worthwhile to notice, that close to the critical concentration some current instability occurs (Fig. 7.4). These instabilities might be related to the competition between the oxidation of acetic acid, via electrogenerated hydroxyl radicals, and the auto-inhibition of acetic acid oxidation by physisorbed acetic acid.

Acetic acid appeared to be an inhibitor not only for its own oxidation but also for that of other compounds that undergo oxidation at high anodic potentials (i.e. in the vicinity of oxygen evolution). As shown in Fig. 7.6b, acetic acid does not influence the reduction of Ce^{4+} , whereas the oxidation of Ce^{3+} is shifted towards higher potentials. This can suggest that either adsorption of acetic acid predominates at high positive potentials or the intermediates of its oxidation adsorb on the electrode surface hindering the anodic processes. The latter, however, is less probable as acetic acid is not oxidized below 2.4 V (Fig. 7.1), while Ce^{3+} is electrochemically active from 1.7 V.

Using experimental results in Fig. 7.6b, it is possible to estimate the coverage of adsorbed acetic acid at a given potential from the following relation:

$$j_{C_{HAc}, \neq 0} = (1 - \Theta) \times j_{C_{HAc}, = 0} \quad (7.6)$$

where $j_{C_{HAc}, \neq 0}$ is the current density of Ce^{3+} oxidation in the presence of acetic acid, Θ is the coverage of acetic acid, and $j_{C_{HAc}, = 0}$ is the current density of Ce^{3+} oxidation in the absence of acetic acid. Table 7.1 presents calculated Θ for 5, 50, and 500 mM CH_3COOH as a function of potential in the region of 1.8–2.1 V vs. SHE. It can be seen that Θ increases with increase of both potential and acetic acid concentration reaching a value of 0.75 for 500 mM acetic acid at 2.1 V vs. SHE.

As shown in Fig. 7.8 and 7.9, acetic acid inhibits also electrooxidation of formic acid. In fact, in the presence of acetic acid, the diffusion coefficient of formic acid was 200 times lower ($8.34 \times 10^{-8} \text{ cm}^2 \text{ s}^{-1}$) than that found in the literature ($1.69 \times 10^{-5} \text{ cm}^2 \text{ s}^{-1}$ [87]). There are two possible explanations of such a big deviation from the literature value: (1) oxidation of formic acid in presence of acetic acid can not be considered as a purely mass-transferred limited process, and (2) the electrode surface is largely occupied by acetic acid and oxidation of formic acid occurs at a tiny fraction of the whole surface. In the latter case, by comparing the peak current measured in the presence and absence of acetic acid (Fig. 7.9), the coverage of acetic acid on the electrode surface

Table 7.1. The coverage Θ of acetic acid on the BDD surface in 5, 50, 500 mM CH_3COOH , estimated from experimental data in Fig. 7.6b.

E / V vs. SHE	$\Theta_{5 \text{ mM}}$	$\Theta_{50 \text{ mM}}$	$\Theta_{500 \text{ mM}}$
1.8	0	0.24	0.47
1.9	0	0.42	0.68
2.0	0.03	0.46	0.74
2.1	0.04	0.45	0.75

is estimated to be $\sim 90\%$. In the former case (1), appearing peak in Fig. 7.9b could be related to the competition between the oxidation of formic acid and the adsorption of acetic acid onto BDD surface. In other words, above ~ 2.5 V, the adsorption of acetic acid would dominate the oxidation of formic acid leading to decrease of the current density and the peak-shaped response.

7.5 Conclusions

Contrary to most of organic compounds, CH_3COOH reversibly adsorbs on BDD anode resulting in a reversible auto-inhibition of its oxidation. In order to enhance oxidation of acetic acid it is necessary to apply higher anodic potentials. This auto-inhibition effect depends strongly on both applied potential and concentration of acetic acid. In addition to its auto-inhibition, adsorbed acetic acid acts as an inhibitor for the oxidation of other compounds requiring high anodic potentials, such as Ce^{3+} and HCOOH .

Adsorption of acetic acid might result in the displacement of water from the surface. As a consequence, the rate of water discharge to hydroxyl radicals is reduced. The elimination of water and decrease of water discharge rate could explain the auto-inhibition of acetic acid oxidation.

Chapter 8

Electrochemical Oxidation of Acetic Acid on BDD; DEMS Study

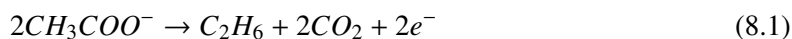
Presented in chapter 7 experimental results are not sufficient to draw conclusions about mechanism of acetic acid electrooxidation on BDD. Such investigations are undertaken in this chapter using differential electrochemical mass spectrometry (DEMS) that allows to identify products and intermediates of the reaction during a potential sweep. The measurements revealed that the main product of acetic acid oxidation is CO_2 , which is formed without showing any evidence for the direct discharge of acetic acid resulting in the Kolbe reaction. In fact, only a small amount of ethane was detected by DEMS. In addition to ethane, methanol was identified as a main intermediate of acetic acid oxidation. Based on these results, a model of indirect oxidation of acetic acid via hydroxyl radicals has been proposed.

This chapter is based on the following publication:

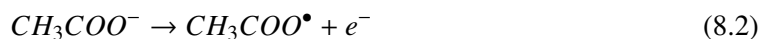
A. Kapalka, B. Lanova, H. Baltruschat, G. Fóti and C. Comninellis. DEMS study of the acetic acid oxidation on boron-doped diamond electrode, *J. Electrochem. Soc.*, 155 (2008) E96.

8.1 Introduction

On platinum electrodes, anodic oxidation of acetate ions results in Kolbe reaction [105, 106, 98, 99, 107, 108, 109] (Eq. 8.1).



This reaction consists of several steps involving the discharge of acetate ions to acetate radical (Eq. 8.2), its decomposition to methyl radical (Eq. 8.3) and recombination of the resulting methyl radicals to ethane (Eq. 8.4).



In aqueous solutions, the Kolbe reaction requires potentials that are higher than the potential of water decomposition [99, 109]. At low current densities, the acetate radicals can also react with hydroxyl radicals to give methanol and carbon dioxide. Under these conditions, the oxygen evolution reaction predominates and the contribution of the Kolbe reaction is very small. At sufficiently high current densities, the electrode surface is occupied mainly by acetate ions which displace water molecules from the surface hindering the formation of hydroxyl radicals. Under these conditions, the surface concentration of acetate radicals is sufficiently high to favor ethane formation. The critical current density for ethane formation is reached where the rate of formation of acetate radicals equals the rate of consumption of adsorbed acetate radicals with hydroxyl radicals. On the contrary, in strongly acidic media the electrooxidation of acetic acid is more difficult as mainly undissociated molecules are present in the solution [110].

As reported by Wadhawan et al. [96], the Kolbe reaction proceeds also on boron-doped diamond electrodes (BDD). The authors studied the electrochemical oxidation of aliphatic carboxylic acids in 1 M NaOH under ultrasound conditions at BDD and Pt electrode. They found that the type and the yield of products obtained from the Kolbe electrolysis were identical at both studied electrodes.

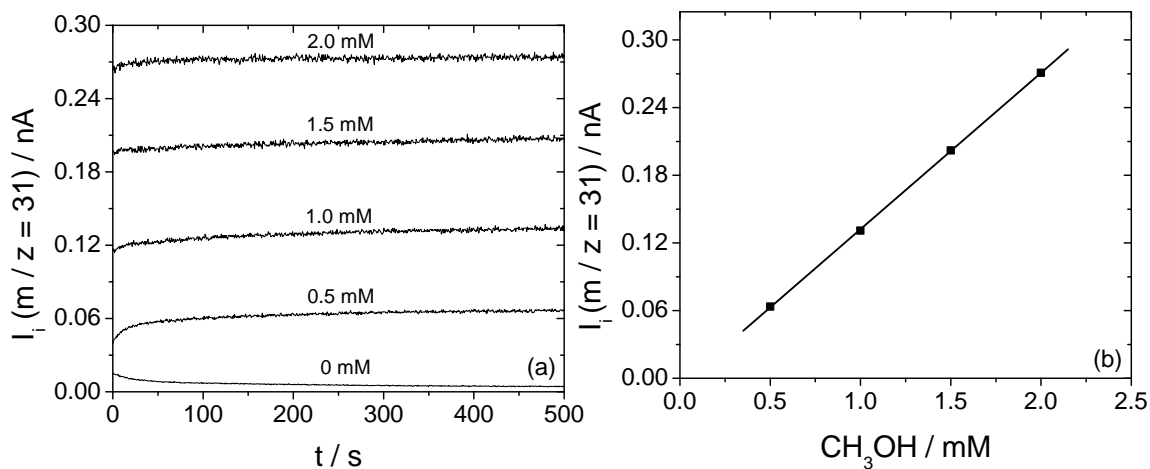


Figure 8.1. Response of the mass spectrometer for CH₃OH (0.5–2.0 mM) in 1 M HClO₄ (a) and corresponding calibration curve (b); flow rate 5 $\mu\text{l s}^{-1}$; T = 25°C.

In this work, the oxidation of acetic acid is investigated in 1 M HClO₄ on BDD anode. As *pKa* of acetic acid is 4.77, in 1 M HClO₄ mainly undissociated acetic acid molecules are present. The products of acetic acid oxidation were studied by differential electrochemical mass spectrometry (DEMS) which allows the immediate detection of reaction products after their formation during potential sweep. As a result, in parallel to faradaic current, the ionic current of $m/z = 44$ (CO₂), $m/z = 32$ (O₂), $m/z = 31$ (CH₃OH), $m/z = 30$ (C₂H₆) and $m/z = 74$ (CH₃COOCH₃) were recorded during oxidation of 1, 10, 50 and 500 mM acetic acid in 1 M HClO₄. On the basis of the obtained results, a mechanism of acetic acid oxidation has been proposed.

8.2 Experimental details

DEMS measurements were performed on BDD in a dual thin layer electrochemical cell under constant flow of 5 $\mu\text{l s}^{-1}$. All details concerning used electrodes and design of the cell are given in chapter 5, sec. 5.2. All measurements were performed at room temperature, in 1 M HClO₄ as a supporting electrolyte. The solutions were deaerated with argon during the measurements.

The rate of CO₂ and C₂H₆ formation was calculated using Eq. 8.5

$$r = \frac{I_i}{FSK^*(44)} \quad (8.5)$$

where r (mol s⁻¹) is the rate, I_i (A) is the ionic current, F (C mol⁻¹) is the Faraday constant, S is the sensitivity factor for detection of a given species ($S = 1$ and 0.48 for CO₂ and C₂H₆,

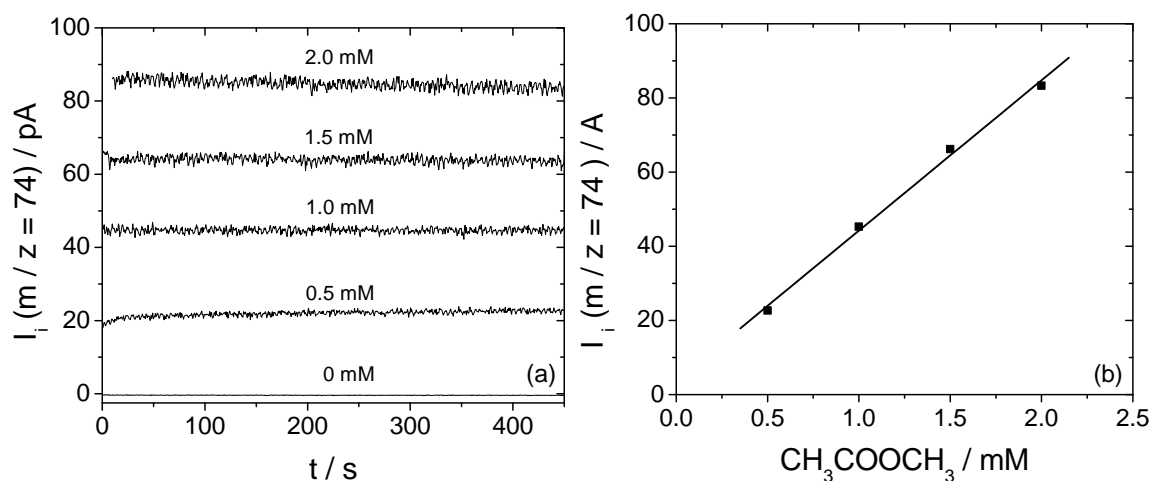


Figure 8.2. Response of the mass spectrometer for CH₃COOCH₃ (0.5–2.0 mM) in 1 M HClO₄ (a) and corresponding calibration curve (b); flow rate 5 $\mu l s^{-1}$; T = 25°C.

respectively [111]) and $K^*(44)$ is the calibration constant for CO₂, equal to 8.1×10^{-6} (chapter 5, sec. 5.2). The rate of formation of methanol and methyl acetate was calculated using Eq. 8.6

$$r = cu \quad (8.6)$$

where c (mol l⁻¹) is the concentration and u (l s⁻¹) is the flow rate. The concentration of methanol and methyl acetate formed during oxidation of acetic acid was determined using the calibration curves obtained from calibration of the mass spectrometer at several concentrations of methanol and methyl acetate in 1 M HClO₄ (Fig. 8.1 and 8.2, respectively).

The current efficiency CE of CO₂ and O₂ formation was determined from the faradaic current I_f and ionic current $I_i(44)$ and $I_i(32)$, respectively, according to Eqs. 5.6–5.9 in chapter 5 [89]. The calibration constant $K^*(32)$ was equal to 5.9×10^{-6} , and the number of electrons involved in the oxidation of acetic acid (Eq. 8.7) and oxygen evolution (Eq. 5.5) was 4.



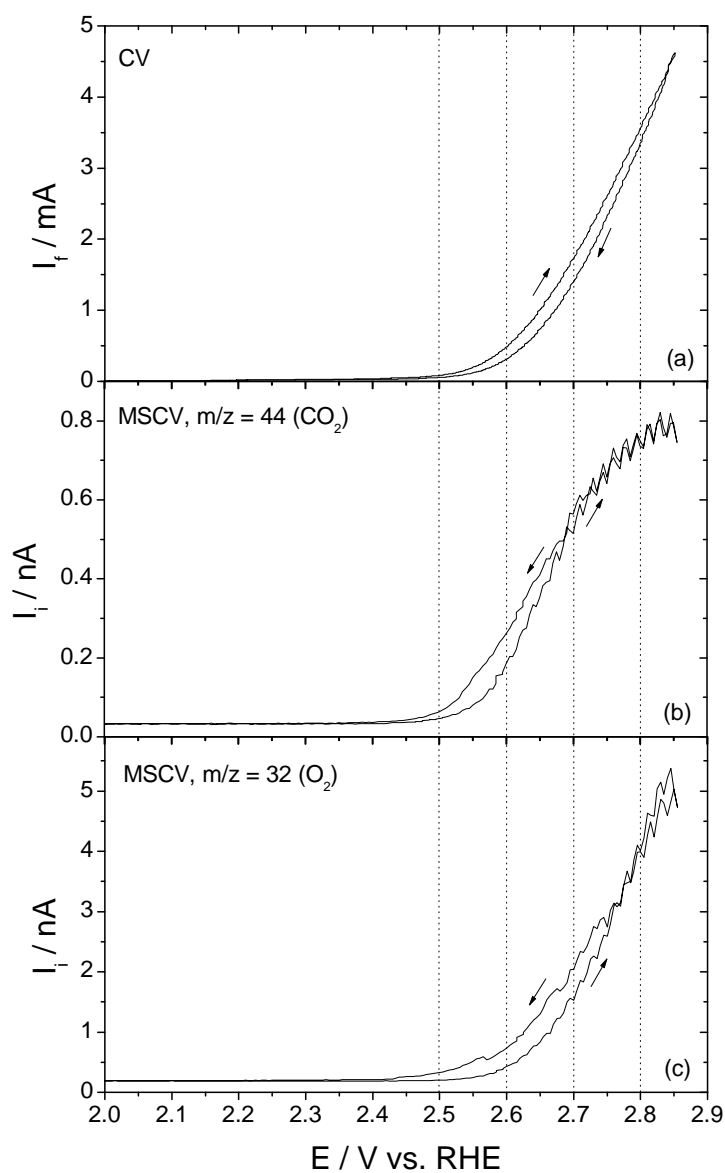


Figure 8.3. Simultaneously recorded cyclic voltammogram (CV) (a) and mass spectrometric CV (MSCV) for (b) $m/z = 44$ (CO_2) and (c) $m/z = 32$ (O_2) on BDD in 1 mM CH_3COOH ; scan rate 10 mV s^{-1} , flow rate $5 \mu\text{l s}^{-1}$, electrolyte 1 M HClO_4 ; $T = 25^\circ\text{C}$.

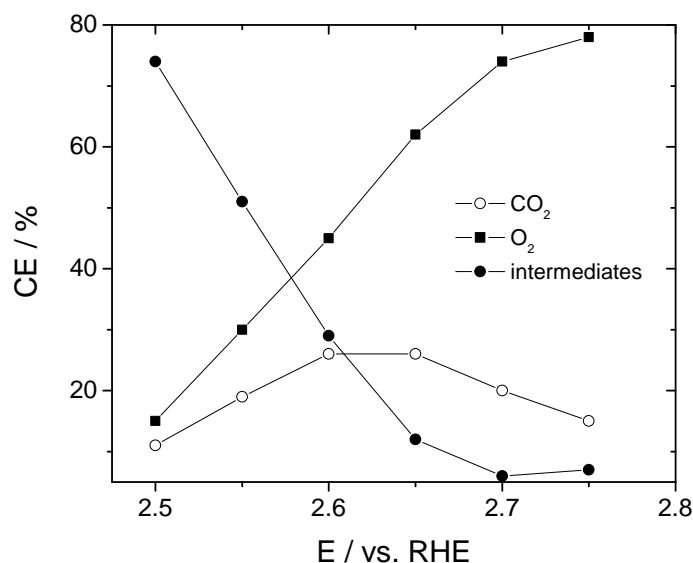


Figure 8.4. The current efficiency CE for CO_2 , O_2 , and intermediates formation during oxidation of 1 mM CH_3COOH . Experimental conditions as in Fig. 8.3.

8.3 Results

8.3.1 Electrooxidation of acetic acid

Figure 8.3 shows the cyclic voltammogram (CV) and the mass spectrometric cyclic voltammograms (MSCV) for $m/z = 44$ (CO_2) and $m/z = 32$ (O_2) simultaneously recorded on BDD during oxidation of 1 mM CH_3COOH in 1 M HClO_4 . It can be seen that the ionic current of CO_2 continuously increases from around 2.45 V vs. RHE reaching a limitation at higher potentials (Fig. 8.3b). The limiting current may indicate that the oxidation of acetic acid is mass transfer limited. O_2 starts to evolve at around 2.55 V vs. RHE (Fig. 8.3c), simultaneously to CO_2 production. As a consequence, the effect of $I_i(44)$ limitation on the faradaic current (Fig. 8.3a), which sums up the current for both CO_2 and O_2 formation, is not visible, i.e., neither a peak nor an oxidation wave is observed.

Figure 8.4 shows the corresponding current efficiency CE for CO_2 and O_2 evolution according to Eqs. 8.7 and 5.5, as a function of potential, calculated using Eqs. 5.6–5.9. $CE(\text{CO}_2)$ at first increases, and then passes through a flat maximum at ~ 2.6 V vs. RHE reaching a value of $\sim 25\%$. In parallel, $CE(\text{O}_2)$ continuously increases up to 80% at 2.75 V vs. RHE. By adding $CE(\text{CO}_2)$ to $CE(\text{O}_2)$ and subtracting from 100%, the efficiency for intermediates formation can be evaluated. It can be seen that the formation of intermediates is important in the potential region below CO_2

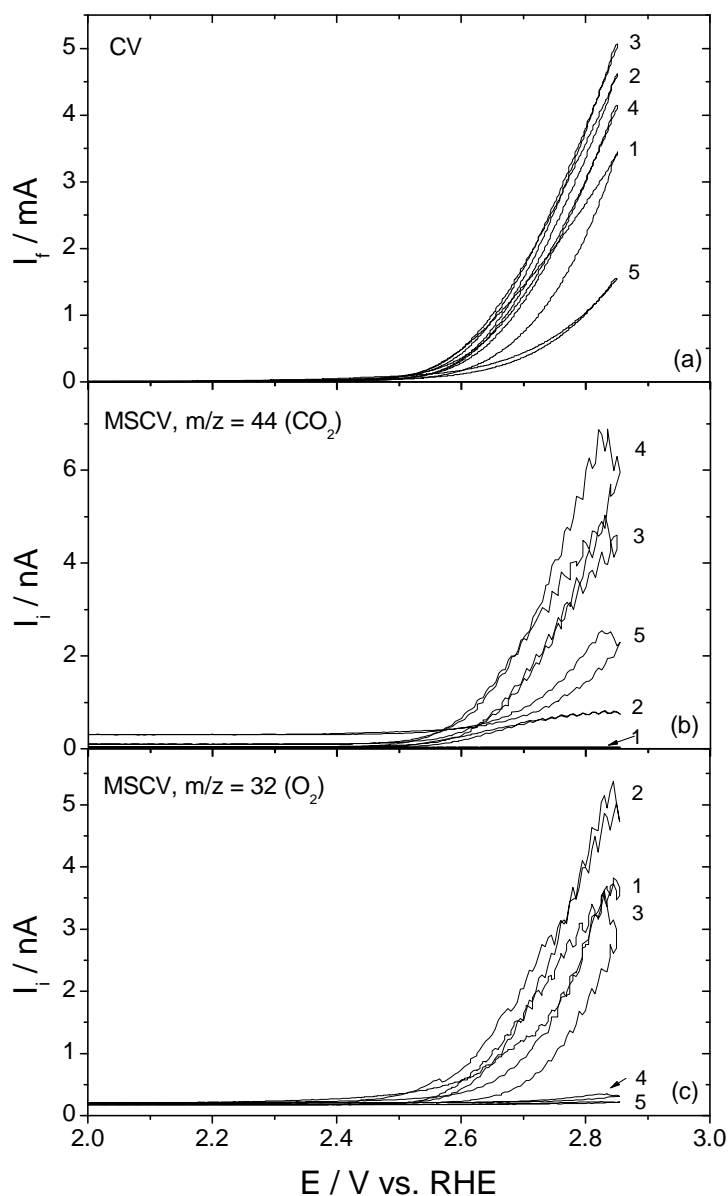


Figure 8.5. Simultaneously recorded cyclic voltammogram (CV) (a) and mass spectrometric CV (MSCV) for (b) $m/z = 44$ (CO_2) and (c) $m/z = 32$ (O_2) on BDD in (1) 0 mM, (2) 1 mM, (3) 10 mM, (4) 50 mM, (5) 500 mM CH_3COOH ; experimental conditions as in Fig. 8.3.

limitation (< 2.6 V), i. e., in the charge transfer control region, as reported previously in [32] (see also chapter 2, sec. 2.1.3).

8.3.2 Effect of acetic acid concentration

Figure 8.5 shows the comparison of CV and MSCV of $m/z = 44$ (CO_2) and $m/z = 32$ (O_2) for 1, 10, 50 and 500 mM acetic acid in 1 M HClO_4 . In the oxygen evolution region (> 2.5 V vs. RHE),

the faradaic current depends strongly on the acetic acid concentration (Fig. 8.5a). At 1 and 10 mM concentration of acetic acid, the faradaic current increases with respect to that of the supporting electrolyte (curve 1 in Fig. 8.5a), whereas starting from 50 mM a decrease of the current is observed. This phenomenon can be explained by the physisorption of acetic acid on the electrode surface resulting in the auto-inhibition of its oxidation, as discussed in chapter 7. As a consequence, the oxidation of acetic acid is shifted to higher potentials.

Figure 8.5b shows that the ionic current of CO_2 for 50 mM acetic acid, however, is much higher than that for 10 mM, indicating an unimpeded oxidation of acetic acid. To explain the decrease of faradaic current for 50 mM acetic acid, one has to take into account the oxygen evolution reaction. In fact, in comparison with 10 mM acetic acid, oxygen evolution is almost negligible in 50 mM acetic acid. Because it hardly contributes to the faradaic current, the latter, decreases with increasing acetic acid concentration. The further decline of faradaic current in 500 mM acetic acid is due to the decrease of the rate of its oxidation. It can be seen that $I_f(44)$ for 500 mM acetic acid is three times lower than that for 50 mM acetic acid.

8.3.3 Detection of intermediates

During oxidation of acetic acid on BDD electrodes, in addition to CO_2 and O_2 evolution, ethane ($m/z = 30$), methyl acetate ($m/z = 74$) and methanol ($m/z = 31$) were detected as intermediates (Fig. 8.6, 8.7 and 8.8, respectively). As their rate of formation is relatively small (Table 8.1), it can be concluded that the main product of acetic acid oxidation on BDD is carbon dioxide, which is formed without showing any evidence for direct oxidation via the Kolbe reaction. In fact, only a small amount of ethane was detected by DEMS (Fig. 8.6). The formation of methyl acetate is also almost negligible, as its ionic current (rate of formation) is very low (Fig. 8.7). Actually, methyl acetate can be detected only in 500 mM acetic acid. Comparing the results in Fig. 8.6–8.8, one can consider methanol as a main intermediate of acetic acid oxidation due to its relatively high ionic current. It is interesting to see, that ionic current of methanol reaches a limitation resulting in a clear peak and pseudo-plateau for 10 mM and 50 mM acetic acid, respectively (Fig. 8.8a and b). This indicates that, beyond a certain potential, the oxidation of methanol dominates its formation leading to the peak-shaped response. This potential is certainly related to the diffusion limitation of acetic acid oxidation. In the mass transfer control region there is a high local concentration of electrogenerated hydroxyl radicals relative to the acetic acid concentration [32]. This excess of hydroxyl radicals causes the oxidation of methanol on the BDD surface.

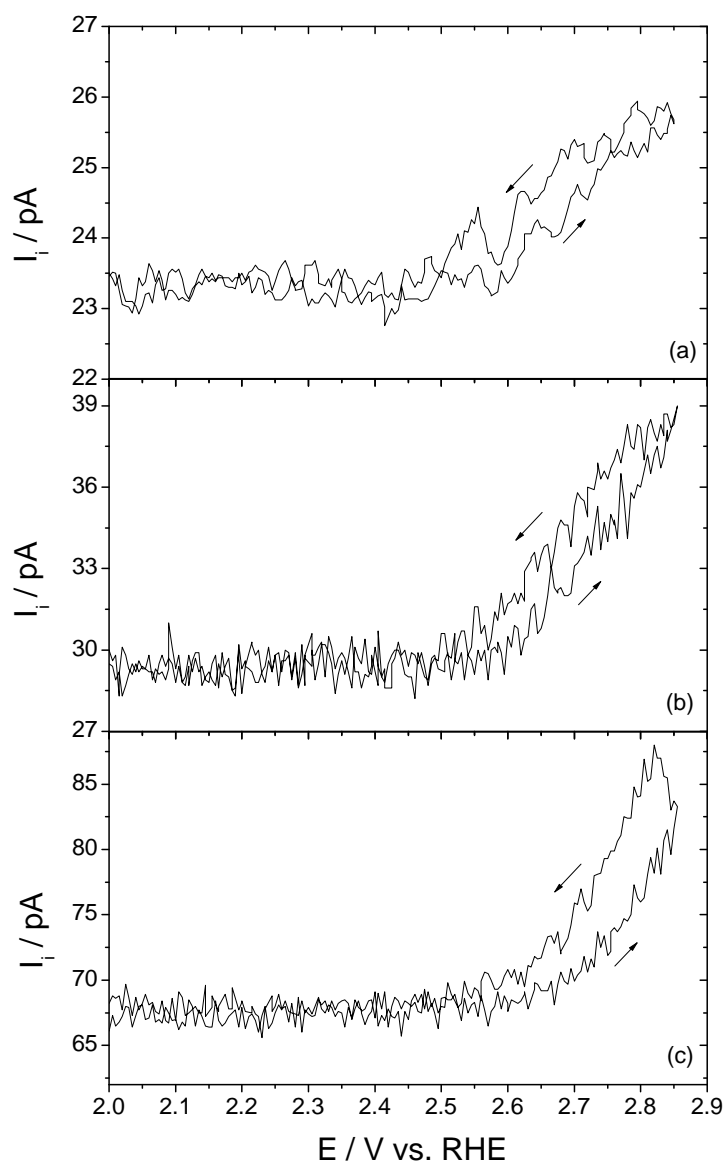


Figure 8.6. Mass spectrometric cyclic voltammograms (MSCV) of ethane ($m/z = 30$) recorded on BDD in (a) 10 mM, (b) 50 mM (c) 500 mM CH_3COOH ; experimental conditions as in Fig. 8.3.

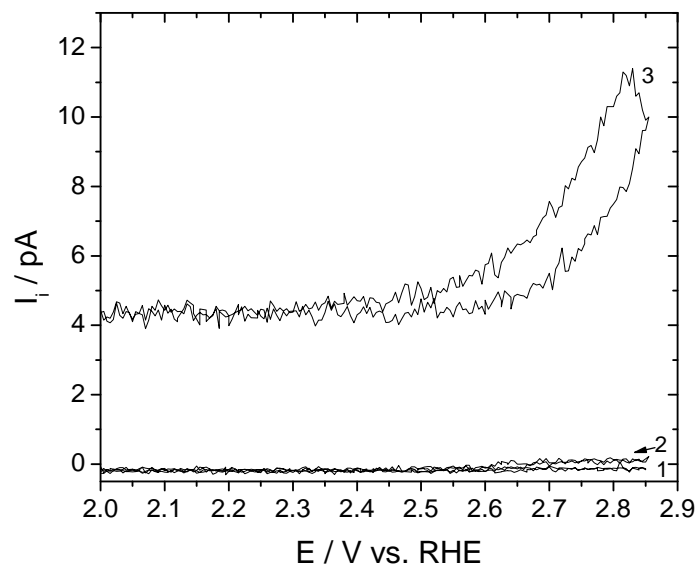


Figure 8.7. Mass spectrometric cyclic voltammograms (MSCV) of methyl acetate ($m/z = 74$) recorded on BDD in (1) 10 mM, (2) 50 mM (3) 500 mM CH_3COOH ; experimental conditions as in Fig. 8.3.

The investigations of the dependence of the ionic currents on the concentration of acetic acid shows that, although the faradaic current and the CO_2 formation rate decreases with concentration, the rate of formation of methanol, methyl acetate, and ethane increases. This indicates that at the highest acetic acid concentrations the formation rate of hydroxyl radicals is too slow and oxidation is largely incomplete.

8.4 Discussion

On the basis of these experimental results, and considering that acetic acid is physisorbed on the electrode surface, the following mechanism of acetic acid oxidation on BDD is proposed:



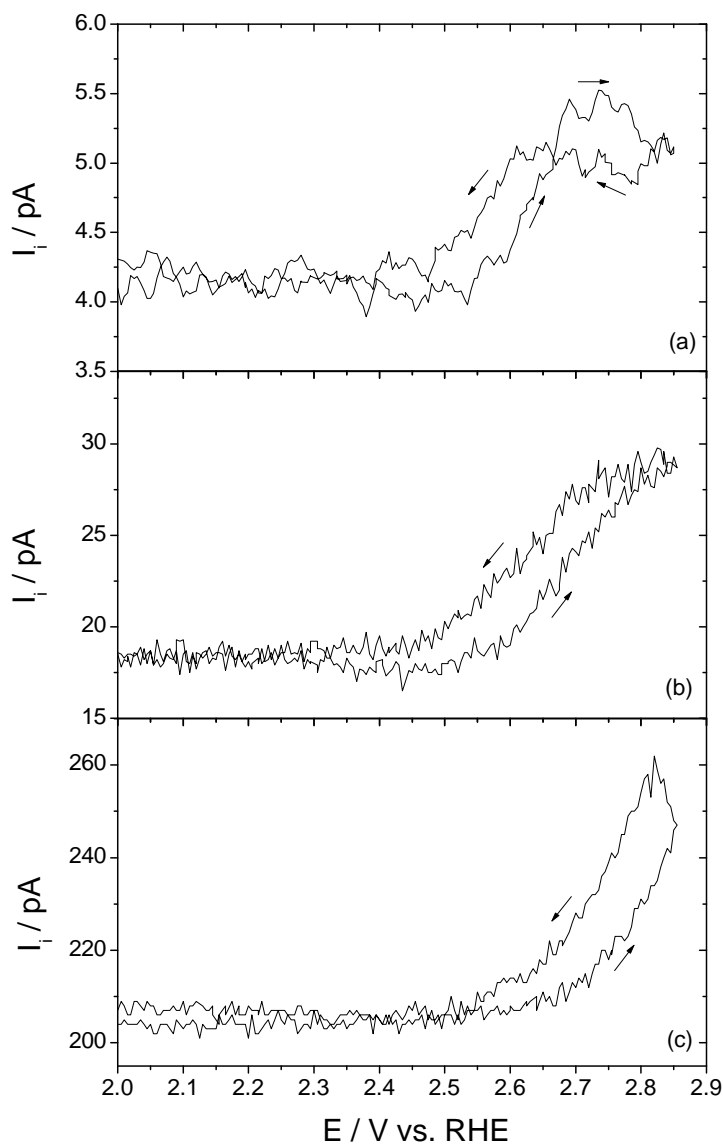
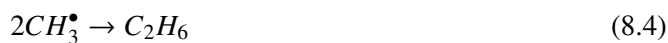


Figure 8.8. Mass spectrometric cyclic voltammograms (MSCV) of methanol ($m/z = 31$) recorded on BDD in (a) 10 mM, (b) 50 mM (c) 500 mM CH_3COOH ; experimental conditions as in Fig. 8.3.

Table 8.1. Comparison of the rate of products formation during oxidation of 500 mM CH_3COOH in 1 M HClO_4 at 2.85 V vs. RHE on BDD anode; the rate was calculated using Eq. 8.5–8.6.

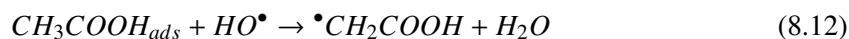
product	rate of formation / nmol s^{-1}
CO_2	2.5
CH_3OH	0.76
$\text{CH}_3\text{COOCH}_3$	0.15
C_2H_6	0.054



Upon anodic polarization, water is discharged, resulting in the formation of hydroxyl radicals (Eq. 2.2). These hydroxyl radicals abstract hydrogen from the physisorbed acetic acid forming an acetoxyl radical (Eq. 8.8). This intermediate decomposes to give methyl radical (Eq. 8.3), which can undergo further chemical reactions to form methanol (Eq. 8.9), ethane (Eq. 8.4), and methyl acetate (Eq. 8.10). The experimental data do not allow to conclude whether these intermediates are adsorbed or not on the BDD surface. Taking into account the results in Fig. 8.8, one can further consider oxidation of methanol on the electrode surface (Eq. 8.11). The oxidation of methanol certainly contributes to the total amount of CO_2 detected by DEMS.



As the energy of a C–H bond (414 kJ mol^{-1}) is comparable with that of O–H bond (463 kJ mol^{-1}), from energetic point of view, reaction 8.12 is also likely to occur, however, no evidence for that has been found in this work.



From the amount of produced methanol, methyl acetate and ethane (Table 8.1) and considering reactions 8.13–8.16, the partial rate of CO_2 and partial faradaic current can be calculated for each reaction (Table 8.2).

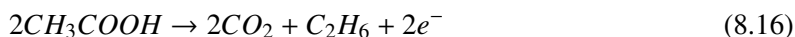
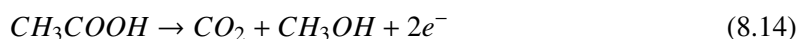


Table 8.2. The partial rate of CO₂ formation, faradaic current and current efficiency for reactions 8.13–8.16 during oxidation of 500 mM CH₃COOH in 1 M HClO₄ at 2.85 V vs. RHE on BDD anode.

	Partial rate of CO ₂ formation ^a / nmol s ⁻¹	Partial faradaic current ^b / mA	Partial current efficiency ^c / %
reaction 8.13	1.48	0.59	43.3
reaction 8.14	0.76	0.15	10.7
reaction 8.15	0.15	0.03	2.11
reaction 8.16	0.11	0.01	0.8

^a) calculated from Table 8.1 and the stoichiometry of reactions 8.13–8.16

^b) calculated from the partial rate of CO₂ formation

^c) calculated from the ratio between partial faradaic current and the corresponding total experimental faradaic current equal to 1.37 mA

The total faradaic current for reactions 8.13–8.16 is equal to 0.78 mA. The fact that the experimental current is much higher (1.37 mA) indicates that other products, e.g., formic acid might also be formed, although can not be detected by mass spectrometry.

As we reported in chapter 7, the auto-inhibition of acetic acid oxidation can be explained by the displacement of water from the electrode surface by acetic acid and the decrease of water discharge rate. In general, these conditions should be favorable for the direct oxidation of acetic acid on BDD, as observed on platinum electrode (sec. 8.1). Nevertheless, in our case no direct oxidation is observed, due presumably to the well known non-catalytic character of this anode. As a consequence, acetic acid accumulates on the BDD surface causing the auto-inhibition of its oxidation (Fig. 8.5).

8.5 Conclusions

DEMS measurements presented in this chapter indicate that the direct oxidation of acetic acid does not occur in 1 M HClO₄. The direct discharge of acetic acid, which could probably result in the Kolbe reaction, is not observed even at high acetic acid concentrations at which the electrode surface is occupied mainly by physisorbed acetic acid.

In acidic solution, acetic acid is oxidized indirectly via hydroxyl radicals formed by water discharged at the BDD surface resulting in the formation of methanol, methyl acetate and ethane as intermediates. At small concentrations, oxidation of acetic acid proceeds in parallel to oxygen evolution whereas at higher concentrations, the oxygen evolution is negligible in investigated potential region. This indicates that oxidation of acetic acid is a main reaction in the studied system. At a high concentration of acetic acid, the rate of water discharge is strongly lowered by

physisorbed acetic acid, causing an inhibition of oxidation of the latter. As a consequence, the oxidation of acetic acid is shifted to higher potentials.

Chapter 9

Electrochemically Induced Oxidation of Acetic Acid by Molecular Oxygen on BDD

In the previous chapters, the electrochemical oxidation of acetic acid was investigated on BDD electrode and an indirect mechanism of its electrooxidation, mediated by hydroxyl radicals, was proposed. This chapter demonstrates that mineralization of acetic acid on BDD does not only involve hydroxyl radicals but also dissolved molecular oxygen. O_2 participates in mineralization processes during anodic polarization of BDD electrode in air/oxygen-saturated aqueous organic solutions. The direct evidence for that was found during electrooxidation of acetic acid saturated with isotopically labelled $^{18}O_2$ resulting in evolution of $C^{18}O_2$ and $C^{16}O^{18}O$. The oxidation of acetic acid by molecular oxygen was initiated probably by hydroxyl radicals formed on the electrode surface. Similar mechanism was reported in radiolysis of aqueous solutions of acetic acid.

This chapter is based on the following publication:

A. Kapałka, B. Lanova, H. Baltruschat, G. Fóti and C. Comninellis. Electrochemically induced mineralization of organics by molecular oxygen on boron-doped diamond electrode, *Electrochem. Comm.*, in press.

9.1 Introduction

The complete degradation of organic pollutants present in wastewater is usually achieved via thermally activated oxygen/air in wet air oxidation process (WAO) [112, 91, 113, 90]. This process occurs at high temperatures and pressures (300°C, 100 atm) and often gives small amount of acetic acid as a final product (Fig 9.1). WAO is initiated by formation of an organic radical R^\bullet during reaction between oxygen and the weakest C–H bond of the organic compound (Eq. 9.1) or during the reaction of the latter with HO_2^\bullet (Eq. 9.2).



R^\bullet reacts further with molecular oxygen to form peroxy radical, RO_2^\bullet (Eq. 2.28), which may react with organics (RH), typically by hydrogen abstraction (Eq. 2.29).



Similar reaction scheme to Eqs. 2.28–2.29 has been reported for radiolysis of organic aqueous solutions in the presence of dissolved oxygen [47, 114]. During this process, R^\bullet can be produced by the direct effect of the radiation on the RH (Eq. 2.24) or by interaction between RH and HO^\bullet (Eq. 2.25). The latter is formed during radiolysis of water, as shown in Eq. 2.26.



Thus, the key factors for the organics degradation via molecular oxygen is to: (i) ensure a good contact between oxygen and the organic matter to be oxidized [112] and (ii) supply sufficient energy to initiate the oxygen activation process, which results further in a chain of reactions.

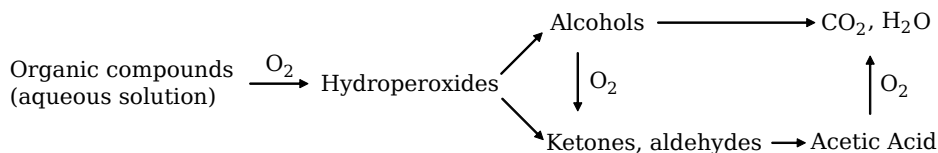


Figure 9.1. Simplified diagram for wet air oxidation [112].

In this chapter, the the role of molecular oxygen in the electrooxidation of aqueous solution of acetic acid is investigated on BDD electrode at ambient temperature. Several solutions of 50 mM CH_3COOH in 1 M HClO_4 have been studied: i) deaerated by argon, ii) aerated, iii) $^{16}\text{O}_2$ -saturated, and iv) $^{18}\text{O}_2$ -saturated. The products of the electrooxidation were studied by differential electrochemical mass spectrometry (DEMS). As a result, in parallel to faradaic current, the ionic current of $m/z = 32$ ($^{16}\text{O}_2$), $m/z = 34$ ($^{16}\text{O}^{18}\text{O}$), $m/z = 36$ ($^{18}\text{O}_2$), $m/z = 44$ (C^{16}O_2), $m/z = 46$ ($\text{C}^{16}\text{O}^{18}\text{O}$), and $m/z = 48$ (C^{18}O_2) were recorded. On the basis of obtained results, the mechanism of electrochemically induced oxidation of acetic by molecular oxygen on BDD electrode is proposed.

9.2 Experimental details

DEMS measurements were performed on BDD electrode in a dual thin layer electrochemical cell under constant flow of $5 \mu\text{l s}^{-1}$. All details concerning used electrodes and design of the cell are given in chapter 5, sec. 5.2. All measurements were performed at room temperature, in 1 M HClO_4 as a supporting electrolyte. The solutions of acetic acid were i) deaerated with argon, ii) aerated, iii) $^{16}\text{O}_2$ -saturated and iv) $^{18}\text{O}_2$ -saturated. The two latter were prepared by bubbling in the solution oxygen $^{16}\text{O}_2$ and isotopically labelled oxygen $^{18}\text{O}_2$, respectively, before (for 30 min) and during measurements.

The rate of O_2 consumption and CO_2 formation was calculated using following equation:

$$r = \frac{I_i}{K^*F} \quad (9.3)$$

where r (mol s^{-1}) is the rate, I_i (A) is the ionic current of O_2 and CO_2 , respectively, K^* is the calibration constant (sec. 5.2) for O_2 and CO_2 formation, equal to 5.9×10^{-6} and 8.1×10^{-6} ,

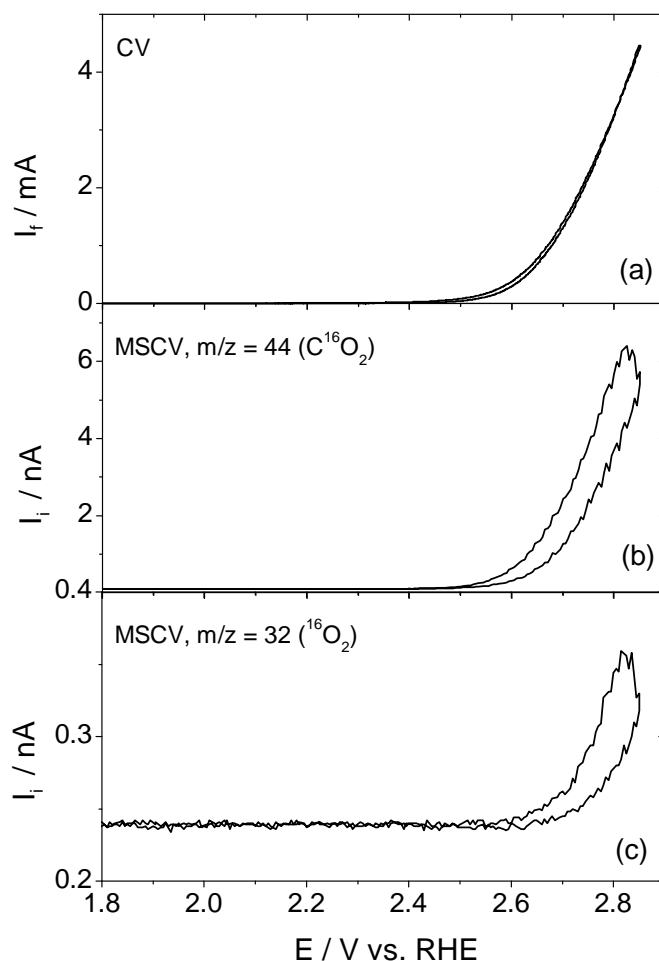


Figure 9.2. Simultaneously recorded the cyclic voltammogram (CV) (a) and the mass spectrometric CV (MSCV) for (b) C^{16}O_2 ($m/z = 44$) and (c) $^{16}\text{O}_2$ ($m/z = 32$) on BDD in deaerated solution of 50 mM CH_3COOH ; scan rate 10 mV s^{-1} , flow rate $5 \mu\text{l s}^{-1}$, electrolyte 1 M HClO_4 ; $T = 25^\circ\text{C}$.

respectively, and F (C mol^{-1}) is the Faraday constant.

9.3 Results

9.3.1 Electrooxidation of air/oxygen-saturated solution of acetic acid

Figure 9.2 shows the cyclic voltammogram CV and the mass spectrometric cyclic voltammograms (MSCV) of C^{16}O_2 and $^{16}\text{O}_2$ simultaneously recorded during oxidation of deaerated solution of 50 mM acetic acid. The oxidation of acetic acid starts at $\sim 2.45 \text{ V}$ vs. RHE resulting in an increase of the faradaic current (Fig. 9.2a) and the ionic current of C^{16}O_2 (Fig. 9.2b). The oxidation

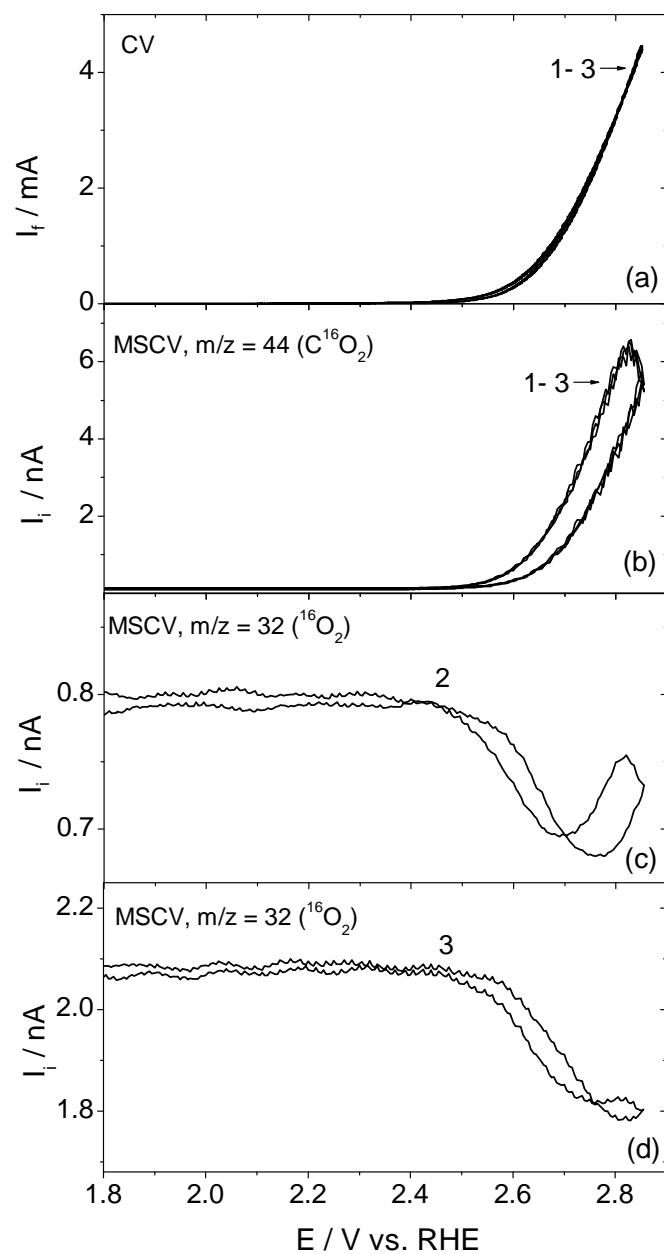


Figure 9.3. Comparison of the cyclic voltammograms (CV) (a) and the mass spectrometric CV (MSCV) for (b) C¹⁶O₂ (m/z = 44) recorded for 1) deaerated, 2) aerated, 3) ¹⁶O₂-saturated solution of 50 mM CH₃COOH on BDD electrode; (c) and (d) show simultaneously recorded MSCV of ¹⁶O₂ (m/z = 32) of 2) aerated, and 3) ¹⁶O₂-saturated solution, respectively; scan rate 10 mV s⁻¹, flow rate 5 μl s⁻¹, electrolyte 1 M HClO₄; T = 25°C.

proceeds simultaneously with oxygen evolution (Fig. 9.2c), which is a side reaction.

A similar experiment was performed for aerated and $^{16}\text{O}_2$ -saturated solution of acetic acid. The comparison of recorded CV's and MSCV's of C^{16}O_2 and $^{16}\text{O}_2$ is presented in Fig. 9.3. Seeing that the obtained voltammograms in Fig. 9.3a–b are superimposed, it can be concluded that neither faradaic current nor C^{16}O_2 evolution is influenced by dissolved oxygen in the solution. On the contrary, one can observe that ionic current of $^{16}\text{O}_2$ decreases in parallel to C^{16}O_2 evolution for both aerated (Fig. 9.3c) and $^{16}\text{O}_2$ -saturated solution (Fig. 9.3d). The rate of $^{16}\text{O}_2$ consumption, estimated from Eq. 9.3 at 2.80 V vs. RHE, is equal to $2.0 \times 10^{-10} \text{ mol s}^{-1}$ and $5.2 \times 10^{-10} \text{ mol s}^{-1}$ for aerated and $^{16}\text{O}_2$ -saturated solution, respectively.

9.3.2 Electrooxidation of acetic acid saturated with isotopically labelled $^{18}\text{O}_2$

The decrease of the ionic current of $^{16}\text{O}_2$ (Fig. 9.3c–d) indicates that molecular oxygen dissolved in the solution may participate in oxidation of acetic acid. To verify this hypothesis, the experiment with $^{18}\text{O}_2$ -saturated solution of acetic acid was performed. Figure 9.4a–c shows the comparison of the CV's and MSCV's of C^{16}O_2 and $^{18}\text{O}_2$ for both deaerated and $^{18}\text{O}_2$ -saturated solution of acetic acid. As previously, presence of $^{18}\text{O}_2$ in the solution does influence neither faradaic current nor C^{16}O_2 evolution (Fig. 9.4a and b, respectively). In parallel to C^{16}O_2 evolution, the ionic current of $^{18}\text{O}_2$ (Fig. 9.4c) decreases with increasing potential. The rate of $^{18}\text{O}_2$ consumption, estimated from Eq. 9.3 at 2.85 V vs. RHE, is equal to $6.2 \times 10^{-10} \text{ mol s}^{-1}$. The decrease of the ionic current is observed only in $^{18}\text{O}_2$ -saturated solution whereas for deaerated one, a non-significant ionic current of $^{18}\text{O}_2$ (max 3 pA) is measured that corresponds to electrochemically formed $^{18}\text{O}_2$ from natural water isotope H_2^{18}O . It is interesting to note that in parallel to decrease of $^{18}\text{O}_2$, the ionic current of $^{16}\text{O}^{18}\text{O}$ increases, in $^{18}\text{O}_2$ -saturated solution, reaching a limitation at higher potentials (Fig. 9.4d). The rate of $^{16}\text{O}^{18}\text{O}$ formation, estimated from Eq. 9.3 at 2.85 V vs. RHE, is equal to $9.5 \times 10^{-11} \text{ mol s}^{-1}$. The limiting current may indicate that formed $^{16}\text{O}^{18}\text{O}$ is limited by diffusion of $^{18}\text{O}_2$ to the electrode surface.

Figure 9.5a–b shows that isotopically labelled C^{18}O_2 and $\text{C}^{18}\text{O}^{16}\text{O}$ are evolved in parallel to $^{18}\text{O}_2$ diminution (Fig. 9.4c) confirming that oxygen dissolved in the solution is involved in oxidation of acetic acid. The rate of C^{18}O_2 and $\text{C}^{18}\text{O}^{16}\text{O}$ formation, estimated from Eq. 9.3 at 2.85 V vs. RHE, is equal to $3.3 \times 10^{-11} \text{ mol s}^{-1}$ and $5.6 \times 10^{-10} \text{ mol s}^{-1}$, respectively. The rate of $\text{C}^{18}\text{O}^{16}\text{O}$ is higher due to the higher probability of its formation since one atom of oxygen (^{16}O) comes from water. Seeing that rate of $\text{C}^{18}\text{O}^{16}\text{O}$ formation is similar to rate of $^{18}\text{O}_2$ consumption,

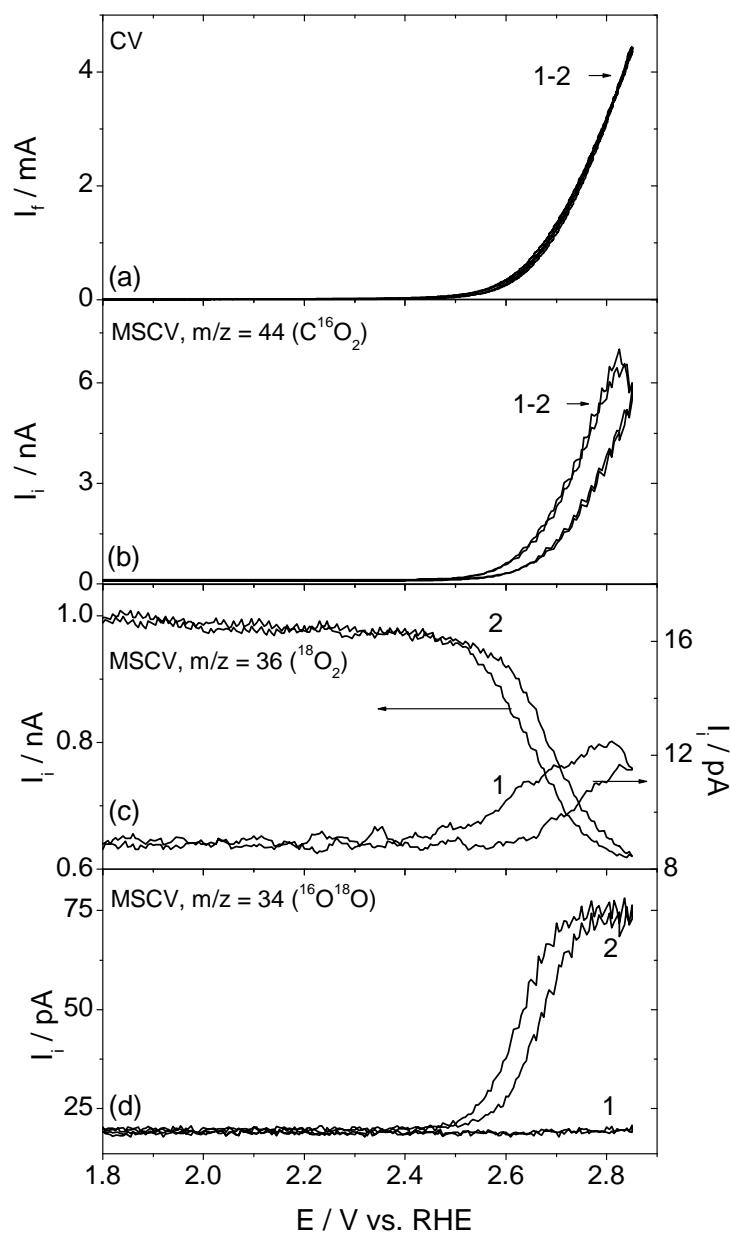


Figure 9.4. Simultaneously recorded the cyclic voltammograms (CV) (a) and the mass spectrometric CV (MSCV) for (b) $C^{16}O_2$ ($m/z = 44$), (c) $^{18}O_2$ ($m/z = 36$), and (d) $^{16}O^{18}O$ ($m/z = 34$) of 1) deaerated and 2) $^{18}O_2$ -saturated solution of 50 mM CH_3COOH ; scan rate 10 $mV s^{-1}$, flow rate 5 $\mu l s^{-1}$, electrolyte 1 M $HClO_4$, $T = 25^\circ C$.

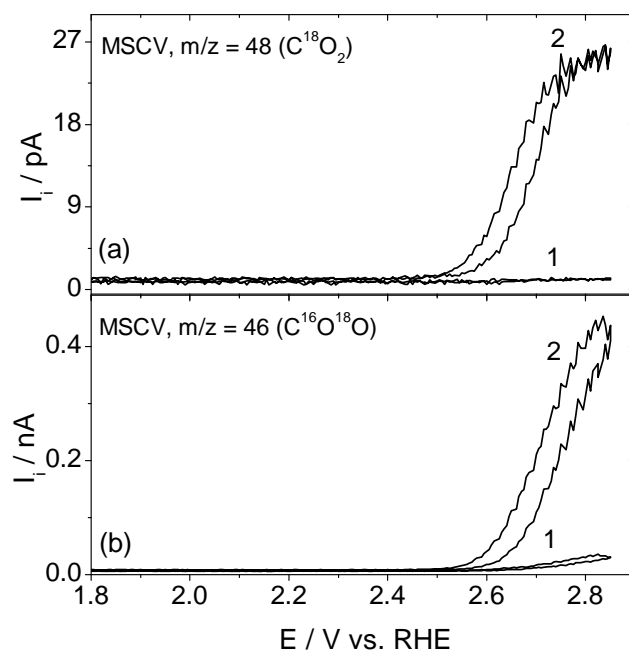


Figure 9.5. Simultaneously recorded the mass spectrometric CV (MSCV) for (a) $C^{18}O_2$ ($m/z = 48$), and (b) $C^{16}O^{18}O$ ($m/z = 46$) of 1) deaerated and 2) $^{18}O_2$ -saturated solution of 50 mM CH_3COOH ; experimental conditions as in Fig. 9.4.

it can be concluded that almost half of $^{18}O_2$ was trapped by intermediates formed during acetic acid oxidation. It is interesting to note that ionic current of $C^{18}O_2$, similar to $^{16}O^{18}O$ (Fig. 9.4d), reaches a limitation at higher potentials (Fig. 9.5a). The limiting current may indicate that oxidation of acetic acid by $^{18}O_2$ is also limited by diffusion of $^{18}O_2$ to the electrode surface.

Under investigated conditions, 7 % of additional, non-faradaic CO_2 was evolved.

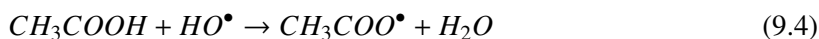
9.4 Discussion

The results presented above provide direct evidence that molecular oxygen can be used at room temperature for the mineralization of acetic acid after its activation on BDD electrode. This activation of the reaction with molecular oxygen proceeds most likely through the sequence of reactions that are initiated by HO^\bullet formed on the electrode surface.

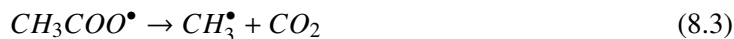
As discussed in section 9.1, during the ionizing irradiation of aqueous solution of organic compounds, molecular oxygen enhances the oxidation processes [47, 115, 116]. This occurs via addition of molecular oxygen to an organic free radical (R^\bullet) resulting in formation of an organic

peroxy radical RO_2^\bullet (Eq. 2.28), which can participate in subsequent reactions. Organic free radical (R^\bullet) is formed via dehydrogenation of hydrocarbons (RH) initiated by HO^\bullet formed during radiolysis of water (Eqs. 2.25–2.26). Therefore, we can make an analogy between radiation-induced oxidation of organic compounds and our system, in which HO^\bullet are generated electrochemically.

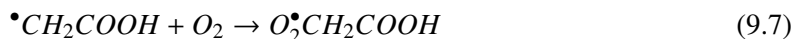
Adopting mechanism described above and considering the mechanism of acetic acid oxidation proposed in chapter 8, the reaction with oxygen initiated electrochemically on BDD electrode in presence of acetic acid may proceed via two parallel paths. In both cases, a starting point is the formation of HO^\bullet from water upon anodic polarization (Eq. 2.2). HO^\bullet abstract hydrogen from acetic acid yielding either acetoxyl radical (Eq. 9.4) or carboxymethyl radical (Eq. 9.5).



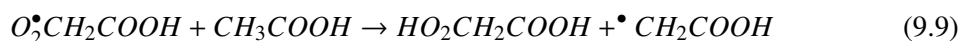
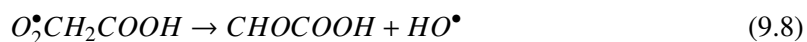
Considering reaction 9.4, acetoxyl radical can decompose to give methyl radical (Eq. 8.3) which can further react with molecular oxygen to form methylperoxy radical (Eq. 9.6). Evidence for reaction 9.6, at room temperature, has been given by Johnson and Weiss [114] in irradiated (by X-rays) aqueous methane solution in the presence of dissolved oxygen.



Considering reaction 9.5, carboxymethyl radical can directly react with molecular oxygen to form peroxy carboxymethyl radical (Eq. 9.7). Such reaction has been reported by Garrison et al. [115, 116] in irradiated (by γ -rays from Co^{60}), oxygen-saturated, aqueous solution of acetic acid.



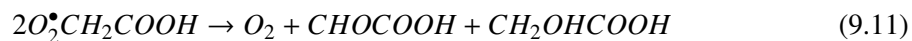
The authors suggested that formed $O_2^{\bullet}CH_2COOH$ may undergo various interactions [115], e.g., *i*) decompose to glyoxylic acid and hydroxyl radical (Eq. 9.8), *ii*) abstract hydrogen from acetic acid (Eq. 9.9), or *iii*) undergo hydrolysis (Eq. 9.10).



It is interesting to note, that two former reactions (Eq. 9.8 and 9.9) lead to regeneration of HO^{\bullet} and ${}^{\bullet}CH_2COOH$, whereas reaction 9.10 leads to formation of hydroperoxyl radical HO_2^{\bullet} . All these radical products participate further in chain reactions.

In our experiment, we have observed formation of a small amount of $^{16}O^{18}O$ during oxidation of acetic acid in $^{18}O_2$ -saturated solution (Fig. 9.4d). Formation of this product gives an evidence that HO^{\bullet} is regenerated or HO_2^{\bullet} is formed during oxidation processes since both of them, besides reacting with organic compounds, may also participate in oxygen evolution, a secondary reaction. The exact mechanism for $^{16}O^{18}O$ evolution can not be concluded from the experimental results, however, we might consider 2 possible reaction paths: *i*) $H^{18}O^{\bullet}$ reacts with either $H^{16}O^{\bullet}$ or $H_2^{16}O$ to form $^{16}O^{18}O$, or *ii*) $H^{16}O^{18}O^{\bullet}$ decomposes to $^{16}O^{18}O$.

According to Garrison et al. [115], peroxy carboxymethyl radical can also undergo disproportionation reaction to give oxygen, glyoxylic and glycolic acid (Eq. 9.11), or hydrogen abstraction (Eq. 9.12) followed by isomerization (Eq. 9.13).



The latter reaction (Eq. 9.13) leads to formation of oxalic acid. In fact, oxalic acid was found as intermediate formed during acetic acid oxidation on BDD electrodes [95]. It has also been

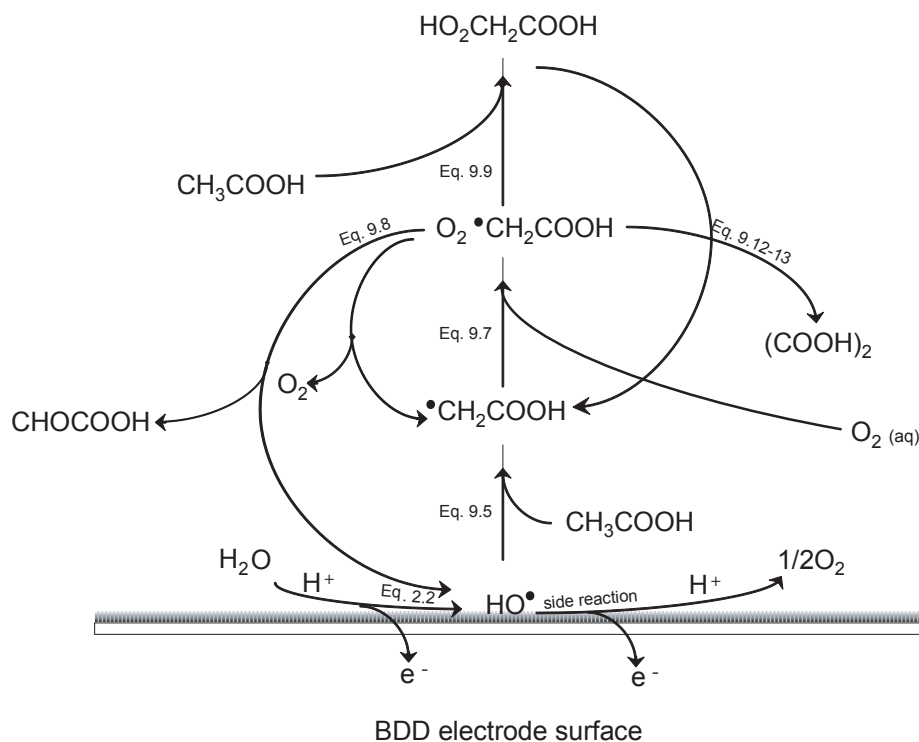


Figure 9.6. Diagram for electrochemically induced oxidation of acetic acid via molecular oxygen dissolved in solution on boron-doped diamond electrode. The diagram is constructed based on reactions: 2.2, 9.5, 9.7, 9.8, 9.9, 9.12, and 9.13.

reported that oxalic acid can be easily oxidized to carbon dioxide and water on BDD via hydroxyl radicals [83], what might contribute to formation of isotopically labelled $C^{18}O_2$ in Fig. 9.5.

Based on reactions 2.2–9.13 and considering that oxidation of acetic acid occurs through parallel reactions in which $O_2^{\bullet}CH_2COOH$ is a main intermediate, the scheme of chain reactions initiated by HO^{\bullet} can be proposed, as shown in Fig. 9.6. By analogy to radiolysis, we might consider that similar reaction scheme is valid for other organic compounds. Thus, based on our experimental results and literature, a general model of electrochemically induced oxidation of organic compounds via molecular oxygen on BDD electrode can be proposed, as given in Fig. 9.7. In this simplified diagram, reactions (6) reflects the stability of peroxy radical RO_2^{\bullet} which is a key factor of an efficient mineralization of organic compounds.

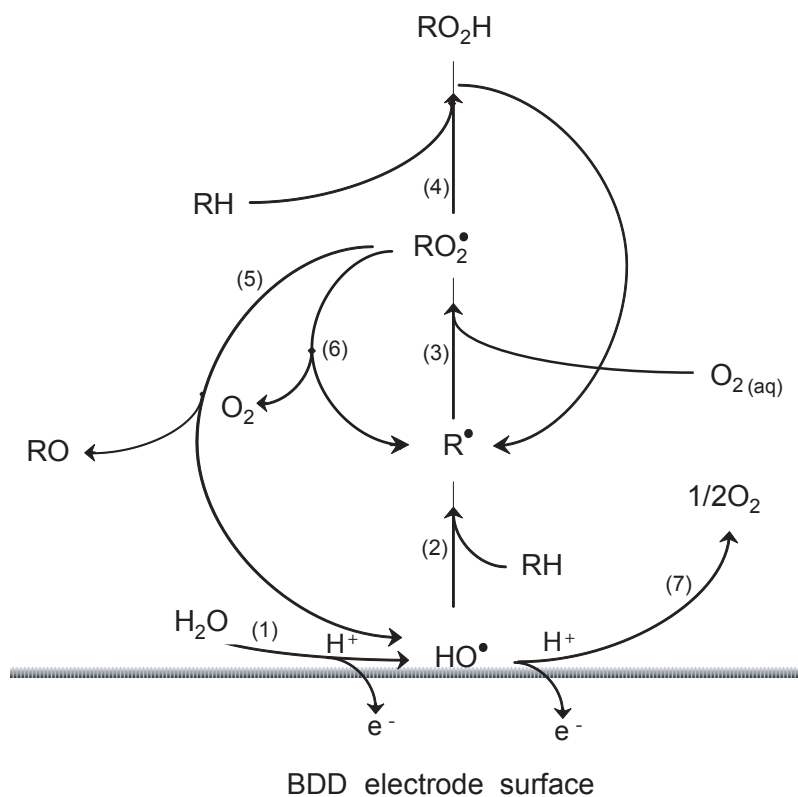


Figure 9.7. Simplified diagram for electrochemically induced oxidation of organic compounds via molecular oxygen dissolved in solution on boron-doped diamond electrode; (1) water discharge to hydroxyl radical HO^\bullet ; (2) dehydrogenation of organic compound, RH via HO^\bullet and formation of free organic radical R^\bullet ; (3) addition of molecular oxygen to an organic free radical R^\bullet resulting in formation of an organic peroxy radical RO_2^\bullet ; (4) dehydrogenation of RH via RO_2^\bullet resulting in formation of organic hydroperoxide $ROOH$ and regeneration of R^\bullet ; (5) decomposition of RO_2^\bullet leading to regeneration of HO^\bullet and formation of RO^\bullet ; (6) decomposition of RO_2^\bullet to R^\bullet ; (7) oxygen evolution, a side reaction.

9.5 Conclusions

The results presented in this chapter show that molecular oxygen dissolved in aqueous solution contributes to the degradation of acetic acid on BDD electrodes in ambient temperature. This non-faradaic enhancement of the acetic acid electrooxidation is initiated by HO^\bullet formed during water discharge on the electrode surface. By analogy to radiolysis, we may consider that similar processes occur in presence of other organic compounds. In fact, this opens the possibilities for designing a less energy consuming electrochemical mineralization process in which current is applied mainly to initiate formation of HO^\bullet whereas complete degradation of pollutant proceeds via reaction with molecular oxygen in air-saturated solutions. To do so, it is necessary to ensure an

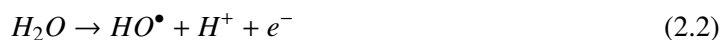
efficient transport of molecular O₂ to the interface and thus the organic radicals in order to avoid their polymerization. The key factors of the efficient mineralization process are the stability of organic radicals (lifetime) and its reactivity toward molecular oxygen dissolved in solution.

Chapter 10

General Discussion

This chapter summarizes the most important results obtained in this thesis regarding the oxygen evolution reaction and oxidation of organic compounds on boron-doped diamond electrodes. This short review focuses on mechanism of the electrooxidation processes and emphasizes the key role of hydroxyl radicals and molecular oxygen in degradation of organic compounds.

On boron-doped diamond (BDD) electrodes, the onset potential for oxygen evolution reaction (OER) is about 2.3 V vs. SHE. Although very high, as compared with other conventional electrode materials, this potential corresponds to a thermodynamic potential of formation of free hydroxyl radicals (2.38 V vs. SHE) in acid aqueous solution (see sec. 3.1.2). Indeed, Marselli et al. [29] have detected hydroxyl radicals on a BDD electrode, by means of spin trapping, during electrolysis of 1 M HClO₄. The fact that O₂ is evolved close to the thermodynamic potential of HO• formation (and at potentials positive of it) allows to assume that quasi free hydroxyl radicals are electrogenerated during water discharge on the BDD surface (Eq. 2.2). This assumption is justifiable, taking into account the inert nature of diamond surface, which contains closely packed sp³ carbon atoms [19].



Reaction 2.2 can be considered as a rate determining step of oxygen evolution reaction due to the fact that the Tafel slope of 120 mV dec⁻¹ and zero reaction order was found for OER on BDD (see sec. 4.3.1.2 and 4.3.4). The Tafel slope of 120 mV dec⁻¹ was determined on both BDD microelectrodes-array (MEA) and BDD macroelectrode in the potential region above 2.4 V. In order to obtain the Tafel slope of 120 mV dec⁻¹ on BDD macroelectrode, an appropriate correction for the ohmic drop (taking into account the total uncompensated resistance of the studied system) was necessary (see sec. 4.3.1.2). In fact, water discharge to hydroxyl radicals has already been assumed to be a rate determining step of OER on BDD, although abnormally high Tafel slope for OER on BDD (between 220 and 415 mV dec⁻¹) has been reported so far in the literature [16, 17, 18].

To sum up, oxygen evolution on BDD occurs at a high overpotential with respect to the thermodynamic potential for O₂ formation ($E_{OER}^\circ = 1.23$ V vs. SHE), but very close to the thermodynamic potential of HO• formation ($E_{HO^\bullet}^\circ = 2.38$ V vs. SHE).

Considering that free hydroxyl radicals mediate the oxidation processes on the BDD surface, it is possible to estimate the change in the onset potential of HO• formation (ΔE) during organics oxidation, with respect to that for oxygen evolution (see sec. 3.3). ΔE can be determined assuming that water discharge to hydroxyl radicals (Eq. 2.2) on BDD is governed by Nernst equation

(Eq. 3.25).

$$\Delta E = \frac{RT}{zF} \ln \frac{c_{HO_R}^s}{c_{HO_{OER}}^s} \quad (3.25)$$

By inserting in Eq. 3.25 the surface concentration of hydroxyl radicals during organics oxidation ($c_{HO_R}^s$) and oxygen evolution ($c_{HO_{OER}}^s$), estimated using one-dimensional Fick law (see sec. 3.2), one obtains the shift of potential, ΔE , in the negative direction, i.e., toward lower potentials. This change in the onset potential of HO^\bullet formation, during organics oxidation, should result in a shift of the current-potential ($I-V$) curves with respect to that for oxygen evolution. Indeed, experimental results show that, during oxidation of methanol and formic acid, $I-V$ curves shift to the lower potentials as organics concentration increases (see sec. 5.3.1). Furthermore, ΔE evaluated experimentally agrees with that estimated by Eq. 3.25 (see sec. 5.4). Similar to C-1 organic compounds, oxidation of other organics (e.g., oxalic acid, ethanol, i-propanol [31]) results in a shift of the $I-V$ curves in a negative direction, what supports the mechanism proposed in this work.

DEMS and voltammetric study of the anodic oxidation of C-1 organic compounds confirmed that their oxidation on BDD is a fast reaction, whereas water discharge to hydroxyl radicals remains a rate determining step. In the presence of organics, oxygen evolution is a secondary reaction and proceeds once the limiting current for organics oxidation is attained. As a consequence, oxygen evolution shifts toward higher potentials (see chapter 5). These conclusions are in agreement with a previous work performed in our group [50, 31].

Contrary to most of organic compounds, during acetic acid oxidation on BDD, $I-V$ curves shift to higher potentials with increasing concentration (above a critical value) of acetic acid. In other words, for a given potential, current density decreases (see sec. 7.3.1). This phenomenon can be explained by an adsorption of acetic acid on BDD surface causing an auto-inhibition of its oxidation (see sec. 7.4). This auto-inhibition effect was found to be reversible with respect to concentration, suggesting rather weak interactions between acetic acid and the electrode surface (no chemical bond formation). Moreover, acetic acid appeared to be an inhibitor not only for its own oxidation but also for that of other compounds (formic acid, Ce^{3+}) that undergo oxidation at high anodic potentials, i.e., close to the oxygen evolution reaction.

Adsorption of acetic acid on BDD probably results in the displacement of water from the electrode surface, reducing the rate of water discharge to hydroxyl radicals. In fact, analysis of Tafel slope indicated that at high acetic acid concentrations there is a competition between the indirect

oxidation of acetic acid via hydroxyl radicals and the inhibition of water discharge reaction. As a consequence, the Tafel slope increased up to 240 mV dec^{-1} at 500 mM acetic acid (see sec. 7.4 and 7.3.2). Furthermore, DEMS analysis showed that although both current and CO_2 formation rate decreases with acetic acid concentration, the rate of formation of intermediates (methanol, ethane, and methylacetate) increases. This indicates that at the highest acetic acid concentrations the formation rate of hydroxyl radicals is too slow and oxidation is largely incomplete (see sec. 8.3.3). Thus, the elimination of water from the electrode surface in presence of acetic acid and decrease of water discharge rate could explain the auto-inhibition of acetic acid oxidation.

In fact, adsorption of acetic acid on BDD is rather astonishing in the light of an inert character of the diamond surface, well known from the lack of adsorption sites [19]. In the literature, it has been reported that oxidation of phenolic compounds cause deactivation of BDD surface in the region of water stability [32, 30]. This phenomenon, however, is due to a deposition of the adhesive polymeric material during oxidation process. In order to restore the initial activity of electrode, it is necessary to apply high anodic potentials at which the polymeric film can be oxidized by hydroxyl radicals. Recently, Weiss et al. [83] have reported that maleic acid blocks its own oxidation at potentials close to that of the water discharge. Furthermore, they observed that oxidation of formic and oxalic acid is inhibited in presence of maleic acid. The authors have explained this phenomenon by adsorption of maleic acid that is oxidized by a direct electron transfer.

It is interesting to see that oxidation of acetic acid involves not only hydroxyl radicals but also molecular oxygen dissolved in the solution (see chapter 9). Direct evidence for that was found during oxidation of acetic acid solution saturated with isotopically labelled oxygen $^{18}\text{O}_2$. As a result, C^{18}O_2 and $\text{C}^{16}\text{O}^{18}\text{O}$ was evolved, proving that molecular oxygen participates in the mineralization process. By analogy to radiolysis / photolysis [45, 47], oxidation of acetic acid by molecular oxygen on BDD was initiated probably by electrogenerated hydroxyl radicals, which react with acetic acid to form organic free radicals R^\bullet ($^\bullet\text{CH}_2\text{COOH}$ or CH_3^\bullet). According to literature, in aerated solution, R^\bullet can react with molecular oxygen to form peroxy radical, as given by Eq. 2.28.



Thus, in our case formation of $^{18}\text{O}_2^\bullet\text{CH}_2\text{COOH}$ and $\text{CH}_3^\bullet^{18}\text{O}_2$ is probable. Organic peroxy radicals are very reactive and can initiate subsequent chain reactions leading, via several possible

intermediates, to complete oxidation of organic compounds (see sec. 9.4).

To the best of our knowledge, electrochemically induced mineralization of organic compounds via reaction with molecular oxygen, at room temperature, has not been yet reported in the literature. In fact, this non-faradaic enhancement of the electrooxidation processes opens the possibilities for designing a less energy consuming degradation of organic pollutants on BDD anodes. Ideally, current would be supplied mainly to initiate formation of HO^\bullet whereas complete mineralization of organics would proceed via reaction with molecular oxygen in aerated solution.

Chapter 11

Perspectives

In order to decrease the cost of the electrochemical treatment of organic pollutants on BDD, it is necessary to: (i) search for alternative methods of preparation of diamond electrodes, (ii) improve the electrochemically induced mineralization of organics by molecular oxygen dissolved in aerated aqueous solutions, and (iii) understand the mechanism of organics adsorption on diamond surface in order to avoid the electrode surface blockage, which limits the efficient wastewater treatment. This chapter focuses on these three aspects, showing some directions for the future developments and investigations.

This chapter is based on the following publication:

A. Ciecwa, R. Wuthrich and C. Comninellis. Electrochemical characterization of mechanically implanted boron-doped diamond electrodes, *Electrochem. Comm.*, 8 (2006) 375

11.1 Mechanically implanted MI-BDD electrodes

In this section, a new, low production cost technique for the preparation of boron-doped diamond electrodes is presented and the electrochemical behavior of these electrodes is studied. This technique is based on mechanical implantation of BDD particles into a titanium substrate. The electrochemical characterization of low coverage mechanically implanted boron doped diamond electrodes (LC-MI-BDD) is performed using the ferri-ferrocyanide $\text{Fe}(\text{CN})_6^{4-/3-}$ redox couple and compared with the Si/ BDD thin-films electrodes deposited on *p*-Si by the hot-filament chemical vapor deposition technique (CVD). It is shown that the electrochemical response of low coverage electrodes (LC-MI-BDD) is different from that of Si/BDD (CVD), revealing rather microelectrodes behavior. Thus, taking all advantageous of microelectrodes behavior, these electrodes can be applied for wastewater treatment or electrolysis.

11.1.1 Introduction

BDD thin-film electrodes, deposited on an appropriate substrate (*p*-Si, Ti, Nb, Ta, Mo, W) by chemical vapor deposition (CVD) are the most widely studied and well reported in literature. Two main techniques have been used for the CVD deposition; the hot-filament chemical vapor deposition and the microwave-assisted plasma-enhanced chemical vapor deposition [15, 21]. Although these electrodes have shown excellent electrochemical performances, they have some limitations, mainly due to the complexity of the preparation procedure of the BDD films (900°C in the presence of large excess of hydrogen).

Recently, a new preparation mode for BDD electrodes, so-called mechanically implanted boron doped diamond electrodes (MI-BDD), has been proposed for electrolysis with application in wastewater treatment and electrosynthesis [117]. In this process, boron doped diamond crystals are firstly prepared then mechanically implanted into a titanium substrate and finally an electrically non-conducting silicon based coating is applied in order to cover the space between the diamond crystals (Fig. 11.1) [117]. The main advantages of this technique are:

- low production cost due to the fact that the preparation of diamond crystals is already a relatively cheap high volume technology [118],
- easy preparation of large surfaces (order of square meters)

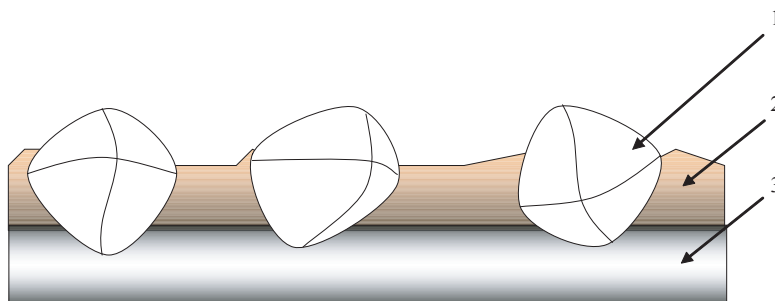


Figure 11.1. Schematic representation of the mechanically implanted boron-doped diamond electrode (MI-BDD); (1) boron-doped diamond crystals, (2) non-conducting silicon based coating, (3) titanium substrate [117].

- avoids problems inherent to the CVD deposition technique at 900°C in presence of excess hydrogen (hydrogen embrittlement, phase transformation of the substrate, formation of non diamond impurities at the grain boundaries of the coating, formation of carbides at the substrate coating interface, difference in the thermal expansion coefficient between the substrate and the coating)
- possibility to control the surface density of diamond crystals for an optimal utilization of diamond particles.

11.1.2 Preparation of the mechanically implanted MI-BDD electrodes

The implanted boron doped diamond electrodes have been synthesized at Pro Aqua GmbH, Niklasdorf, Austria. The conductive diamond particles (doping level of boron 3×10^{20} at cm^{-3}), with a particles size in the range from 100 to 150 μm , have been prepared by the high temperature high pressure technique [117].

The titanium substrate, before implantation, has been treated in boiling oxalic acid solution (10%) for 30 min in order to increase the surface roughness and to eliminate the surface oxide layer (TiO_2). The diamond particles have been implanted on the pre-treated Ti substrate by rolling. All spaces between the diamonds particles were filled with electrical non-conductive silicon based coating Tyranno coat ST-100 Standard (Fig. 11.1). Finally the electrodes were heated in argon atmosphere during 30 minutes at 350°C and polished mechanically by a grinding machine until

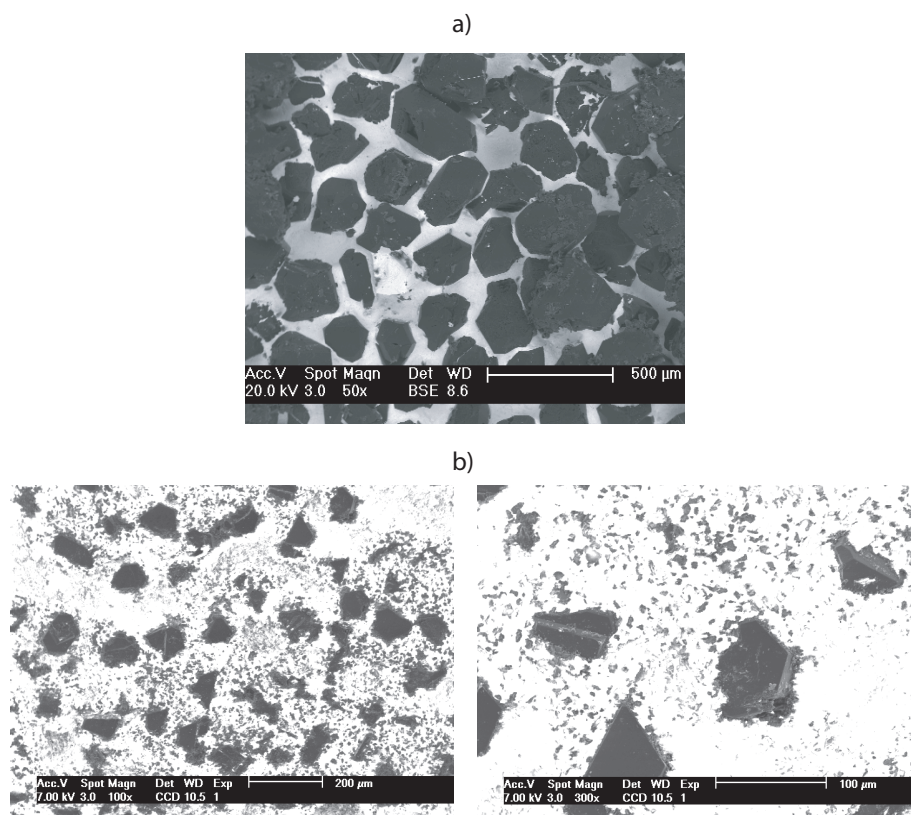


Figure 11.2. SEM micrographs of: (a) high coverage mechanically implanted boron-doped diamond electrodes (HC-MI-BDD); (b) low coverage mechanically implanted boron-doped diamond electrodes (LC-MI-BDD).

the tops of the diamonds were visible. Figure 11.2a–b shows SEM micrograph for both high (HC-MI-BDD) and low coverage (LC-MI-BDD) mechanically implanted boron doped diamond electrodes, respectively.

In this section, the low coverage mechanically implanted electrodes (LC-MI-BDD) will be investigated (Fig 11.2b). The estimated fractional coverage of the LC-MI-BDD obtained from Fig. 11.2b is $25 \pm 5\%$. Since the diamond particles are randomly dispersed and irregularly shaped, the average distance between particles (d) and the average size of the exposed diamond particles (equivalent dimension R) can be approximated only with a big deviation. The center to center separation d of particles was found to be $120 \pm 25 \mu\text{m}$ while the equivalent dimension R was estimated to $70 \pm 15 \mu\text{m}$. Furthermore, diamond particles exhibit a big discrepancy of the orientation. As it is shown in Fig. 11.3 various diamond crystal planes are exposed above the isolation coating. In consequence of the random dispersion, non-uniform shape and diverse orientation of the diamond

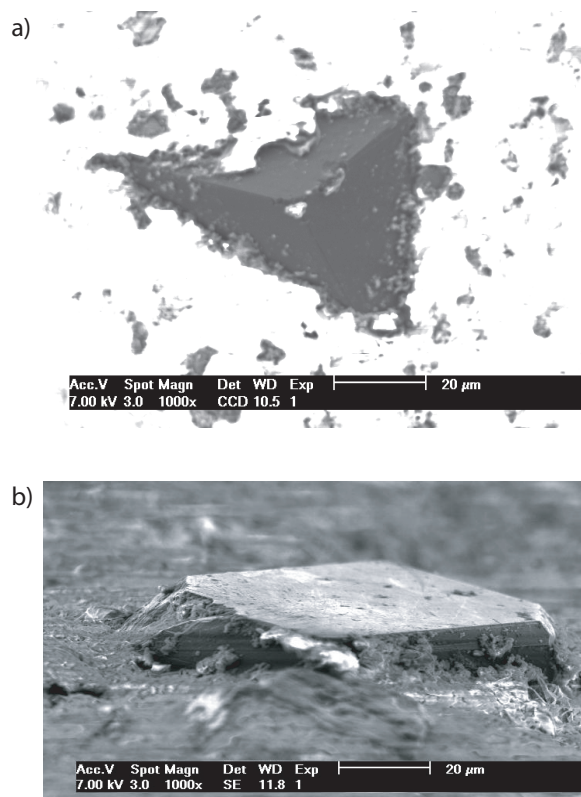


Figure 11.3. SEM micrographs of the individual particles in the low coverage mechanically implanted boron-doped diamond electrodes (LC-MI-BDD). Micrographs (a) and (b) show different orientation of diamond grains.

particles, LC-MI-BDD electrodes are characterized by a high heterogeneity.

11.1.3 Electrochemical characterization of LC-MI-BDD electrode

Figure 11.4a shows cyclic voltammograms (CV) of the $\text{Fe}(\text{CN})_6^{4-/3-}$ redox couple on boron doped diamond thin film electrodes, Si/BDD, obtained at different scan rates ($5\text{--}300\text{ mV s}^{-1}$). As previously reported by many authors, well defined peaks (anodic and cathodic) are obtained for the investigated couple [119]. Furthermore, the current peak varies linearly with the square root of the scan rate (Fig. 11.4b). Supposing a quasi-reversible system for the $\text{Fe}(\text{CN})_6^{4-/3-}$ couple, the diffusion coefficient $\text{Fe}(\text{CN})_6^{4-}$ was calculated using Eq. 11.1 to be $7.6 \times 10^{-6}\text{ cm}^2\text{ s}^{-1}$ which agrees with the literature [120] ($7.35 \times 10^{-6}\text{ cm}^2\text{ s}^{-1}$).

$$I_p = (2.69 \times 10^5) z^{3/2} A c D^{1/2} \nu^{1/2} \quad (11.1)$$

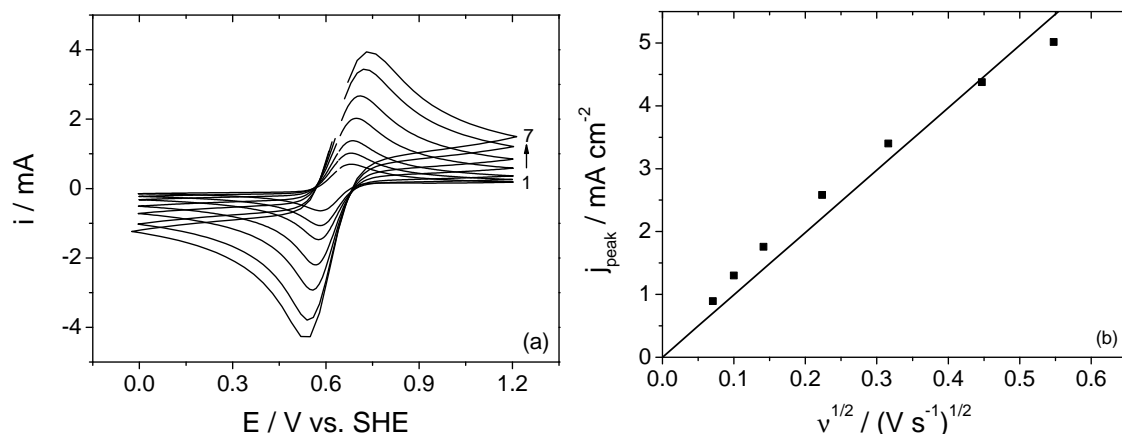


Figure 11.4. (a) Cyclic voltammograms of the Fe(CN)_6^{4-} redox couple recorded at Si/BDD electrode at scan rates: (1) 5, (2) 10, (3) 20, (4) 50, (5) 100, (6) 200, (7) 300 mV s^{-1} ; concentration of Fe(CN)_6^{4-} : 12.5 mM; $T = 25^\circ\text{C}$; (b) corresponding current peak density (related to geometric area of the electrode: 0.785 cm^2) vs. square root of the scan rate.

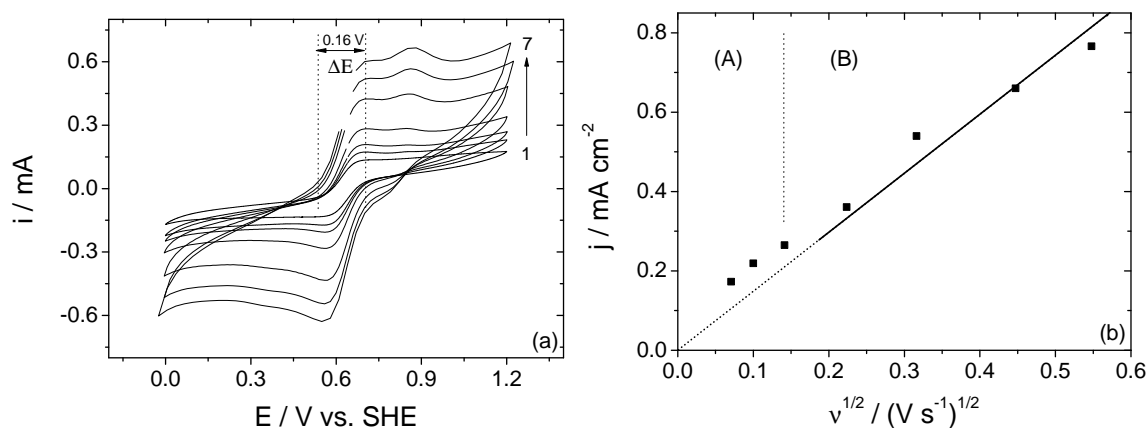


Figure 11.5. (a) Cyclic voltammograms of the Fe(CN)_6^{4-} redox couple recorded at LC-MI-BDD electrode at scan rates: (1) 5, (2) 10, (3) 20, (4) 50, (5) 100, (6) 200, (7) 300 mV s^{-1} ; concentration of Fe(CN)_6^{4-} : 12.5 mM; $T = 25^\circ\text{C}$; (b) corresponding current peak density (related to geometric area of the electrode: 0.785 cm^2) vs. square root of the scan rate; (A) spherical diffusion with partial overlap, (B) linear diffusion.

where I_p (A) is the current peak, z is the number of electrons involved in the reaction ($z = 1$), A (cm^2) is the working electrode surface, c (mol cm^{-3}) is the concentration, D (cm^2s^{-1}) is the diffusion coefficient, and v (V s^{-1}) is the scan rate.

Figure 11.5a shows cyclic voltammograms of the $\text{Fe(CN)}_6^{4-/3-}$ redox couple obtained on low coverage mechanically implanted boron doped diamond electrodes (LC-MI-BDD) performed at the same scan rates as for Si/BDD electrodes. Recorded CV of the mechanically implanted electrode are significantly different compared to the CV obtained using thin film electrodes. The main differences between these electrodes are:

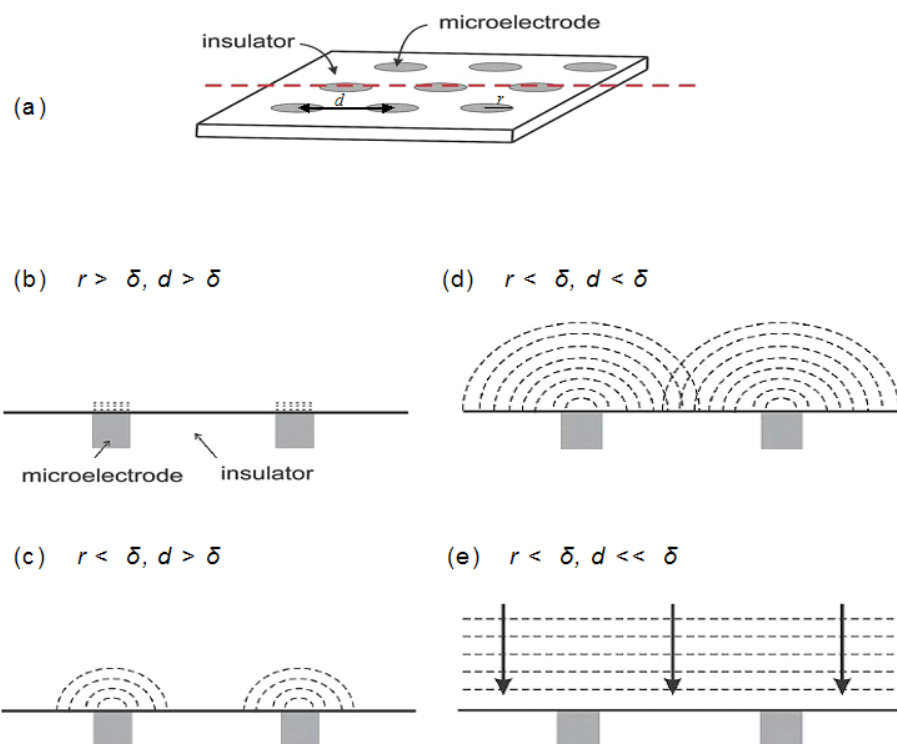


Figure 11.6. (a) Schematic representation of the microelectrodes-array; d is the distance between microelectrodes in the array; r is the radius of the single microelectrode, δ is the thickness of the diffusion layer; (b)–(e) diffusion profiles at the microelectrodes-array: linear diffusion (b), non-linear diffusion (c), non-linear diffusion with partial overlap (d), heavily overlapping diffusion layers resulting in linear diffusion (e) [121].

- under similar conditions the measured currents are much smaller than those obtained using p -Si/BDD electrodes,
- at low scan rates ($< 50 \text{ mV s}^{-1}$) there is no evidence for peak formation, in fact a plateau is rather formed (limiting current) indicating a steady-state tendency,
- at relatively high scan rates ($> 100 \text{ mV s}^{-1}$) a multiplicity of peaks seems to be appeared,
- the limiting (or the peak current) varies linearly with the square root of scan rate only at high scan rates (Fig. 11.5b) however, at low scan rate there is a strong deviation from linearity.

11.1.4 Discussion

Such an unusual behaviour of the LC-MI-BDD electrodes can be explained in the light of the microelectrode theory. Considering that each diamond particle of LC-MI-BDD electrode acts as a single microelectrode, one can shift from the macro-electrode (linear diffusion) standpoint to

Table 11.1. Estimated parameters of LC-MI-BDD; δ is the thickness of diffusion layer; R is the equivalent particle dimension equal to $70 \pm 15 \mu\text{m}$; d is the average distance between BDD particles equal to $120 \pm 25 \mu\text{m}$.

Scan rate mV s^{-1}	5	10	20	50	100	200	300
$\delta / \mu\text{m}$	217	153	108	69	48	34	28
$\frac{R}{\delta}$	0.32 ± 0.07	0.5 ± 0.1	0.6 ± 0.1	1.0 ± 0.2	1.5 ± 0.3	2.0 ± 0.4	2.5 ± 0.5
$\frac{d}{\delta}$	0.5 ± 0.1	0.8 ± 0.2	1.1 ± 0.2	1.7 ± 0.4	2.5 ± 0.5	3.5 ± 0.7	4.3 ± 0.9

the random microelectrodes-arrays one. According to Bard [67], there is no exact definition of microelectrode. It is said that, when the electrode is smaller than the scale of developed diffusion layer, we can consider it as a microelectrode. In case of microelectrodes-array, the voltammetric response depends on the two key factors [121, 122, 123]. First is the radius of the individual microelectrodes r versus the size of the diffusion layer thickness δ and the second is the size of the diffusion layer thickness δ versus the distance between the individual microelectrodes d . Depending on these factors, different diffusion profiles can be observed at microelectrodes-array (Fig. 11.6) [121, 122].

Cyclic voltammetry is a powerful technique and can allow the modification of the diffusion layer thickness δ by a simple modification of the scan rate (Eq. 11.2) [121]:

$$\delta = \sqrt{2D \frac{\Delta E}{\nu}} \quad (11.2)$$

where ΔE is the potential difference between the onset oxidation potential and the potential of limiting current (or current peak) appearance as it is shown in Fig. 11.5a.

Considering the average size of the exposed diamond particles in LC-MI-BDD electrode (equivalent dimension R), in Table 11.1 the diffusion thickness δ and the ratio R/δ and d/δ are given as a function of potential scan rate. From this table it is clear that at low scan rates ($< 20 \text{ mV s}^{-1}$) the equivalent particle dimension R is smaller than the size of the diffusion layer thickness δ ($R < \delta$) and the average distance between particles is almost the same as the diffusion layer thickness δ ($R < \delta$ and $d \sim \delta$). Under these conditions, spherical diffusion dominates mass transport and the average distance between particles d is close to the diffusion layer thickness δ . Therefore, there is an overlap of adjacent diffusion layers of individual particles (microelectrodes). This can explain the scan rate dependence of the limiting current observed at low scan rates (Fig. 11.5b (A)). Table 11.1 shows also that at high scan rates ($> 50 \text{ mV s}^{-1}$) both the equivalent particle dimension R and the average distance between particles d are larger than the size of the

diffusion layer thickness δ ($R > \delta$ and $d > \delta$). Under these conditions linear diffusion dominates mass transport and the area of the overall diffusion field is the sum of the geometric areas of the individual particles (microelectrodes). This can explain the linear dependency between the peak current and the square root of scan rate (Fig. 11.5b (B)). Observed voltammetry characteristics can be associated with category (d) and (b) of diffusion profile (Fig. 11.6).

The presence of the linear diffusion still does not explain why multiple peaks appear. In order to clarify such behavior, the heterogeneous nature of LC-MI-BDD has to be taken into account. In fact, these electrodes can exhibit diverse local electrochemical activity due to the inhomogeneity of the surface (crystallographic orientation, doping level and dimension of the diamond particles) leading to domains with different electrochemical reaction rates. As a consequence, the multiplicity of the peaks is very likely. Therefore, possible explanation of apparent quasi-steady performance of voltammograms at short time scales can be the presence of several but less pronounced peaks. As at high scan rates linear diffusion dominates the mass transport and the area of the overall diffusion is the sum of the geometric areas of the individual microelectrodes, comparison of the voltammetric response of *p*-Si/BDD and LC-MI-BDD electrodes can allow the estimation of the fractional coverage of the diamond surface of LC-MI-BDD electrodes. In fact, from Fig. 11.4b and 11.5b, where the current peak density (related to geometric area 0.785 cm²) as a function of square root of the scan rate for both *p*-Si/BDD and LC-MI-BDD electrodes is given, the fractional coverage can be estimated from the ratio between the two slopes in the domain of high scan rates ($> 50 \text{ mV s}^{-1}$). The calculated coverage of the diamond phase was found to be 16%, what gives similar value as obtained from the SEM micrograph analysis (25%).

11.1.5 Conclusions

In this section, a new technique of BDD electrodes preparation based on mechanical implantation of BDD particles into a titanium substrate is presented. The electrochemical response of low coverage mechanically implanted BDD (LC-MI-BDD) was found to be similar to the microelectrodes-array one. Taking into account all advantages of microelectrodes, attractive electrodes for electrolysis with application in wastewater treatment or electrosynthesis can be obtained by this method. These preliminary results encourage for further studies on mechanically implanted boron doped diamond electrodes. By controlling the dimension of the diamond crystals and the average spacing, in a very simple and cheap way the optimized electrodes can be fabricated for a big scale application.

11.2 Electrochemically induced activation of molecular oxygen

As discussed in chapter 9, molecular oxygen dissolved in aerated aqueous solution contributes to the degradation of acetic acid on boron-doped diamond electrode at ambient temperature. It has been shown that under investigated conditions, 7% of additional, non-faradaic CO_2 was evolved. The efficiency of this non-faradaic contribution to electrooxidation of organics on BDD can be certainly improved by ensuring an efficient transport of molecular oxygen to the electrode surface. A possible solution that can be implemented to enhance transport of O_2 to the interface is to supply an oxygen via a porous electrode.

Future investigations should also provide better understanding of the mechanism of chain reactions that are initiated by hydroxyl radical and organic peroxy radicals. Therefore, it is necessary to carry out experiments in aerated / oxygen saturated aqueous solutions of various organic compounds in order to detect formed intermediates. To do so, two techniques are suggested: Differential Electrochemical Mass Spectrometry (DEMS) and the Fourier Transform Infrared Spectroscopy (FTIR).

11.3 Study of adsorption process on BDD surface

As shown in chapters 7 and 8, acetic acid adsorbs on the BDD surface inhibiting both its own oxidation and that of other compounds that oxidize at high anodic potentials. Further investigations are necessary to elucidate the adsorption mechanism of acetic acid on diamond. It would be interesting to compare oxidation of acetic acid on both hydrogen and oxygen terminated diamond surface in order to find out whether the surface termination of diamond has an effect on the adsorption process. Moreover, oxidation of various organic compounds should be performed in order to identify compounds (classes of compounds) which are prone to adsorption on diamond surface.

The understanding of the the adsorption mechanism of the organic compounds on BDD can be helpful in avoiding the anode surface blockage, which limits the efficient wastewater treatment.

References

- [1] M. A. Q. Alfaro, S. Ferro, C. A. Martinez-Huitle, and Y. M. Vong, "Boron doped diamond electrode for the wastewater treatment," *Journal of the Brazilian Chemical Society*, vol. 17, pp. 227–236, 2006.
- [2] R. Tenne and C. Levy-Clement, "Diamond electrodes," *Israel Journal of Chemistry*, vol. 38, pp. 57–73, 1998.
- [3] Y. V. Pleskov, "Synthetic diamond in electrochemistry," *Russian Chemical Reviews*, vol. 68, pp. 381–392, 1999.
- [4] Y. V. Pleskov, A. Y. Sakharova, M. D. Krotova, L. L. Builov, and B. V. Spitsyn, "Photoelectrochemical properties of semiconductor diamond," *Journal of Electroanalytical Chemistry and Interfacial Electrochemistry*, vol. 228, pp. 19–27, 1987.
- [5] K. Serrano, P. A. Michaud, C. Comninellis, and A. Savall, "Electrochemical preparation of peroxodisulfuric acid using boron doped diamond thin film electrodes," *Electrochimica Acta*, vol. 48, no. 4, pp. 431–436, 2002.
- [6] F. Beck, W. Kaiser, and H. Krohn, "Boron doped diamond (BDD)-layers on titanium substrates as electrodes in applied electrochemistry," *Electrochimica Acta*, vol. 45, no. 28, pp. 4691–4695, 2000.
- [7] M. Panizza, P. A. Michaud, G. Cerisola, and C. Comninellis, "Electrochemical treatment of wastewaters containing organic pollutants on boron-doped diamond electrodes: Prediction of specific energy consumption and required electrode area," *Electrochemistry Communications*, vol. 3, no. 7, pp. 336–339, 2001.

- [8] A. Morao, A. Lopes, M. T. Pessoa de Amorim, and I. C. Goncalves, "Degradation of mixtures of phenols using boron doped diamond electrodes for wastewater treatment," *Electrochimica Acta*, vol. 49, no. 9-10, pp. 1587–1595, 2004.
- [9] R. Bellagamba, P. A. Michaud, C. Comninellis, and N. Vatistas, "Electro-combustion of polyacrylates with boron-doped diamond anodes," *Electrochemistry Communications*, vol. 4, no. 2, pp. 171–176, 2002.
- [10] P. Rychen, L. Pupunat, W. Haenni, and E. Santoli, "Water treatment applications with BDD [boron-doped diamond electrodes and the diacell concept]," *New Diamond and Frontier Carbon Technology*, vol. 13, pp. 109–117, 2003.
- [11] G. M. Swain, "Electroanalytical applications of diamond electrodes," *Semiconductors and Semimetals*, vol. 77, pp. 121–148, 2004.
- [12] A. Fujishima, C. Terashima, K. Honda, B. V. Sarada, and T. N. Rao, "Recent progress in electroanalytical applications of diamond electrodes," *New Diamond and Frontier Carbon Technology*, vol. 12, pp. 73–81, 2002.
- [13] Y. Einaga, R. Sato, H. Olivia, D. Shin, T. Ivandini, and A. Fujishima, "Modified diamond electrodes for electrolysis and electroanalysis applications," *Electrochimica Acta*, vol. 49, no. 22-23, pp. 3989–3995, 2004.
- [14] P.-A. Michaud, E. Mahe, W. Haenni, A. Perret, and C. Comninellis, "Preparation of peroxodisulfuric acid using boron-doped diamond thin film electrodes," *Electrochemical and Solid-State Letters*, vol. 3, pp. 77–79, 2000.
- [15] A. Perret, W. Haenni, N. Skinner, X. M. Tang, D. Gandini, C. Comninellis, B. Correa, and G. Foti, "Electrochemical behavior of synthetic diamond thin film electrodes," *Diamond and Related Materials*, vol. 8, no. 2-5, pp. 820–823, 1999.
- [16] M. H. Santana, L. A. D. Faria, and J. F. Boodts, "Electrochemical characterisation and oxygen evolution at a heavily boron doped diamond electrode," *Electrochimica Acta*, vol. 50, no. 10, pp. 2017–2027, 2005.
- [17] F. Beck, H. Krohn, W. Kaiser, M. Fryda, C. P. Klages, and L. Schafer, "Boron doped diamond/titanium composite electrodes for electrochemical gas generation from aqueous electrolytes," *Electrochimica Acta*, vol. 44, no. 2-3, pp. 525–532, 1998.

- [18] N. Katsuki, E. Takahashi, M. Toyoda, T. Kurosu, M. Iida, S. Wakita, Y. Nishiki, and T. Shimamune, "Water electrolysis using diamond thin-film electrodes.," *Journal of the Electrochemical Society*, vol. 145, pp. 2358–2362, 1998.
- [19] A. Fujishima, *Diamond Electrochemistry*. BKC INC Tokyo, 2005.
- [20] J. van de Lagemaat, D. Vanmaekelbergh, and J. J. Kelly, "Electrochemistry of homoepitaxial cvd diamond. energetics and electrode kinetics in aqueous electrolytes," *Journal of Electroanalytical Chemistry*, vol. 475, pp. 39–151, 1999.
- [21] T. Tsubota, T. Fukui, T. Saito, K. Kusakabe, S. Morooka, and H. Maeda, "Surface morphology and electrical properties of boron-doped diamond films synthesized by microwave-assisted chemical vapor deposition using trimethylboron on diamond (100) substrate," *Diamond and Related Materials*, vol. 9, no. 7, pp. 1362–1368, 2000.
- [22] P.-A. Michaud, *Comportement anodique du diamant synthétique dopé au bore*. PhD thesis, EPFL, No 2595, 2002.
- [23] S. Ferro, "Synthesis of diamond," *Journal of Materials Chemistry*, vol. 12, pp. 2843–2855, 2002.
- [24] R. Kalish, "Doping of diamond," *Carbon*, vol. 37, pp. 781–785, 1999.
- [25] C. Levy-Clement, "Semiconducting and metallic boron-doped diamond electrodes," in *Diamond Electrochemistry*, pp. 80–114, Amsterdam: Elsevier Science, 2005.
- [26] H. Notsu, I. Yagi, T. Tatsuma, D. A. Tryk, and A. Fujishima, "Surface carbonyl groups on oxidized diamond electrodes," *Journal of Electroanalytical Chemistry*, vol. 492, pp. 31–37, 2000.
- [27] H. Notsu, I. Yagi, T. Tatsuma, D. A. Tryk, and A. Fujishima, "Introduction of oxygen-containing functional groups onto diamond electrode surfaces by oxygen plasma and anodic polarization," *Electrochemical and Solid-State Letters*, vol. 2, pp. 522–524, 1999.
- [28] S. Ferro, M. Dal Colle, and A. De Battisti, "Chemical surface characterization of electrochemically and thermally oxidized boron-doped diamond film electrodes," *Carbon*, vol. 43, no. 6, pp. 1191–1203, 2005.

- [29] B. Marselli, J. Garcia-Gomez, P.-A. Michaud, M. A. Rodrigo, and C. Comninellis, "Electrogeneration of hydroxyl radicals on boron-doped diamond electrodes," *Journal of The Electrochemical Society*, vol. 150, no. 3, pp. D79–D83, 2003.
- [30] W. Haenni, P. Rychen, M. Fryda, and C. Comninellis, "Industrial applications of diamond electrodes," *Semiconductors and Semimetals*, vol. 77, pp. 149–196, 2004.
- [31] G. Foti and C. Comninellis, "Electrochemical oxidation of organics on iridium oxide and synthetic diamond based electrodes," *Modern aspects of electrochemistry*, vol. 37, pp. 86–129, 2004.
- [32] J. Iniesta, P. A. Michaud, M. Panizza, G. Cerisola, A. Aldaz, and C. Comninellis, "Electrochemical oxidation of phenol at boron-doped diamond electrode," *Electrochimica Acta*, vol. 46, no. 23, pp. 3573–3578, 2001.
- [33] G. Foti, D. Gandini, and C. Comninellis, "Anodic oxidation of organics on thermally prepared oxide electrodes.," *Current Topics in Electrochemistry*, vol. 5, pp. 71–91, 1997.
- [34] S. Fierro, T. Nagel, H. Baltruschat, and C. Comninellis, "Investigation of the oxygen evolution reaction on Ti/IrO₂ electrodes using isotope labelling and on-line mass spectrometry," *Electrochemistry Communications*, vol. 9, no. 8, pp. 1969–1974, 2007.
- [35] S. Fierro, T. Nagel, H. Baltruschat, and C. Comninellis, "Investigation of formic acid oxidation on Ti/IrO₂ electrodes using isotope labelling and on-line mass spectrometry," *Electrochemical and Solid-State Letters*, vol. 11, no. 7, pp. E20–E23, 2008.
- [36] H. Baltruschat, "Differential electrochemical mass spectrometry," *Journal of the American Society for Mass Spectrometry*, vol. 15, no. 12, pp. 1693–1706, 2004.
- [37] B. Bittins-Cattaneo, E. Cattaneo, P. Koenigshoven, and W. Vielstich, "New developments in electrochemical mass spectroscopy," *Electroanalytical Chemistry*, vol. 17, pp. 181–220, 1990.
- [38] H. Baltruschat, "Differential electrochemical mass spectrometry as a tool for interfacial studies.," in *Interfacial Electrochemistry: Theory, Experiment, and Applications.*, Marcel Dekker, 1999.

- [39] S. Bruckenstein and R. R. Gadde, "Use of a porous electrode for in situ mass spectrometric determination of volatile electrode reaction products," *Journal of the American Chemical Society*, vol. 93, no. 3, pp. 793–794, 1971.
- [40] O. Wolter and J. Heitbaum, "Differential electrochemical mass spectroscopy (DEMS) - a new method for the study of electrode processes.," *Berichte der Bunsen-Gesellschaft*, vol. 88, pp. 2–6, 1984.
- [41] G. Henrici-Olive and S. Olive, "Activation of molecular oxygen," *Angewandte Chemie*, vol. 86, pp. 1–12, 1974.
- [42] M. Tarr and F. Samson, eds., *Oxygen Free Radicals in Tissue Damage*. Birkhauser Boston, 1993.
- [43] E. F. Elstner, "Oxygen activation and oxygen toxicity," *Annual Review of Plant Physiology*, vol. 33, pp. 73–96, 1982.
- [44] R. S. Drago, "Activation of molecular oxygen by transition metal complexes," *Studies in Surface Science and Catalysis*, vol. 66, pp. 83–91, 1991.
- [45] O. Legrini, E. Oliveros, and A. M. Braun, "Photochemical processes for water treatment," *Chemical Reviews*, vol. 93, pp. 671–98, 1993.
- [46] Y. Du, M. Zhou, and L. Lei, "The role of oxygen in the degradation of p-chlorophenol by Fenton system," *Journal of Hazardous Materials*, vol. 139, pp. 108–115, 2007.
- [47] G. Scholes and J. Weiss, "Oxygen effects and formation of peroxides in aqueous solutions," *Radiation Research Supplement*, vol. 1, pp. 177–189, 1959.
- [48] J. H. Raley, L. M. Porter, F. F. Rust, and W. E. Vaughan, "The oxidation of free methyl radicals.," *Journal of the American Chemical Society*, vol. 73, pp. 15–17, 1951.
- [49] L. I. Kartasheva, V. N. Chulkov, O. A. Didenko, and A. K. Pikaev, "Hydrogen peroxide yields in the radiolysis of aerated aqueous solutions of formic acid," *High Energy Chemistry*, vol. 34, no. 6, pp. 409–411, 2000.
- [50] C. Comninellis, I. Duo, P.-A. Michaud, B. Marselli, and S.-M. Park, "Application of synthetic boron-doped diamond electrodes in electrooxidation processes," in *Diamond Electrochemistry*, pp. 449–476, Amsterdam: Elsevier Science, 2005.

- [51] R. Parsons, *Standard Potentials in Aqueous Solution*. Marcel Dekker INC., 1985.
- [52] J. Hoare, *Standard Potentials in Aqueous Solution*. Marcel Dekker INC., 1985.
- [53] A. B. Anderson, "Theory at the electrochemical interface: reversible potentials and potential-dependent activation energies," *Electrochimica Acta*, vol. 48, no. 25-26, pp. 3743–3749, 2003.
- [54] P. Ruetschi and P. Delahay, "Influence of electrode material on oxygen overvoltage: A theoretical analysis," *The Journal of Chemical Physics*, vol. 23, no. 3, pp. 556–560, 1955.
- [55] A. B. Anderson, N. M. Neshev, R. A. Sidik, and P. Shiller, "Mechanism for the electrooxidation of water to OH and O bonded to platinum: quantum chemical theory," *Electrochimica Acta*, vol. 47, no. 18, pp. 2999–3008, 2002.
- [56] H. Yang and J. L. Whitten, "The adsorption of water and hydroxyl on Ni(III)," *Surface Science*, vol. 223, no. 1-2, pp. 131–150, 1989.
- [57] C. Qin and J. Whitten, "Adsorption of O, H, OH, and H₂O on Ag(100)," *Journal of Physical Chemistry B*, vol. 109, no. 18, pp. 8852–8856, 2005.
- [58] T. E. Shubina and M. T. Koper, "Co-adsorption of water and hydroxyl on a Pt₂Ru surface," *Electrochemistry Communications*, vol. 8, no. 5, pp. 703–706, 2006.
- [59] Y. Cao and Z.-X. Chen, "Theoretical studies on the adsorption and decomposition of H₂O on Pd(1 1 1) surface," *Surface Science*, vol. 600, no. 19, pp. 4572–4583, 2006.
- [60] P.-A. Michaud, M. Panizza, L. Ouattara, T. Diaco, G. Foti, and C. Comninellis, "Electrochemical oxidation of water on synthetic boron-doped diamond thin film anodes," *Journal of Applied Electrochemistry*, vol. 33, no. 2, pp. 151–154, 2003.
- [61] "The radiation chemistry data center. <http://allen.rad.nd.edu/>."
- [62] L. J. J. Janssen and M. H. A. Blijlevens, "Electrochemical oxidation of iodate to periodate," *Electrochimica Acta*, vol. 48, no. 25-26, pp. 3959–3964, 2003.
- [63] M. Panizza and G. Cerisola, "Influence of anode material on the electrochemical oxidation of 2-naphthol: Part 1. Cyclic voltammetry and potential step experiments," *Electrochimica Acta*, vol. 48, no. 23, pp. 3491–3497, 2003.

- [64] H. Vogt and R. Balzer, "The bubble coverage of gas-evolving electrodes in stagnant electrolytes," *Electrochimica Acta*, vol. 50, no. 10, pp. 2073–2079, 2005.
- [65] J. Eigeldinger and H. Vogt, "The bubble coverage of gas-evolving electrodes in a flowing electrolyte," *Electrochimica Acta*, vol. 45, no. 27, pp. 4449–4456, 2000.
- [66] S. Alehashem, F. Chambers, J. W. Strojek, G. M. Swain, and R. Ramesham, "Cyclic voltammetric studies of charge transfer reactions at highly boron-doped polycrystalline diamond thin-film electrodes," *Analytical Chemistry*, vol. 67, no. 17, pp. 2812–2821, 1995.
- [67] A. J. Bard and L. R. Faulkner, *Electrochemical methods : fundamentals and applications*. New York, N.Y. : Wiley, 1980.
- [68] D. M. Shub and M. F. Reznik, "Method for estimating ohmic errors and correcting the polarization curves of metal-oxide anodes.," *Elektrokhimiya*, vol. 21, pp. 937–941, 1985.
- [69] N. Krstajic and S. Trasatti, "Cathodic behavior of RuO₂-doped Ni/Co₃O₄ electrodes in alkaline solutions: hydrogen evolution.," *Journal of Applied Electrochemistry*, vol. 28, pp. 1291–1297, 1998.
- [70] L. A. De Faria, J. F. C. Boodts, and S. Trasatti, "Electrocatalytic properties of ternary oxide mixtures of composition Ru_{0.3}Ti(0.7-x)Ce_xO₂: oxygen evolution from acidic solution.," *Journal of Applied Electrochemistry*, vol. 26, pp. 1195–1199, 1996.
- [71] T. Erdey-Grúz, *Kinetics of electrode processes*. London:Hilger, 1972.
- [72] J. Koryta, J. Dvorák, and L. Kavan, *Principles of electrochemistry*. 2nd ed. - Chichester : Wiley, 1993.
- [73] L. Nylen and A. Cornell, "Critical anode potential in the chlorate process," *Journal of The Electrochemical Society*, vol. 153, no. 1, pp. D14–D20, 2006.
- [74] J. O. Bockris and A. K. Reddy, *Modern electrochemistry*. New York : Plenum Press, 1970.
- [75] T. Kondo, K. Honda, D. A. Tryk, and A. Fujishima, "AC impedance studies of anodically treated polycrystalline and homoepitaxial boron-doped diamond electrodes," *Electrochimica Acta*, vol. 48, no. 19, pp. 2739–2748, 2003.

- [76] A. Damjanovic, A. Dey, and J. O. Bockris, "Kinetics of oxygen evolution and dissolution on platinum electrodes," *Electrochimica Acta*, vol. 11, no. 7, pp. 791–814, 1966.
- [77] L. M. Da Silva, J. F. C. Boodts, and L. A. De Faria, "Oxygen evolution at $\text{RuO}_2(x)+\text{Co}_3\text{O}_4(1-x)$ electrodes from acid solution," *Electrochimica Acta*, vol. 46, no. 9, pp. 1369–1375, 2001.
- [78] M. C. Tavares, S. A. S. Machado, and L. H. Mazo, "Study of hydrogen evolution reaction in acid medium on Pt microelectrodes," *Electrochimica Acta*, vol. 46, no. 28, pp. 4359–4369, 2001.
- [79] B. El Roustom, *Préparation et caractérisation de nanoparticules bimétalliques (Pt-Au) sur un substrat en diamant dopé au bore : application à l'électrocatalyse*. PhD thesis, EPFL, No 3624, 2006.
- [80] H. B. Martin, A. Argoitia, J. C. Angus, and U. Landau, "Voltammetry studies of single-crystal and polycrystalline diamond electrodes," *Journal of The Electrochemical Society*, vol. 146, no. 8, pp. 2959–2964, 1999.
- [81] I. Duo, A. Fujishima, and C. Comninellis, "Electron transfer kinetics on composite diamond (sp^3)-graphite (sp^2) electrodes," *Electrochemistry Communications*, vol. 5, no. 8, pp. 695–700, 2003.
- [82] P. Canizares, J. Garcia-Gomez, J. Lobato, and M. A. Rodrigo, "Electrochemical oxidation of aqueous carboxylic acid wastes using diamond thin-film electrodes.," *Industrial & Engineering Chemistry Research*, vol. 42(5), pp. 956–962, 2003.
- [83] E. Weiss, K. Groenen-Serrano, A. Savall, and C. Comninellis, "A kinetic study of the electrochemical oxidation of maleic acid on boron doped diamond.," *Journal of Applied Electrochemistry*, vol. 37(1), pp. 41–47, 2007.
- [84] J.-F. Zhi, H.-B. Wang, T. Nakashima, T. N. Rao, and A. Fujishima, "Electrochemical incineration of organic pollutants on boron-doped diamond electrode. Evidence for direct electrochemical oxidation pathway.," *Journal of Physical Chemistry B*, vol. 107(48), pp. 13389–13395, 2003.

- [85] M. Panizza, P. A. Michaud, G. Cerisola, and C. Comninellis, "Anodic oxidation of 2-naphthol at boron-doped diamond electrodes," *Journal of Electroanalytical Chemistry*, vol. 507, no. 1-2, pp. 206–214, 2001.
- [86] C.-H. Chen and T.-K. Yeh, "A mathematical model for simulating methanol permeation and the mixed potential effect in a direct methanol fuel cell," *Journal of Power Sources*, vol. 160, no. 2, pp. 1131–1141, 2006.
- [87] J. G. Liu, G. S. Luo, S. Pan, and J. D. Wang, "Diffusion coefficients of carboxylic acids in mixed solvents of water and 1-butanol," *Chemical Engineering and Processing*, vol. 43, no. 1, pp. 43–47, 2004.
- [88] J. Willsau, O. Wolter, and J. Heitbaum, "On the nature of the adsorbate during methanol oxidation at platinum : A DEMS study," *Journal of Electroanalytical Chemistry*, vol. 185, no. 1, pp. 163–170, 1985.
- [89] H. Wang, C. Wingender, H. Baltruschat, M. Lopez, and M. T. Reetz, "Methanol oxidation on Pt, PtRu, and colloidal Pt electrocatalysts: a DEMS study of product formation," *Journal of Electroanalytical Chemistry*, vol. 509, no. 2, pp. 163–169, 2001.
- [90] R. Shende and J. Levec, "Wet oxidation kinetics of refractory low molecular mass carboxylic acids," *Industrial & Engineering Chemistry Research*, vol. 38, no. 10, pp. 3830–3837, 1999.
- [91] P. Gallezot, S. Chaumet, A. Perrard, and P. Isnard, "Catalytic wet air oxidation of acetic acid on carbon-supported ruthenium catalysts," *Journal of Catalysis*, vol. 168, no. 1, pp. 104–109, 1997.
- [92] L. Oliviero, J. Barbier, D. Duprez, H. Wahyu, J. W. Ponton, I. S. Metcalfe, and D. Mantzavinos, "Wet air oxidation of aqueous solutions of maleic acid over Ru/CeO₂ catalysts," *Applied Catalysis B: Environmental*, vol. 35, no. 1, pp. 1–12, 2001.
- [93] P. Canizares, J. Lobato, R. Paz, M. Rodrigo, and C. Saez, "Electrochemical oxidation of phenolic wastes with boron-doped diamond anodes," *Water Research*, vol. 39, no. 12, pp. 2687–2703, 2005.

- [94] E. Brillas, M. A. Banos, M. Skoumal, P. L. Cabot, J. A. Garrido, and R. M. Rodriguez, "Degradation of the herbicide 2,4-DP by anodic oxidation, electro-Fenton and photoelectro-Fenton using platinum and boron-doped diamond anodes," *Chemosphere*, vol. 68, no. 2, pp. 199–209, 2007.
- [95] D. Gandini, M. E., P. A. Michaud, W. Haenni, A. Perret, and C. Comninellis, "Oxidation of carboxylic acids at boron-doped diamond electrodes for wastewater treatment.," *Journal of Applied Electrochemistry*, vol. 30(12), pp. 1345–1350, 2000.
- [96] J. D. Wadhawan, F. J. Del Campo, R. G. Compton, J. S. Foord, F. Marken, S. D. Bull, S. G. Davies, D. J. Walton, and S. Ryley, "Emulsion electrosynthesis in the presence of power ultrasound biphasic Kolbe coupling processes at platinum and boron-doped diamond electrodes," *Journal of Electroanalytical Chemistry*, vol. 507, no. 1-2, pp. 135–143, 2001.
- [97] Y. Tian, X. Chen, C. Shang, and G. Chen, "Active and stable Ti/Si/BDD anodes for electro-oxidation," *Journal of The Electrochemical Society*, vol. 153, no. 7, pp. J80–J85, 2006.
- [98] Y. B. Vassiliev and V. A. Grinberg, "Adsorption kinetics of electrode processes and the mechanism of Kolbe electrosynthesis : Part I. Adsorption of carboxylic acids and the nature of the particles chemisorbed on platinum electrodes," *Journal of Electroanalytical Chemistry*, vol. 283, no. 1-2, pp. 359–378, 1990.
- [99] Y. B. Vassiliev and V. A. Grinberg, "Adsorption kinetics of electrode processes and the mechanism of Kolbe electrosynthesis : Part III. Mechanism of the process," *Journal of Electroanalytical Chemistry*, vol. 308, no. 1-2, pp. 1–16, 1991.
- [100] Y. B. Vassiliev and V. A. Grinberg, "Adsorption kinetics of electrode processes and the mechanism of Kolbe electrosynthesis : Part II: The role of adsorption in processes taking place during electrolysis of carboxylic acid salts," *Journal of Electroanalytical Chemistry*, vol. 336, no. 1-2, pp. 281–307, 1992.
- [101] A. Wieckowski, J. Sobrowski, P. Zelenay, and K. Franaszczuk, "Adsorption of acetic acid on platinum, gold and rhodium electrodes," *Electrochimica Acta*, vol. 26, no. 8, pp. 1111–1119, 1981.

- [102] E. K. Krauskopf and A. Wieckowski, "Acetic acid adsorption on smooth pt electrodes : Measuring the rate of double-layer organization and rearrangement," *Journal of Electroanalytical Chemistry*, vol. 271, no. 1-2, pp. 295–304, 1989.
- [103] Y. Maeda, K. Sato, R. Ramaraj, T. N. Rao, D. A. Tryk, and A. Fujishima, "The electrochemical response of highly boron-doped conductive diamond electrodes to Ce³⁺ ions in aqueous solution," *Electrochimica Acta*, vol. 44, no. 20, pp. 3441–3449, 1999.
- [104] E. Wadsworth, F. R. Duke, and C. A. Goetz, "Present status of cerium(IV)-cerium(III) potentials.," *Analytical Chemistry*, vol. 29, pp. 1824–5, 1957.
- [105] H. Kolbe *Memoirs and Proceedings of the Chemical Society*, vol. 3, p. 378, 1848.
- [106] A. K. Vijh and B. E. Conway, "Electrode kinetic aspects of the Kolbe reaction," *Chemical Reviews*, vol. 67, no. 6, pp. 623–664, 1967.
- [107] T. Dickinson and W. F. K. Wynne-Jones, "Mechanism of Kolbe's electrosynthesis. Part 1. Anode potential phenomena," *Transactions of the Faraday Society*, vol. 58, p. 382, 1962.
- [108] T. Dickinson and W. F. K. Wynne-Jones, "Mechanism of Kolbe's electrosynthesis. Part 2. Charging curve phenomena," *Transactions of the Faraday Society*, vol. 58, p. 388, 1962.
- [109] T. Dickinson and W. F. K. Wynne-Jones, "Mechanism of Kolbe's electrosynthesis. Part 3. Theoretical discussion," *Transactions of the Faraday Society*, vol. 58, p. 400, 1962.
- [110] C. Sequeira, D. Santos, and P. Brito, "Mediated and non-mediated electrochemical oxidation of isopropanol," *Applied Surface Science*, vol. 252, no. 17, pp. 6093–6096, 2006.
- [111] R. Bussar, *Einfluss der Stufendekoration auf dieReaktivität von Platineinkristallen*. PhD thesis, Universität Bonn, 2002, p. 100.
- [112] H. Debellefontaine and J. N. Foussard, "Wet air oxidation for the treatment of industrial wastes. Chemical aspects, reactor design and industrial applications in Europe," *Waste Management*, vol. 20, no. 1, pp. 15–25, 2000.
- [113] R. Serikawa, M. Isaka, Q. Su, T. Usui, T. Nishimura, H. Sato, and S. Hamada, "Wet electrolytic oxidation of organic pollutants in wastewater treatment," *Journal of Applied Electrochemistry*, vol. 30, no. 7, pp. 875–883, 2000.

- [114] G. Johnson and J. Weiss, "The formation of methyl hydroperoxide from methane irradiated by X-rays (200 kv.) in aqueous solution in the presence of dissolved oxygen.," *Chemistry and Industry*, pp. 358–359, 1955.
- [115] W. M. Garrison, H. R. Haymond, W. Bennett, and S. Cole, "Radiation-induced oxidation of aqueous acetic acid-oxygen solutions," *Radiation Research*, vol. 10, no. 3, pp. 273–282, 1959.
- [116] V. M. Garrison, H. R. Haymond, and B. M. Weeks, "Some effects of heavy-particle irradiation of aqueous acetic acid," *Radiation Research*, vol. 1, no. 1, pp. 97–108, 1954.
- [117] W. Wesner, M. Kotschan, R. Hermann, W. Staber, and M. Schelch, Vol. EP1527212, 2004.
- [118] O. Semchinova, D. Uffmann, H. Neff, and E. P. Smirnov, "Growth, preparation and surface modification of microcrystalline diamond powder for the synthesis of diamond ceramics," *Journal of the European Ceramic Society*, vol. 16, no. 7, pp. 753–758, 1996.
- [119] S. Ferro and A. De Battisti, "Electron transfer reactions at conductive diamond electrodes," *Electrochimica Acta*, vol. 47, no. 10, pp. 1641–1649, 2002.
- [120] C. Hodgman, *Handbook of Chemistry and Physics*. Chemical Rubber Publ. Co., Cleveland, 1944.
- [121] T. J. Davies and R. G. Compton, "The cyclic and linear sweep voltammetry of regular and random arrays of microdisc electrodes: Theory," *Journal of Electroanalytical Chemistry*, vol. 585, no. 1, pp. 63–82, 2005.
- [122] T. J. Davies, R. R. Moore, C. E. Banks, and R. G. Compton, "The cyclic voltammetric response of electrochemically heterogeneous surfaces," *Journal of Electroanalytical Chemistry*, vol. 574, no. 1, pp. 123–152, 2004.
- [123] K. Soh, W. Kang, J. Davidson, S. Basu, Y. Wong, D. Cliffl, A. Bonds, and G. Swain, "Diamond-derived microelectrodes array for electrochemical analysis," *Diamond and Related Materials*, vol. 13, no. 11-12, pp. 2009–2015, 2004.

List of Symbols

Roman symbols

<i>Symbol</i>	<i>Meaning</i>	<i>Units</i>
A	area	m^2
a	Tafel constant	V
b	Tafel slope	V dec^{-1}
C	capacitance	F
CE	current efficiency	—
COD	chemical oxygen demand	$\text{mol O}_2 \text{ m}^{-3}$
COD^0	initial chemical oxygen demand	$\text{mol O}_2 \text{ m}^{-3}$
c	concentration	mol m^{-3}
c^s	surface concentration	mol m^{-3}
D	diffusion coefficient	$\text{m}^2 \text{ s}^{-1}$
E	potential	V
E^o	standard thermodynamic potential	V
E_p	peak potential	V
$E_{p/2}$	half-peak potential	V
ΔE	difference in potential	V
ΔE^o	standard internal activation energy	kJ mol^{-1}
F	Faraday constant	C mol^{-1}
ΔG_r^o	standard Gibbs free energy change of reaction	kJ mol^{-1}
ΔH	apparent enthalpy of activation	kJ mol^{-1}
ΔH^o	standard enthalpy of activation	kJ mol^{-1}
I	current	A
I_f	faradaic current	A

<i>Symbol</i>	<i>Meaning</i>	<i>Units</i>
I_i	ionic current	A
I_{lim}	limiting current	A
I_p	current peak	A
ICE	instantaneous current efficiency	—
J	flux	mol s^{-1}
j	current density	A m^{-2}
j_{apply}	applied current density	A m^{-2}
j_{lim}	limiting current density	A m^{-2}
j_{lim}^0	initial limiting current density	A m^{-2}
K^o	calibration constant in Eq. 2.19	C mol^{-1}
K^*	calibration constant in Eq. 2.22	—
k	rate constant	$\text{m}^3 \text{mol}^{-1} \text{s}^{-1}$
k_m	mass transport coefficient	m s^{-1}
N	collection efficiency	—
n	number of microelectrodes	—
P	constant in Eq. 4.4	A m^{-2}
p	(a) reaction order	—
	(b) pressure	bar
Q	electric charge	C
Q_f	faradaic charge	C
Q_i	ionic charge	C
R	(a) gas constant	$\text{J mol}^{-1} \text{K}^{-1}$
	(b) resistance	Ωcm^2
	(c) equivalent dimension	m
r	(a) radius of a single electrode	μm
	(b) rate	mol s^{-1}
S	sensitivity factor	—
T	temperature	K
t	time	s
t_{cr}	critical time	s

<i>Symbol</i>	<i>Meaning</i>	<i>Units</i>
u	flow rate	$\mu\text{l s}^{-1}$
V	volume	m^3
x	distance	m
z	number of electrons	—

Greek symbols

<i>Symbol</i>	<i>Meaning</i>	<i>Units</i>
α	(a) dimensionless current density	—
	(b) anodic transfer coefficient	—
δ	thickness of diffusion layer	m
η	overpotential	V
ν	scan rate	V s^{-1}
Θ	relative surface coverage	—

Curriculum Vitae

Agnieszka Kapalka

Maiden name: Cięciwa
Nationality: Polish
Date of birth: 13.08.1979
E-mail: agnieszka@kapalka.eu

Education

2005–2008	PhD in Chemical Engineering, Swiss Federal Institute of Technology (EPFL) in Lausanne, Switzerland; Institute of Chemical Science and Engineering; major: Electrochemical Engineering
1998–2003	MSc and Eng. in Material Science, AGH University of Science and Technology in Krakow, Poland; Faculty of Materials Science and Ceramics; major: Advanced Ceramic Materials

Professional Experience

07.2004–10.2004	Trainee in the Environmental Technology Laboratory at EMPA in Dübendorf, Switzerland
10.2003–07.2004	Post-graduate student at the Department of Advanced Ceramic Materials at AGH, Poland
06.2003–07.2003	Trainee at the Department of Inorganic Chemistry of the Cantabria University, Spain
06.2002–09.2002	Trainee at the Physics Department of the Rostock University, Germany

Publications related to this work

A. Kapałka, B. Lanova, H. Baltruschat, G. Fóti and C. Comninellis. Electrochemically induced mineralization of organics by molecular oxygen on boron-doped diamond electrode. *Electrochem. Comm.*, in press.

A. Kapałka, G. Fóti and C. Comninellis. The importance of electrode material in environmental electrochemistry. Formation and reactivity of free hydroxyl radicals on boron-doped diamond electrodes. *Electrochim. Acta*, in press.

A. Kapałka, G. Fóti and C. Comninellis. Basic principles of the electrochemical mineralization of organic pollutants for wastewater treatment. In *Electrochemistry for the Environment*, Springer, in press.

A. Kapałka, B. Lanova, H. Baltruschat, G. Fóti and C. Comninellis. DEMS study of the acetic acid oxidation on boron-doped diamond electrode. *J. Electrochem. Soc.*, 155 (2008) E96.

C. Comninellis, A. Kapałka, S. Malto, S. A. Parsons, I. Poullos, D. Mantzavinos. Advanced oxidation processes for water treatment: advances and trends for R&D. *J. Chem. Tech. Biol.*, 83 (2008) 769.

A. Kapałka, G. Fóti and C. Comninellis. Investigations of the anodic oxidation of acetic acid on boron-doped diamond electrodes. *J. Electrochem. Soc.*, 155 (2008) E27.

A. Kapałka, G. Fóti and C. Comninellis. Determination of the Tafel slope for oxygen evolution on boron-doped diamond electrodes. *Electrochem. Comm.*, 10 (2008) 607.

M. Panizza, A. Kapałka and C. Comninellis. Oxidation of organic pollutants on BDD anodes using modulated current electrolysis. *Electrochim. Acta*, 53 (2008) 2289.

A. Kapałka, G. Fóti and C. Comninellis. Kinetic Modelling of the Electrochemical Mineralization of Organic Pollutants for Wastewater Treatment. *J. Appl. Electrochem.*, 38 (2008) 7.

A. Kapałka, G. Fóti and C. Comninellis. Investigations of electrochemical oxygen transfer reaction on boron-doped diamond electrodes. *Electrochim. Acta*, 53 (2007) 1954.

A. Cięciwa, R. Wuthrich and C. Comninellis. Electrochemical characterization of mechanically implanted boron-doped diamond electrodes. *Electrochem. Comm.*, 8 (2006) 375.

Oral Presentations

A. Cięciwa, Ch. Comninellis. Investigations of Electrochemical Oxygen Transfer Reaction on Boron-Doped Diamond Microelectrodes. 57th Annual Meeting of the International Society of Electrochemistry, Edinburgh, August 27th–September 1st, 2006.

A. Kapałka, C. Pulgarin, C. Comninellis, Degradation of organic pollutants for wastewater treatment, Water Workshop, EPFL, Lausanne, October 25th, 2007.

Poster Presentation

A. Kapałka, B. Lanova, H. Baltruschat, and C. Comninellis. Electrochemical oxidation of carboxylic acids on boron-doped diamond electrodes. 21st Century COE KEIO-LCC International Symposium Carbon Films: Applications for life and environment, March 9–10, 2007, Keio University, Yagami, Yokohama, Japan.